On the Design and Validation of a Variable Geometry Burner Concept

Thomas Leitgeb

Institute for Thermal Turbomachinery and Machine Dynamics

Dissertation

for the Degree of Doctor of Engineering Sciences

submitted to

the Faculty of Mechanical Engineering,
Graz University of Technology

Reviewer 1: Univ.-Prof. Dr.-Ing. Franz Heitmeir, Graz University of Technology
Reviewer 2: Prof. Dr. Tomas Grönstedt, Chalmers University of Technology

December 20, 2012

Funded by the European Commission within the 6th framework programme 'New Aero Engine Core Concepts' (NEWAC, AIP5-CT-2006-030876)

We humans are short-living creatures on a relatively small planet, which orbits around a remarkably ordinary star. Our central star turns around the center of an insignificant galaxy – one of many in a tremendously great universe of which we do not know if it is the only one. Should we particularly be something special in this corner of the cosmos, just because we happen to worry about these things?

- Jochen Stadler -

Audere est Facere

Statutory declaration

I declare that I have authored this thesis independently, that I have not used other than the declared sources / resources, and that I have explicitly marked all material which has been quoted either literally or by content from the used sources.

Place	Date	Signature

Acknowledgements

This thesis was written during my time as a research associate at the Institute for Thermal Turbomachinery and Machine Dynamics at Graz University of Technology. I would like to thank the head of the institute, Prof. Franz Heitmeir, for supporting and supervising this work and for the comfortable working atmosphere.

I also wish to thank Prof. Tomas Grönstedt for reviewing this thesis.

Special thanks go to Dr. Fabrice Giuliani for his support and his suggestions.

I would like to express my special gratitude to Prof. Jakob Woisetschläger, whose encouragement and support contributed to the success of this work. I will always keep our photo-trips and discussions in positive memory.

Also thanks to my former diploma students, Mr. Andreas Niederhammer and Mr. Roman Proebster, who supported me during the measurement campaigns.

Many thanks to my dear colleagues and staff at the institute for the comfortable working atmosphere, the discussions during the coffee breaks and the fun we had outside the world of work.

Last but not least, I would like to thank my family and friends, who supported me as best they could.

This work was funded by the European Commission within the 6^{th} framework programme 'New Aero Engine Core Concepts' (NEWAC, AIP5-CT-2006-030876).

Abstract

In order to reduce the impact of aviation on climate change and to reach the emission targets set by the governments, new innovative gas turbine core concepts are investigated. This work here focuses on the ability of a combustor to maintain stable combustion during a drastic reduction of main air through the core of the engine to improve off-design efficiency. A novel variable geometry burner was designed and validated, which was able to vary swirl strength and injector exit area continuously. These parameters were set independently depending on the operating point in order to maintain a certain flow field. As fuel a methane/air mixture was used and the burner was operated at atmospheric and unconfined conditions at a maximum thermal power of 5 kW. To show the effectiveness of the actuation, four special operating points were chosen which have been investigated more in detail. Beginning with a default operating point, swirl strength of the fluid and nozzle exit area have been varied independently. Mainly optical and laser-based measurement techniques have been applied during the experiments in order to gather information on flame shape and position, density and density fluctuations as well as temperature distributions. The extension of the operating range, the flame dynamics i.e. transition attached-detached and blow-off limits have been investigated. It was demonstrated that a stable lifted flame could be maintained by reducing the default air mass flow rate up to 50 %.

Contents

Nomenclature

	Latin symbols	
A	Cross section, area	m^2
$A_c(f)$	Effective measurement area (function of frequency f)	m^2
c	Speed of light	m/s
c	Speed of sound	m/s
c_p	Specific heat capacity at constant pressure	$J/(kg \cdot K)$
C_xH_y	Hydrocarbons	
CH^*	Chemical radical, necessary for prompt NO formation	
CO	Carbon monoxide	
CO_2	Carbon dioxide	
D	Depth	m
f	Frequency	Hz
G	Gladstone-Dale constant	m^3/kg
g_1	Grayscale intensity distribution of frame 1	
g_2	Grayscale intensity distribution of frame 2	
H	Height	m, mm
H_u	Lower heating value	MJ/kg
k	Constant	
k	Velocity-constant of a chemical reaction	$cm^3/(mol \cdot s)$
k	Vibrometer calibration factor	mm/s/V
L	Length, Distance	m, mm
L	Optical path	mm
$\dot{m}$	Mass flow rate	kg/s
n	Refractive index	
N_2O	Dinitrogen monoxide	
NNH^*	Chemical radical, result of the reaction of nitrogen and hydrogen	
NO	Nitrogen monoxide	
NO_2	Nitrogen dioxide	
NO_x	Nitric oxides	
O_2	Oxygen	
O_3	Ozone	
P	Thermal power	kW
p	Pressure	Pa
p_1	High pressure (massflow measurement)	Pa
p_2	Exit pressure	bar abs

p_2	Low pressure (massflow measurement)	Pa
R	Gas constant	$\mathrm{J/(kg \cdot K)}$
R_e	Reynolds number	
s	Entropy	J/K
SO_2	Sulfur dioxide	
T	Temperature	K
T_2	Exit temperature	°C
T_U	Turbulence level	
TiO_2	Titanium dioxide	
U	Vibrometer output signal	V
$V_{tot,RMS}$	Absolute RMS velocity	
V_{tot}	Absolute velocity	
W	Width	m, mm
w	Flow velocity	m/s
cd	Candela, SI base unit of luminous intensity	

Greek symbols

Δ	Difference	
ϵ	Deflection	rad
η	Efficiency	
γ	Specific heat ratio	
κ	Ratio of specific heat capacities	
λ	Wavelength	nm
ϕ	Equivalence ratio	
ϕ	Phase	rad
π	Pressure ratio	
ρ	Density	$\mathrm{kg/m^3}$
ζ	Length	m
ζ	Loss coefficient	

Subscripts

0	Initial condition
act	Actual
dyn	Dynamic
in	Inlet
max	Maximum
out	Outlet
red	Reduced
ref	Reference
sto	Stoichiometric
x	Coordinate
y	Coordinate

Abbreviations

3C	Three component
abs	Absolute
AFR	Air/fuel ratio (by mass)
approx	Approximately
AVBP	Explicit Euler-Euler solver (CERFACS)
CCD	Charged coupled device
CDP	Implicit Euler-Lagrange solver (Stanford)
deg	Degree (angle)
DEHS	Di-Ethyl-Hexyl-Sebacat
EU	European Union
exp	Experiment
FFT	Fast Fourier transform
FS	Full scale
GHG	Greenhouse gas
GUI	Graphical user interface
HCN	Hydrocyanic acid
HP	High pressure
HPT	High pressure turbine
IATA	International Air Transport Association
IIR	Infinite impulse response
IRZ	Inner recirculation zone
ITTM	Institute for Thermal Turbomachinery and Machine Dynamics
LabVIEW	Laboratory Virtual Instrumentation Engineering Workbench
LDI	Lean direct injection
LES	Large eddy simulation
LMS	Least Mean Squares
LP	Low pressure
LPP	Lean premixed prevaporized
max	Maximum
MEMS	Micro electro mechanical system
NGV	Nozzle guide vane
NI	National Instruments
OPR	Overall pressure ratio
OTDF	Overall temperature distribution factor
PAH	Polycyclic aromatic hydrocarbons
PC	Personal computer
PERM	Partial evaporation and rapid mixing
ppm	Parts per million
rel	Relative
RMS	Root mean square

RPK	Revenue Passenger Kilometers
RQL	Rich burn, quick quench, lean burn
RTD	Resistive thermal device
RTDF	Radial temperature distribution factor
SFC	Specific Fuel Consumption
sim	Simulation
SNR	Signal-to-noise ratio based on the average signal distance
stag	Stagnation
TAPS	Twin annular premixing swirler
TRL	Technology Readiness Level
UHC	Unburned hydrocarbons
UV	Ultraviolet light
VDC	Volts (direct current)

Chapter 1

Introduction

1.1 Motivation

Over the past four decades air travel has encountered strong growth despite periods of drawbacks caused by geopolitical and economic issues and wars (*Fig. 1.1*) [1]. In total a mean annual growth of 5 % over the last 20 years was achieved doubling the air traffic every 15 years. The forecast of the air traffic development for the year 2030 is around 12 trillion revenue passenger kilometers (RPK).

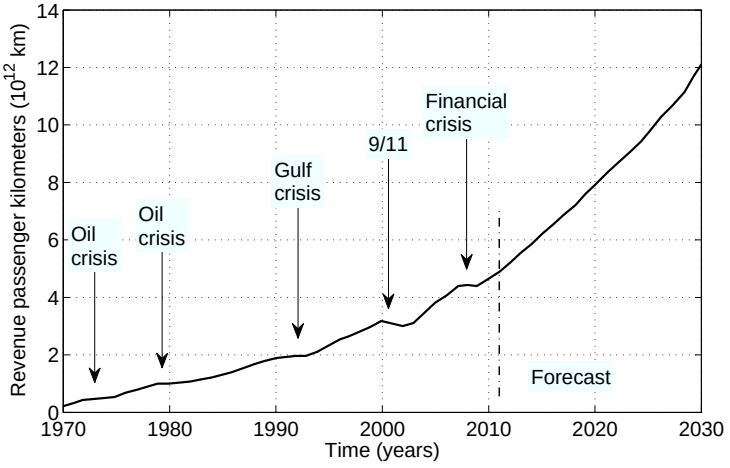

Fig. 1.1: Air traffic development [1]

The impact of aviation to climate change seems to be rather small as it produces 2 % of the global carbon dioxide (CO_2) emissions (12 % of CO_2 from all transport sources, compared to 74 % from road transport) and 3 % of the total manmade contribution to climate change [2]. However, as the emission takes place approximately 10 km above sealevel, the pollutants are considered to be disproportionately relevant [3]. Therefore, airline industry has established a comprehensive framework to lower the levels of greenhouse gas (GHG) emissions. For that four key areas were identified, namely, improved technology, effective operations, efficient infrastructure, and positive economic measures [4]. The impact of these is depicted in *Fig. 1.2*. If business-as-usual will take place fuel consumption and hence CO_2 emissions will increase most likely according to the solid line. By applying effective operations and infrastructure the emissions may be reduced to levels according to the dashed line. Carbon-neutral growth starting from 2020 and even a 50 % reduction of emissions at 2050 shall be reached by using new technology, i.e. biofuels or innovative

core concepts [5]. The deviation of the gross emission curve between the years 2020 and 2037 from the neutral growth curve shall be compensated by financial measures.

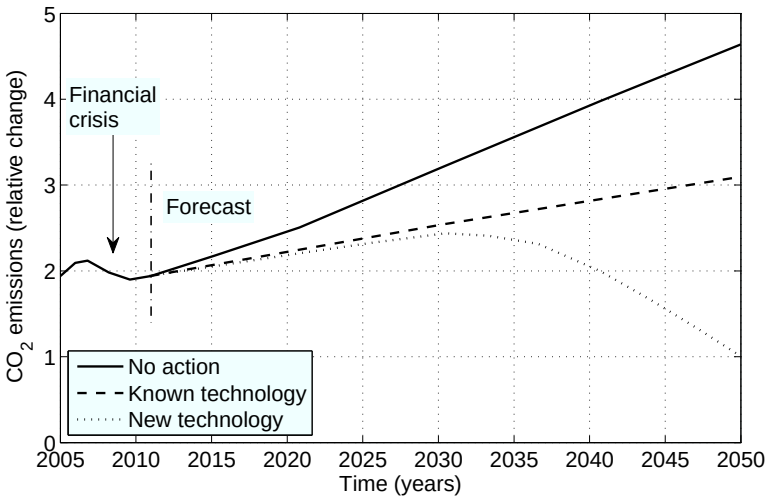

Fig. 1.2: Emissions reduction roadmap [4]

As mentioned before, novel engine concepts are necessary to reach the emission targets. Furthermore, fossil fuel is a limited quantity and costs may drastically increase in future. Therefore, technologies are already under investigation and potentials in terms of fuel savings are estimated [6, 7]. The technical challenges of these concepts are the increased pressure ratios, the higher turbine inlet temperatures, and the drastic variations of core air mass flows due to optimized control schedules. These variations of mass flow during flight may lie between 6 to 50 %. This has strong effects on the combustion stability as flame blow-off and flashback can occur or the flame may undergo a transition from a lifted to an attached state. New combustor technologies and designs might therefore be necessary which help to enlarge the operating range.

1.2 Objectives

The aim of this work was to enlarge the operating range of a burner in case of a drastic main air feed reduction with the help of novel variable geometry concept at the injection, where a conventional geometry would lead to flame blow-off, flash back or flame shape transition.

The parameters which were altered were the swirl strength and the exit velocity of the fluid of the injector. Both parameters have a strong influence on the flow field in the primary combustion zone and hence on the combustion process itself. The idea was to design and analyze a burner which is able to adjust the injector exit area and the swirl angle as a function of the operating point. At the default operating point of the burner a swirl-stabilized lifted flame is produced and the actuation system is in its default position. To maintain stable combustion in the case of drastically decreased main air, the inlet area is reduced and the swirl component is adjusted in similar proportion so that an appropriate flow field is achieved again.

1.3 Methodology

To prepare for the design of the actual variable geometry burner, a literature survey was performed to agree on the geometric parameters and on their implementation. In order to determine the shape of the burner exit nozzle, a number of numerical simulations have been performed. Afterwards, the burner and a versatile test rig have been built and experiments have been carried out where the fixed geometry setup was tested against the variable geometry setup. Based on these investigations a stability chart has been created. During this task four specific operating points have been selected which have been analyzed more in detail by optical and laser-based measurement techniques.

Chapter 2

Gas turbine combustion technology

To begin with, a gas turbine is a heat engine which basically consists of a compressor, a combustion chamber, and a turbine. The gas turbine uses air as working fluid to produce thrust. For that, the working medium flowing through the gas turbine has to be accelerated. The engine is illustrated in *Fig. 2.1* in which (0) to (8) represent specific points of the cycle. From (0) to (3) air is compressed to increase the pressure energy. This is achieved by the retention at the engine intake and by the compressor. Heat energy addition is done in the combustion chamber from (3) to (4) at nearly constant pressure. To drive the compressor some of the energy is turned into mechanical energy by the turbine from (4) to (5). The remaining kinetic energy is used to produce a propulsive jet.

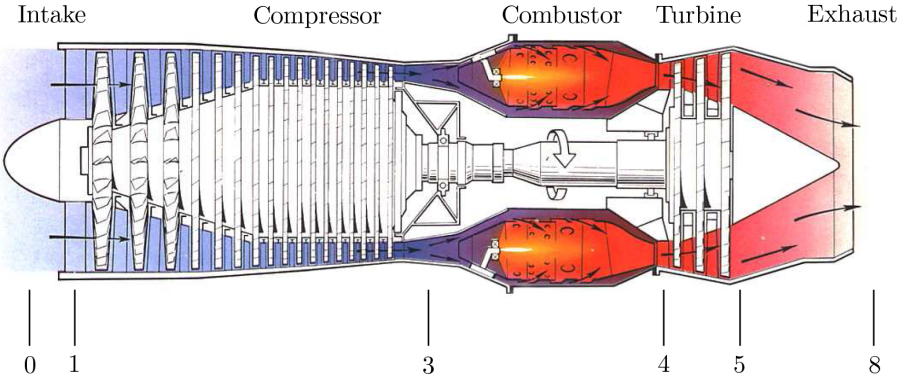

Fig. 2.1: Conventional gas turbine engine [8]. In the single-shaft application the thrust is produced by the kinetic energy of the exhaust jet.

Figure 2.2 illustrates the working cycle of a gas turbine, also known as Joule or Brayton cycle, on a temperature-entropy diagram.

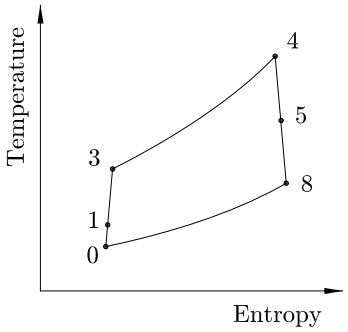

Fig. 2.2: Gas turbine working cycle on a temperature-entropy diagram

Depending on the application, the turbine is either used to drive the compressor (*Fig. 2.1*) or to drive the compressor and a so-called fan (*Fig. 2.3*). At the first application (conventional), the thrust is produced by a propulsive jet (*Fig. 2.1*), at the latter (modern), most of the thrust (approximately 70 %) is produced by the fan (*Fig. 2.3*). The most recent design, as illustrated in *Fig. 2.3*, has a lower fuel consumption and produces less emissions and noise compared to the state-of-the-art design. The gas turbine shown, a Rolls-Royce Trent 900, has a three-shaft architecture and is used to drive the Airbus A380 family.

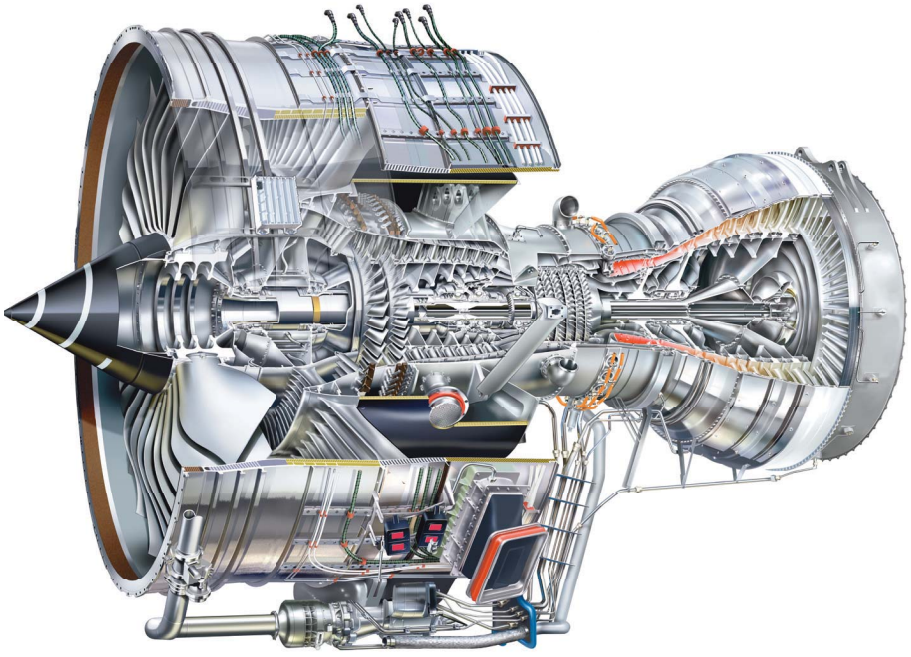

Fig. 2.3: Modern gas turbine engine [9]. The Rolls-Royce Trent 900, which is used to drive the Airbus A380 family, has a three-shaft architecture. Most of the thrust is produced by the fan at the front of the engine.

2.1 The combustion chamber

As mentioned above, the combustion chamber or combustor is one of the main parts of a gas turbine (*Fig. 2.1*). In the following, requirements, principles, designs, and types of combustion chambers will be discussed.

2.2 Requirements

Due to the key role of the combustor, it must satisfy a wide range of requirements. Their relative importance depends on the application and on the engine type and can be listed as follows [10, 11]:

1. High combustion efficiency (conversion of chemical energy into heat)
2. Reliable and smooth ignition on the ground and at high altitude
3. Wide operation range and stability limits

4. Low pressure loss
5. Outlet temperature distribution for maximum live of turbine blades and nozzle guide vanes (NGV)
6. Low emission production
7. Maintainability and durability
8. Multifuel capability

2.3 Fundamental principles of combustion chambers

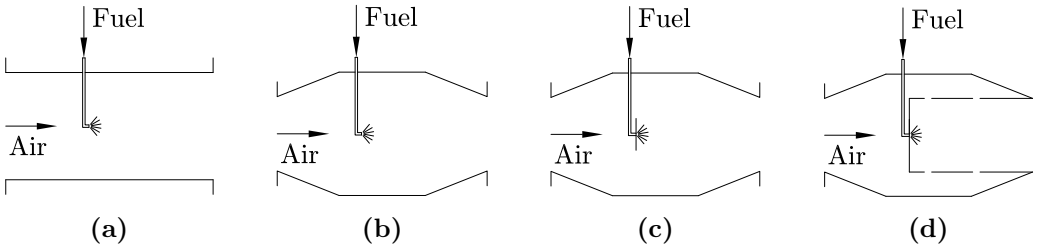

Fig. 2.4: Principles of combustion chambers [11]

The simplest form of a combustion chamber is a straight tube connecting the compressor and the turbine, as shown in *Fig. 2.4a*. However, this design produces an excessive pressure loss as the compressed air exits the high pressure compressor at around Mach 0.3. To reduce the velocity, a diffuser is applied (*Fig. 2.4b*) and velocities of the order of 30 m/s are achieved. In order to anchor the flame, a bluff body or a swirling device can be used to establish a recirculation zone, shown in *Fig. 2.4c*. As combustion is sustained only in regions with an appropriate air/fuel ratio, a liner or flame-tube is employed to distribute the air needed for the combustion process (*Fig. 2.4d*) and to protect the pressure vessel from excessive heat.

2.4 Combustion zones

The section of the combustion chamber in which the flame stabilizes is called the primary zone, as illustrated in *Fig. 2.5*. As mentioned above, the flame settles itself in the recirculation of a bluff body or a swirling device. The main function of the primary zone is to provide enough time and turbulence to achieve a reasonable atomization and evaporation and eventually complete combustion. As temperatures as high as 2000 °C can occur, the hot gases have to be cooled down before entering the NGVs and the first rotor stage of the high pressure turbine (HPT). This is done in the secondary or intermediate zone. In the dilution zone, more air is introduced in order to set the temperature profiles before the hot gases are entering the turbine stage. For quantification, the overall temperature distribution factor (OTDF) and the radial temperature distribution factor (RTDF) are used, which describe the temperature distribution in circumferential and radial direction, respectively. The position, size and number of orifices for introducing the cooling and dilution air has a major influence on the stability and on the emission production during the combustion process. *Figure 2.5* also illustrates the distribution of the airflow within a

conventional combustor. Around 40 % of the total air mass flow is directed to the primary zone, the rest is used for cooling of the combustion chamber (2/3) and dilution (1/3). More information on emission production and formation is given in *App. E*.

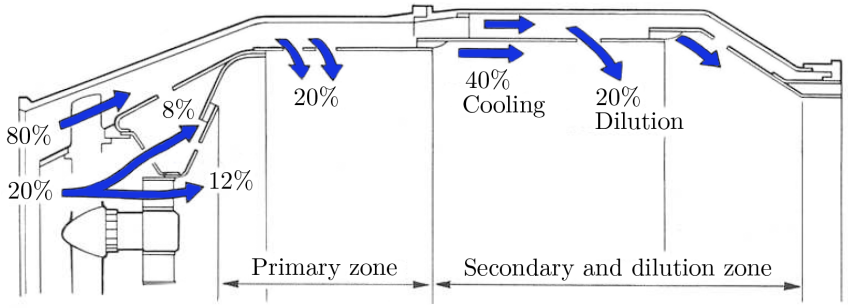

Fig. 2.5: Airflow distribution within the combustion chamber [8]

2.5 Types of combustion chambers

In general three types of combustion chambers exist – can or tubular, can-annular or tubo-annular, and annular. The main difference between the types is the placement and number of liners used. The combustor types are illustrated in *Fig. 2.6*. The choice of a specific type is determined mainly by the engine design, however, in modern engines usually annular combustors are used.

(a) **(b)** **(c)**

Fig. 2.6: Combustor types [12]. Can combustor (a), can-annular combustor (b), annular combustor (c). Flow direction is from left to right.

2.5.1 Can combustor

As can be seen in *Fig. 2.7a*, a cylindrical liner is mounted concentrically inside a pressure casing. The liners are connected via cross-fire tubes due to ignition. Depending on the engine size, 6 to 16 combustors are normally employed. The development and maintenance effort is rather low, however, due to their excessive length and weight, their main field of application are industrial units. This type was used by the early jet engines Whittle W2B, Jumo 004, and Rolls-Royce Nene [11].

2.5.2 Can-annular combustor

The can-annular combustor employs a group of flame-tubes, from 6 to 10, arranged inside a single annular pressure casing (*Fig. 2.7b*). Again, the liners are connected via cross-fire tubes. Compared to the can combustor, the can-annular type is more compact. The GE J73, the P&W J57 as well as the Rolls-Royce Avon are fitted with this combustor type.

2.5.3 Annular combustor

As illustrated in *Fig. 2.7c*, a single annular flame-tube is mounted concentrically inside an annular pressure casing. Aerodynamically, this design results in a lower pressure loss than the other combustor types but it can be sensitive to combustion oscillations as the single burner modules may interact at certain operating points. However, since the 1960s this type of combustor is the choice for all new aircraft jet engines.

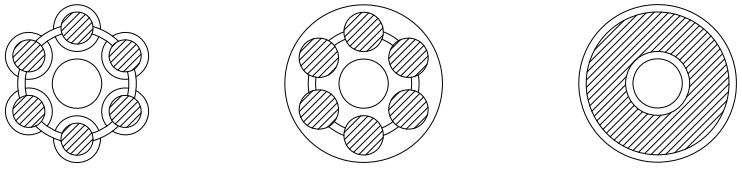

Fig. 2.7: Cross-sections of combustor types [11]. Can combustor (a), can-annular combustor (b), annular combustor (c). The hatched areas illustrate the reaction zones.

2.6 Key components of the combustion chamber

Although many variations of the basic design (*Fig. 2.4d*) exist, some key components of a combustion chamber can be identified, namely diffuser (1), combustion chamber casing (2), liner (3), fuel injector (4), and igniter (5), as shown in *Fig. 2.8*. Additionally illustrated are the primary zone (6) and intermediate (7) and dilution zone (8).

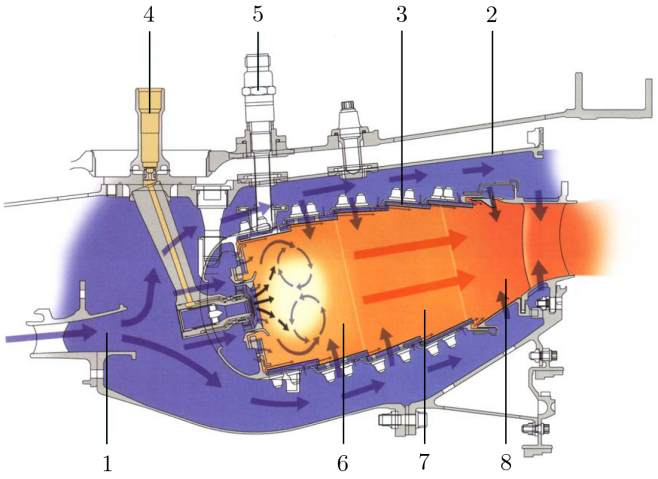

Fig. 2.8: Key components of a combustor [12]. Arrows are indicating flow paths.

2.7 Fuel injectors

Fuel preparation and hence the processes of atomization and evaporation of liquid fuels are essential to the performance of a combustor. In general, the better the spray quality, the better the evaporation, which also affects combustion stability and efficiency as well as emission production. There are three types of fuel injectors, namely pressure atomizers, airblast atomizers, and premix-prevaporize modules, as shown in *Fig. 2.9*.

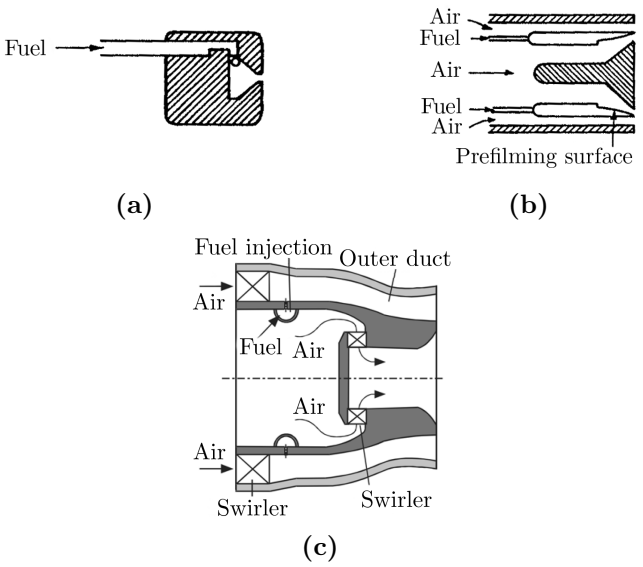

Fig. 2.9: Injector types. Pressure atomizer (a) [11], airblast atomizer (b) [11], premix-prevaporize module (c) [10]

Pressure atomizers achieve atomization by forcing fuel under pressure through an orifice (*Fig. 2.9a*). A major drawback of this design is to achieve good atomization over the fuel flow range, as doubling the fuel mass flow rate requires quadruplication of the pressure. Depending on the size of the orifice – the smaller, the better the atomization – high pressures might be necessary.

The airblast atomizer can be operated at low pressure levels. Fuel is forced to flow over a lip which is positioned in an airstream (*Fig. 2.9b*). The high kinetic energy (high velocity) of the airstream atomizes the fuel and the droplets are carried into the combustion zone. Problems with this type arise if the velocity of the airstream is not high enough, for instance at start-up, which results in poor atomization quality and narrow stability limits.

By injecting the fuel into the swirled airstream within the module, a certain degree of evaporation and premixing is achieved, as illustrated in *Fig. 2.9c*. This reduces the emission production compared to the other designs. However, disadvantageous is the sensitivity to flashbacks due to the combustible fuel/air mixture within the duct of the module. The residence time of the mixture within the module is an important factor at the design phase.

The injection of gaseous fuels is less critical than that of liquid fuels, as the residence time of gaseous fuels can be longer and no evaporation has to be performed. Gaseous fuels can be injected by orifices, swirlers, and venturi nozzles.

Chapter 3

Variable geometry parameters

In general, when talking about variable geometry an actuator is altering a geometric parameter. In a combustion system this can be the position of a valve or a splitter controlling the air mass flow [13–15] or moving the flametube walls for changing the combustion chamber volume [16].

This work here focused on altering the geometric parameters of the injector in terms of rotation or swirl of the fluid and the exit area ratio of the burner exit nozzle. As will be seen in *Sec. 8*, both parameters can be set continuously and independently during operation. Compared to variable chamber geometry, acting on the injector is advantageous, as the first needs high expenditures in design and is technically complex [17].

3.1 Swirl

The swirl of the fluid is an important parameter, as it is used to stabilize the flame. When swirl is introduced to a jet flow, axial and radial pressure gradients are formed which grow with the strength of the swirl. Moderate gradients widen the jet without establishing a back flow (*Fig. 3.1a*). Due to high gradients at higher degrees of swirl back flow occurs and a recirculation zone can be formed (*Fig. 3.1b*). As mentioned above, the flame stabilizes itself in this zone due to the velocity profile. Hence, flames are strongly affected by the degree of swirl as it influences its size, shape, stability, and intensity [18]. If liquid or solid fuels are used, the hot recirculated gases are essential for the evaporation of the oil drops and the devolatilization of the solid particles [19].

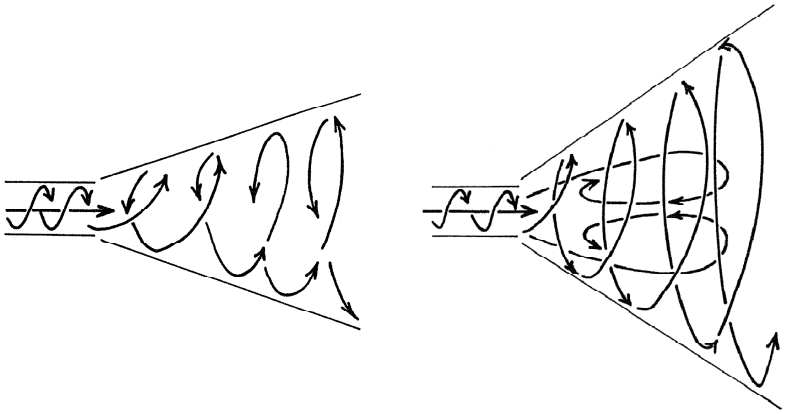

(a) **(b)**

Fig. 3.1: Flow fields of swirling jets [20]. Low swirl (a), high swirl (b)

3.1.1 Swirl number

The degree of swirl is usually characterized by the swirl number S, as suggested by [21]. It is a non-dimensional criterion based on the axial flux of the angular momentum G_φ and the axial flux of the axial momentum G_x as both G_φ and G_x are conserved in swirling free jets and flames [21]. Thus, the swirl number calculates as:

$$S = \frac{2}{D}\frac{G_\varphi}{G_x} \tag{3.1}$$

where D denotes as the exit nozzle diameter. The fluxes can be written as follows:

$$G_\varphi = \int_{\varphi=0}^{2\pi}\int_{r=0}^{\infty} (\rho\, v)\, u\, r^2\, dr\, d\varphi = \text{const} \tag{3.2}$$

$$G_x = \int_{\varphi=0}^{2\pi}\int_{r=0}^{\infty} (\rho\, u)\, u\, r\, dr\, d\varphi = \text{const} \tag{3.3}$$

The axial and tangential components of the velocity denote as u and v, respectively. Turbulent normal and shear stress terms as well as the pressure term have been neglected, which makes S the local swirl number. *Figure 3.2* illustrates the notation at an infinitesimal cross-section dA for calculating G_φ and G_x.

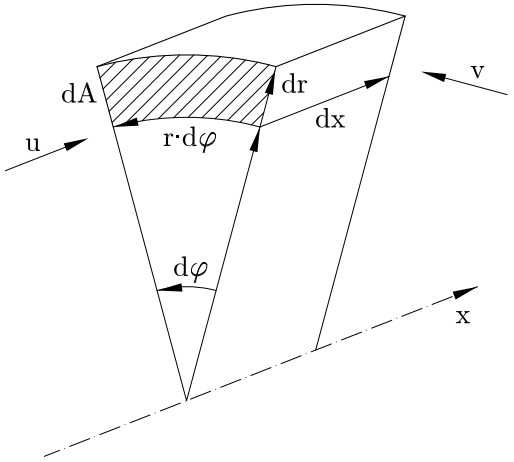

Fig. 3.2: Infinitesimal cross-section of a swirling jet

If the axial flux of the angular momentum is calculated directly at the swirl generator employing its geometrical data, a theoretical swirl number is obtained. A good summary about different definitions of swirl numbers is given in [22].

3.1.2 Generation of swirl

Several methods of inducing swirl exist which may be divided into three main categories according to [20, 21]. Tangential entry of the fluid into a cylindrical duct (I), guided vanes (II), and direct rotation i.e. rotating vanes, tubes or grids (III). Of practical use are methods (I) and (II), method (III) is sometimes used in experiments [23], but needs high rotational speed when the swirl is solely imparted through viscous forces [24]. The strength

of swirl is controlled by the revolutions of the rotating device. When using tangential inlet slots for swirl generation, the strength can be adjusted through different inserts [25] or by blocking the area of the slots [26]. Another way to adjust the swirl strength applying method (I) is to control the ratio of the tangential and axial air mass flow while keeping the overall mass flow rate constant [27, 28]. This type of swirl generator is simple to produce [21] and is mainly used for slow to medium swirl strength (*Fig. 3.3*). At high degrees of swirl this method produces distinct pressure drops. In general applying method (II) results in higher degrees of swirl producing pressure drops at an acceptable level [20]. *Figure 3.4* shows a generic axial swirl generator [21]. The swirl strength can be adjusted seamlessly when using a movable block swirl generator (*Fig. 3.5*). Two adjacent parts are moved such that a flow with zero swirl to a certain swirl strength can be produced [21, 29–31]. By applying guide vanes variable swirl can be reached by adjusting the vane angle [32, 33] or by moving the swirl generator in axial direction [34]. Most of the variable swirl generators have been tested on laboratory burners; a list of selected papers is given in *App. A*.

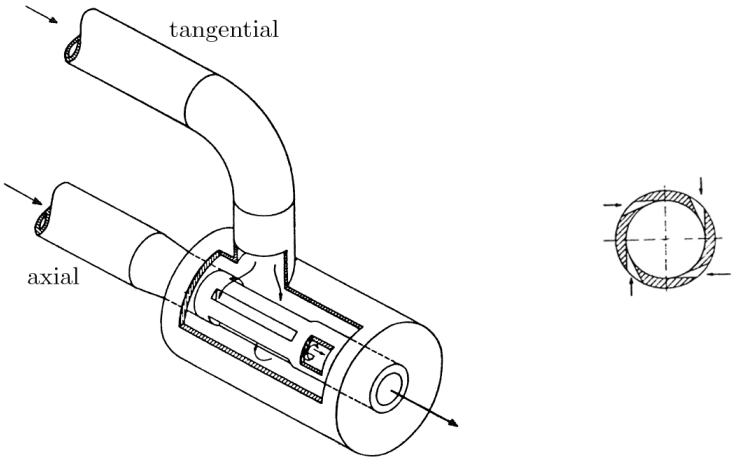

Fig. 3.3: Tangential swirl generator [27]. The swirl generator has separate feed lines for axial and tangential air (a), cross-sectional view illustrating the tangential inlet slots (b). Arrows are indicating flow paths.

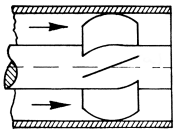

Fig. 3.4: Axial swirl generator. Arrows are indicating flow paths.

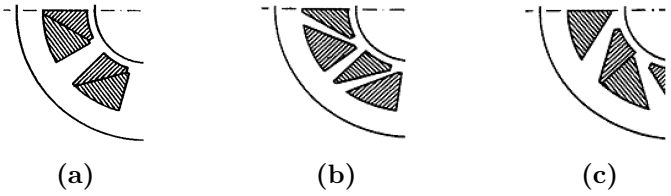

Fig. 3.5: Movable block swirl generator [35]. No swirl (a), medium swirl strength (b), maximum swirl strength (c)

3.1.3 Flame stabilization

The compressed air for the combustion process exits the high pressure compressor at around Mach 0.3. A diffuser thus is used to slow down the fluid while a so-called liner or flame tube is employed to distribute the air needed for the combustion process. Unfortunately, this is not sufficient for stabilizing the flame. Methods generating local recirculations (*Fig. 3.6*) have to be applied. This can be done either by a bluff body like an orifice plate or a V-shaped flame holder, or by a swirl generator stabilizing the flame aerodynamically.

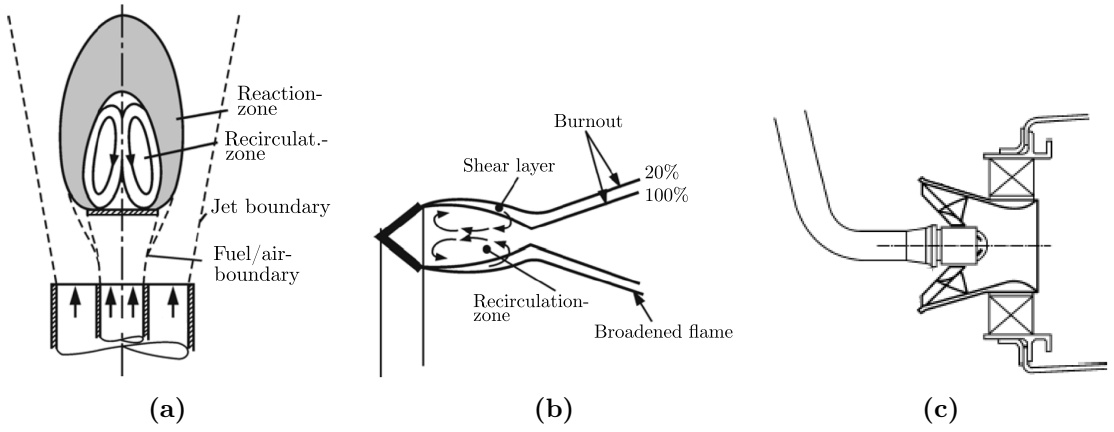

Fig. 3.6: Types of flame stabilization [10]. Bluff body (a) and (b), swirl-stabilized (c)

As the orifice plate and the v-shaped flame holder, as used by after-burners, intrude the flow they are subject to strong wear out and damage, even more in case of a flash back. In a swirl-stabilized flow the flame is stabilized aerodynamically. No mechanical parts are directly involved. Furthermore, the pressure drop generated and the number of maintenance intervals are lower.

Flame stabilization is even more important in lean premixed combustion, as it is applied in modern gas turbines to reduce the emissions. Fuel and air are mixed in the mixing tube shortly before the swirl generator. Due to a flashback the flame may stabilize within the mixing tube and can lead to damage of mechanical parts through thermal loading. In swirl-stabilized burners four mechanisms can be identified initiating flashback, namely flame propagation in the boundary layer, turbulent flame propagation in the core flow, combustion instabilities, and combustion induced vortex breakdown [36, 37]. When designing a burner, these mechanisms have to be taken into account as they depend on the geometry and the velocity distribution in axial and tangential direction.

3.1.4 Vortex breakdown

Vortex breakdown is a process that involves the rapid transformation of the swirling flow from a highly organized, undisturbed state to a large-scale, highly turbulent flow region [38]. The breakdown can lead to strong fluctuations further downstream and may be irrespective of the type of in- and outflow conditions, which makes it an important fact to consider when dealing with swirling flows. It has been found that the predominant parameter for determining the onset of vortex breakdown is the ratio of the circumferential to the axial velocity v/u [39], i.e. when the value of the characteristic circumferential velocity becomes sufficiently large relative to the characteristic axial velocity, the flow

undergoes vortex breakdown. It has to be noted, that through vortex breakdown the resonant acoustic modes of a flow system may be excited which can produce vibrations of the mechanical structure. This is due to the fact, that the downstream fluctuations are in the form of a helical instability similar to that observed for higher-order modes of a jet. Up to now, the mechanism responsible for producing the onset of the vortex breakdown is an active field of investigation and not fully understood. Overviews and assessments can be found in [39–41].

3.1.5 Combustion instabilities

As mentioned above, flame stabilizing is done aerodynamically by using swirlers which produce flow fields with back flows which allow the flame to settle. The inevitable shear layers due to the flow, on the other hand, induce vortices and flow instabilities which cause an alternating heat release rate and thus pressure waves. These are being reflected on the boundaries and can interfere with the flame to cause even more unsteady heat release [42]. Due to this coupling combustion oscillations may arise. Combustion oscillations may also occur during lean combustion of hydrocarbons, a technology to reduce nitric oxides by combustion at lower temperatures. These instabilities can be reduced by means of active control; a good overview of control strategies which mainly focus on fuel modulation is given in [43]. Enhanced sensors for improved combustion control can be seen in [44]. However, combustion instabilities will not be covered by this work here.

3.2 Injector exit area

By altering the injector exit area, the exit velocities can be adjusted according to the operating conditions in order to maintain stable combustion. The area of the exit nozzle can be adjusted either by orifices and diaphragms [45, 46] or by axially moving of bluff bodies [47], as will be shown in *Chap. 4*. An advantage of applying a bluff body is the formation of a recirculation zone downstream of the exit nozzle (*Fig. 3.7*) allowing a broader swirl strength range and mitigating the risk of flashback [36, 37].

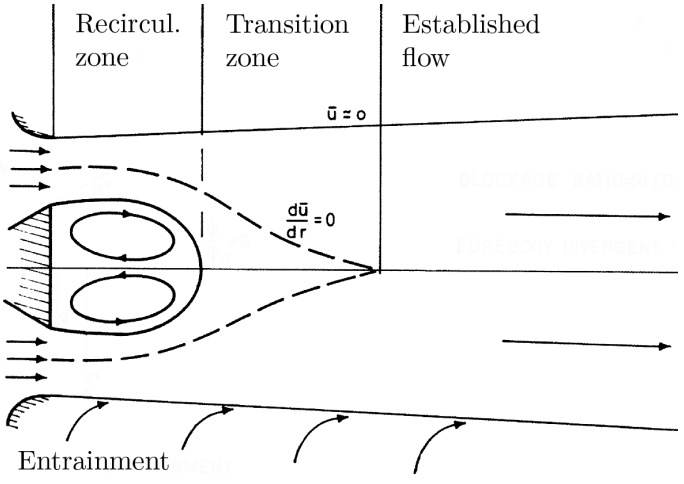

Fig. 3.7: Flow field in the wake of a bluff body [21]. Arrows are indicating flow paths.

Chapter 4

Literature review

This chapter is intended to give a concise overview of various types of variable geometry applications in combustion chambers of gas turbines. Information is gathered not only from technical papers and reports but also from patents. A lot of work concerning variable geometry in combustion technology has been done in the 1950s and 1960s. It may be due to problems for industrial implementation, i.e. complex control, added weight, cost, reliability, that the topic variable geometry faded away in the early 70s. Especially in aviation, where security measures are very tight and therefore technology is considered to be conservative and resistant against new applications. Due to more stringent emission regulations and improved materials and control strategies variable geometry became interesting again in the 1980s as through fuel control the ambitious targets in terms of emissions might not be reached. Combustion instabilities might be mitigated or even prevented by variable geometry combustion. It could keep temperatures around 1670 K, which means reaction rates are high and combustion zones can be made smaller, which in turn decreases combustor size and weight [11]. Additionally, temperature distribution within the combustor may be controlled in order to prevent hot-spots. Variable geometry can also be used to ameliorate efficiency at off-design operation points such as idle and taxiing as newly proposed core concepts entail drastic changes of mass flow through the combustor or to provide better stability at lean part load modes which makes it an alternative to staged combustion (complex liner) using a classical annular combustor. Another advantage compared to staged combustion is the ability of variable geometry technology to change the operating point without power jumps as would be observed if stages are turned on or off. Variable geometry may also enable different power loads per burner module for specific part load or transient operation. An increased activity concerning variable geometry is thus observed up to now. Advantages and disadvantages concerning variable geometry combustion are summarized in *Tab. 4.1*.

Tab. 4.1: Advantages and disadvantages of variable geometry

Advantages	Disadvantages
Extended combustion range	Added weight and cost
Adapts flame to operation	Complex control
Flame stability	Need for robust/effective actuation
Emission reduction	Need for fail-safe strategy
	Low technology readiness level (TRL)

Anyway, it is not uncommon that elder technology concepts experience a revival. In general, two reasons might be responsible for this. Firstly, the performance requirements and secondly, the technology readiness level of supporting technologies. For instance, in former

times, the requirement on the combustion chamber was just to maintain a stable flame. This was achieved by using a conventional chamber design with rigid geometry. A variable geometry design could have done the same but was to complex and would have created problems at the certification authority. Today, efficiencies at off-design points have to be increased and emissions throughout the flight envelope should be at a minimum. It is thought, that by means of variable geometry combustion these targets can be achieved. When using variable geometry, a certain amount of moving parts is necessary which are exposed to pressure, heat, and vibrations. The lack of eligible materials and/or control technologies might be responsible for refusing this technology in combustion chamber design in the past decades.

4.1 Air flow splitters

Aoyama and Mandai [13] used a butterfly valve to maintain constant fuel/air ratio over the whole operating range of a 120 MW gas turbine in order to reduce NO_x emission levels. At low-power requirements and starting when fuel flow rates are low, the butterfly valve (1) is opened (*Fig. 4.1*). Combustion air is then injected into the transition duct (2) before the turbine (3) bypassing the pilot (4) and main (5) stage of the combustion chamber. At base load and high power operating points the butterfly valve is gradually closed.

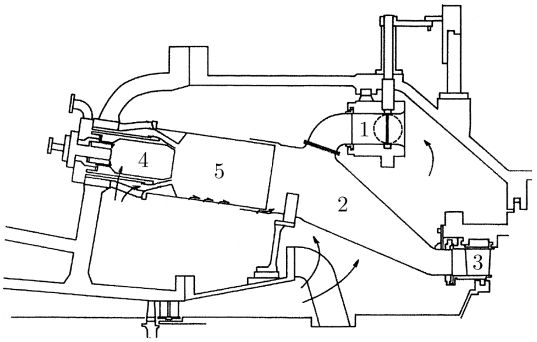

Fig. 4.1: A butterfly valve is used to control air mass flow of pilot and main stage of the combustion chamber. Arrows are indicating flow paths.

Hayashi et al. [48] employed butterfly valves (1) placed in air-flow ducts in order to control the distribution of main (2) and dilution (3) air of the combustor (*Fig. 4.2*). The system was tested on a natural gas-fired 210 kW gas turbine. NO_x emission levels of 10 ppm at 90 % full power have been achieved.

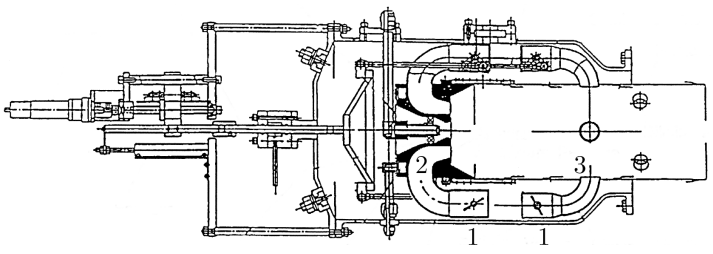

Fig. 4.2: Butterfly valves are used to control the distribution of main and dilution air.

Johnson and Wilkes [49] used an external valve mechanism (1) in order to control the distribution of air for the reaction (2) and dilution (3) zones (*Fig. 4.3*).

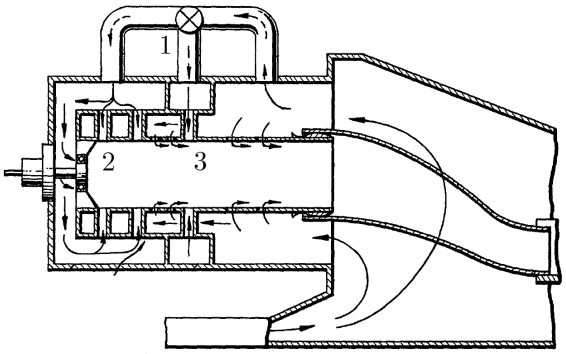

Fig. 4.3: Combustion air control system using an external valve mechanism. Arrows are indicating flow paths.

Corr [50] used a plurality of poppet valves (1) to direct air to the mixing or dilution zone (*Fig. 4.4*). By actuating the valves the total open area of the combustor was not changed and, hence, the total pressure loss was not affected. The valves had only two operating positions which resulted in a mechanically straightforward design.

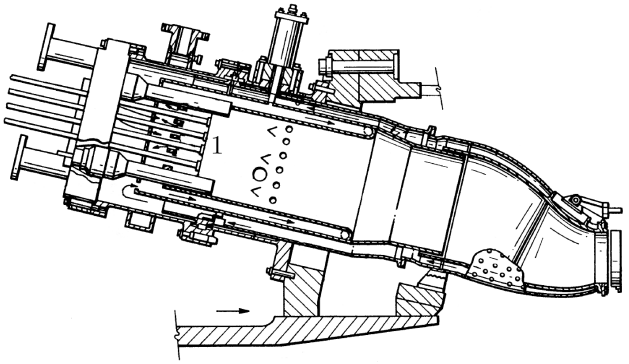

Fig. 4.4: Poppet valves for air distribution control. Arrows are indicating flow paths.

Li and Hales [14] installed a hydraulically driven (1) air flow splitter (2) upstream of the combustion chamber (*Fig. 4.5*). Axially moving the splitter altered the cross-sectional area ratio and hence the air flow to the primary zone. It was found that in combination with fuel staging the movement of the splitter can be reduced which is beneficial to the air flow field at the combustor inlet.

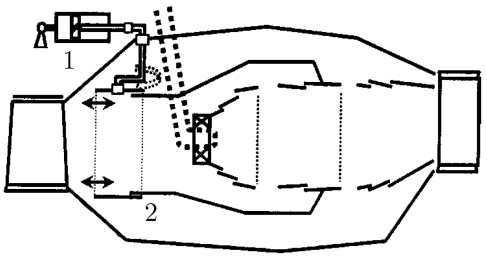

Fig. 4.5: The axially moved splitter controls the air flow ratio to the primary zone.

Egan et al. [51] used a conical splitter (1) which was moved back and forth to control the air mass flow of a staged swirler (2) depending on the operating point (*Fig. 4.6*). At low power operation the splitter was moved forward guiding all air flow through the inner swirler vanes and blocking the outer ones.

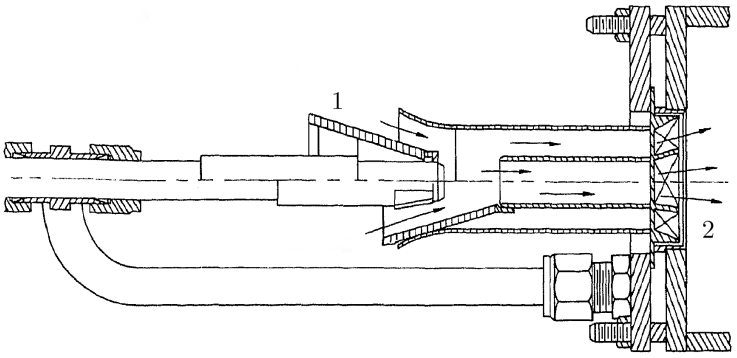

Fig. 4.6: Conical splitter. The position of the splitter for maximum power is drawn above the centerline, for low power requirements below. Arrows are indicating flow paths.

Sampath and Davenport [52] used an annular baffle (1) to regulate the air flow according to power levels (*Fig. 4.7a*). For default operation the baffle is in the rightmost position (dashed lines, *Fig. 4.7b*) allowing air entering the primary and secondary zone as well as the premixing zone providing lean combustion. For idle and standby power needs the baffle is in the leftmost position (full lines, *Fig. 4.7b*) forcing more air through the secondary dilution holes producing a rich primary zone. The enhanced dilution more efficiently cooled the hot gases keeping the emission production low.

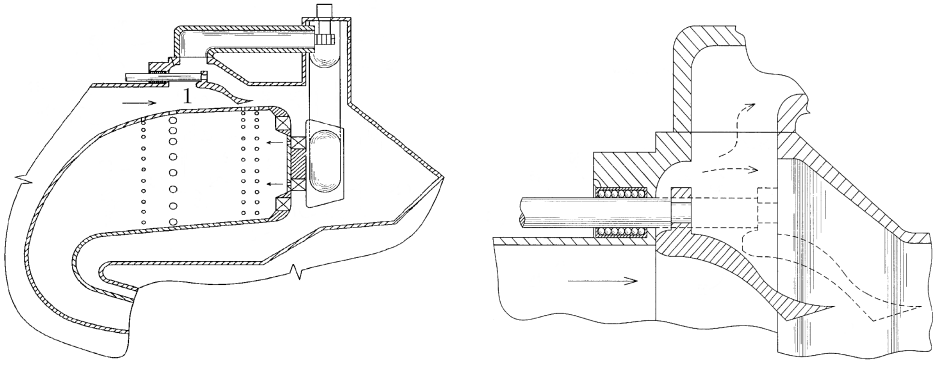

(a) **(b)**

Fig. 4.7: Sliding baffle. An annular baffle is used to divert the air mass flow (a). Positions of the baffle according to the power needs (b). Full lines: idle, dashed lines: default operation. Arrows are indicating flow paths.

Arvin et al. [53] employed sleeves for adjusting the inlet areas of mixing (1) and dilution (2) air in order to control the distribution of the oxidizer (*Fig. 4.8*). By moving the sleeves, which were rigidly coupled by a plurality of rods (3), the total inlet area of the combustor was kept constant.

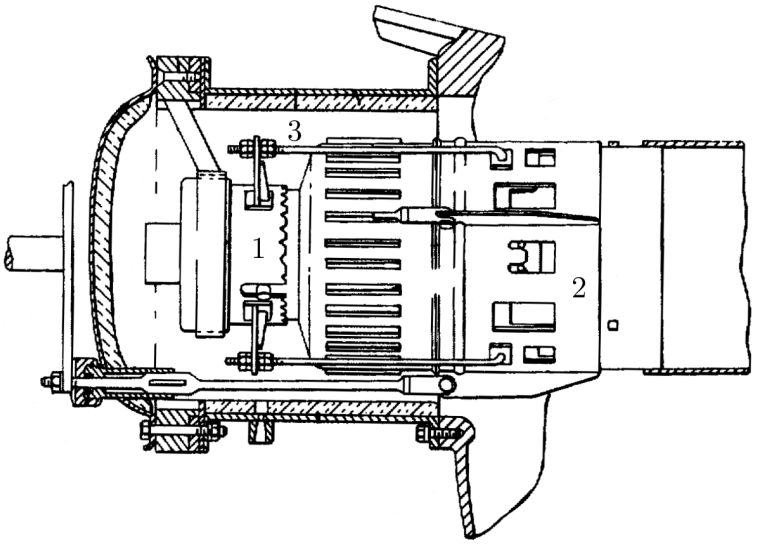

Fig. 4.8: Rigidly coupled annular sleeves

4.2 Moving liner wall segments

Bardey et al. [16] invented a combustion chamber with moving liner wall segments (*Fig. 4.9*). Depending on the operating point the combustor volume is varied in order to optimize the fuel/air ratio and the residence time. By doing so combustor efficiency is increased and emission levels are reduced.

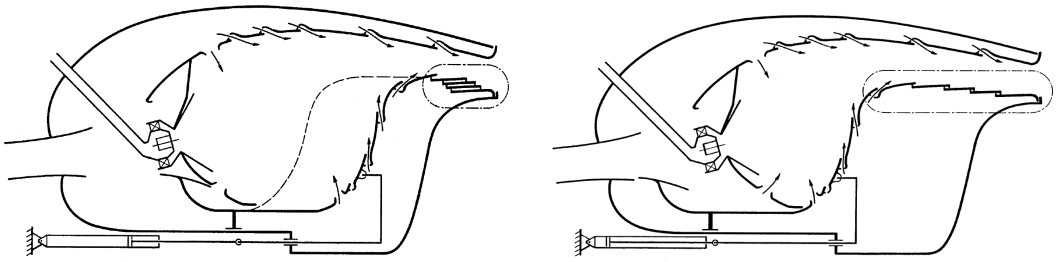

(a) (b)

Fig. 4.9: Moving liner wall segments. Maximum volume at full power (a), minimum volume at idle (b). Arrows are indicating flow paths.

4.3 Variable injector

Pillsbury and Suter [54] used a rotary shutter (*Fig. 4.10*) for each injector of the combustion chamber in order to control additional air for the primary zone depending on the operating point. At low power needs the shutter is opened to prevent soot production. Additionally, the air is injected slightly tangentially for an enhanced circumferential velocity.

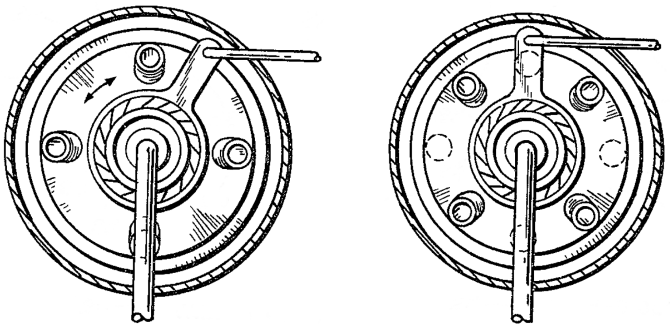

Fig. 4.10: Rotary shutter. Providing a lean primary zone when shutter is open (a) and a rich zone when shutter is closed (b).

Vaught [55] employed an axial swirler with an annular sleeve (1) indexed with air passages covering the housing of the swirler. Downstream of the swirler the housing had tangentially inlet slots (2) which could be freed by rotating the sleeve (*Fig. 4.11*). This additional angular momentum helped to stabilize the combustion process throughout the operational envelope.

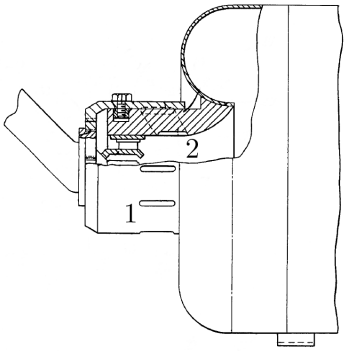

Fig. 4.11: Variable swirler with annular sleeve

Sanders [47] employed a movable injector nozzle (1) in order to vary the exit area (2). This should ensure velocity levels high enough to prevent flashback (*Fig. 4.12*).

Zarzalis and Joos [17] designed a swirl generator with tangential inlet slots which can be altered in size by axially moving the profiles relative to one another. One section of a profile is to be a hollow body in which the corresponding section engages in a movable manner (*Fig. 4.13*). Depending on the operating conditions an optimum swirl strength can be set.

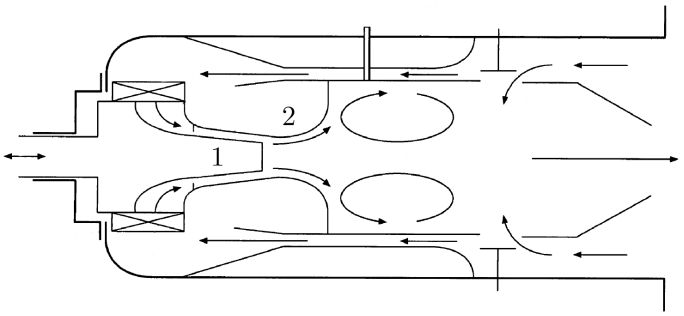

Fig. 4.12: Movable fuel injector for optimal velocity levels throughout the operational envelope. Arrows are indicating flow paths.

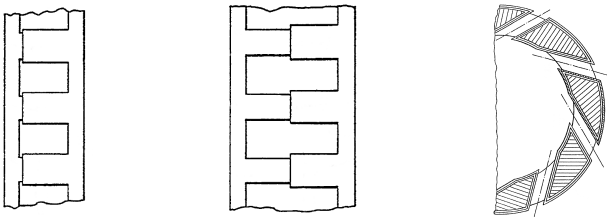

Fig. 4.13: Axially adjustable swirler. Minimum flow cross-section (a), maximum flow cross-section (b), partial circumferential cross-sectional view illustrating the wedge-shaped profiles (c).

4.4 Orifices and diaphragms

Barbier et al. [45] used spinning baffles in order to control the atomization air of an injector depending on the operating conditions (*Fig. 4.14*). The system allowed varying the air flow from 5 to 20 % of the total incoming air flow for low speeds and full power, respectively. This ensured high efficiency and stability of operation at low power needs and reduced maximum temperatures and smoke emission at wide open throttle.

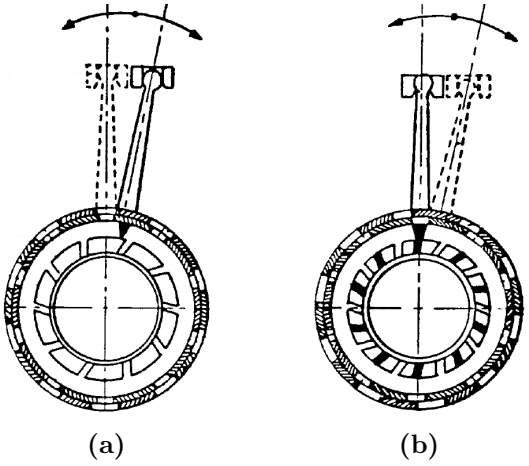

Fig. 4.14: Sectional view of the injector applying spinning baffles. Wide open throttle conditions (a), low-speed mode of operation (b)

Ciccia and Lancelot [46] equipped swirl generators with control diaphragms (1) and closure plates (2), both actuated by a sliding member (3), in order to control the air flow at the swirler (*Fig. 4.15*). Depending on the operating conditions, when the diaphragms are in their maximum flow position the additional intake orifices are closed by the closure plates and vice versa.

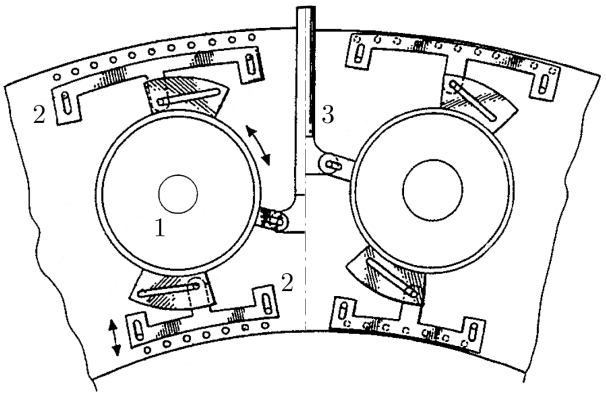

Fig. 4.15: Variable oxidizer intake. The diaphragms and closure plates are used to control the air flow at the swirl generators depending on the operating conditions. Left of the centerline: minimum flow position of the diaphragm, right of the centerline: maximum flow position of the diaphragm.

Chapter 5

Measurement techniques

Measurements in reacting flows, or more specifically in flames, are always critical as mechanical probes are exposed to heat and heat release fluctuations. Due to the intrusive nature of the measurement devices the flame and its dynamics are influenced and the results may not be reliable. As a consequence, non-intrusive optical and laser-based measurement techniques such as the schlieren technique, particle image velocimetry, interferometric measurement techniques, light emission measurements, and Raman spectroscopy, have been used here to investigate the behavior of the variable geometry burner. Incentive has been put on:

- Flame shape and position
- Injection dynamics
- Turbulence
- Temperature

5.1 Schlieren visualization

Schlieren visualization is a technique which uses the property of light waves when traveling through a transparent medium. If the waves encounter different refractive indices they are decelerated and deflected. Projected on a screen, bright and dark areas can be observed. The schlieren technique qualitatively visualizes gradients of density and comprises the whole field of view. Combustion processes as well as flow phenomena like shock waves can be visualized. The latter was one of the first applications of the schlieren technique. As early as 1887 Mach and Salcher [56] used this method to visualize the flow field around a supersonic bullet. This was possible as a simple optical setup and a white light source are sufficient.

5.1.1 Fundamentals

Light is commonly described by the wavelength λ and the frequency f when considered as a wave. The product of wavelength and frequency is the speed of light c. In vacuum c equals $2.998{\cdot}10^8$ m/s. If light is traveling in a medium the frequency remains constant, hence, λ and c change. The ratio of the speed of light in vacuum to the speed of light in a medium is denoted as refractive index n and is always greater than unity. A typical value of n for air under atmospheric conditions is 1.00029 [57]. At the interface of two different media the light beam is de- or accelerated and deflected depending on the optical properties and on

the angle of incidence. The relation between refractive index n and the density ρ is called Gladstone-Dale constant G, which is more described in detail in *Sec. 5.4*. This relation is useful as the deflection of a light beam in a medium can be estimated according to [58] as follows:

$$\varepsilon_x = \frac{G}{G\,\rho + 1}\,\frac{\partial \rho}{\partial x}\,(\zeta_{out} - \zeta_{in}) \tag{5.1}$$

$$\varepsilon_y = \frac{G}{G\,\rho + 1}\,\frac{\partial \rho}{\partial y}\,(\zeta_{out} - \zeta_{in}) \tag{5.2}$$

where ε_x and ε_y denote the deflections in x and y direction, respectively. The difference $\zeta_{out} - \zeta_{in}$ is the thickness of the medium investigated. *Equation (5.1)* and *Eq. (5.2)* are obtained assuming that the total deflection of the light ray is small and hence $\tan\varepsilon \approx \varepsilon$. Projecting the beam on a recording plane at a distance L and observing the displacements Δx and Δy, the deflections in the form as stated above, can be gained. As already mentioned, the schlieren technique visualizes the deflections ε_x and ε_y, ergo $\partial n/\partial x$ and $\partial n/\partial y$, which are the first spatial derivatives of the refractive index n in x and y direction.

To do so, a point shaped light source together with a lens system is used to provide parallel light rays within the measurement volume. In the focus of the second lens a schlieren stop (aperture) is placed which either blocks the parallel light rays or allows them to pass. The first option is called dark-field schlieren technique (*Fig. 5.1a*), the latter bright-field schlieren technique. The dark-field schlieren technique is more sensitive as only the deflected rays are visualized but needs a stronger light source. In applications where strong density gradients occur, e.g. in flames, the schlieren stop can be replaced by the aperture of a video camera, as the deflections are relatively high (*Fig. 5.1b*).

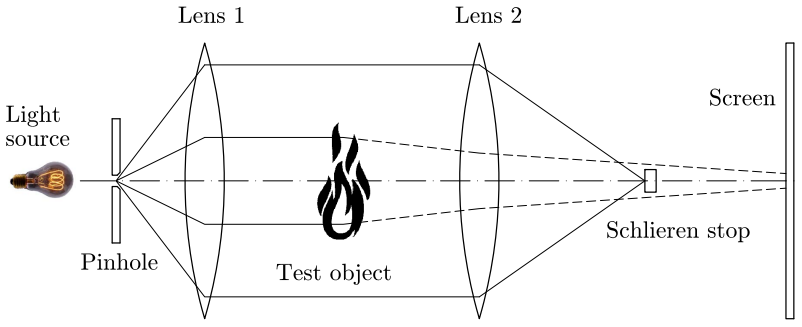

(a)

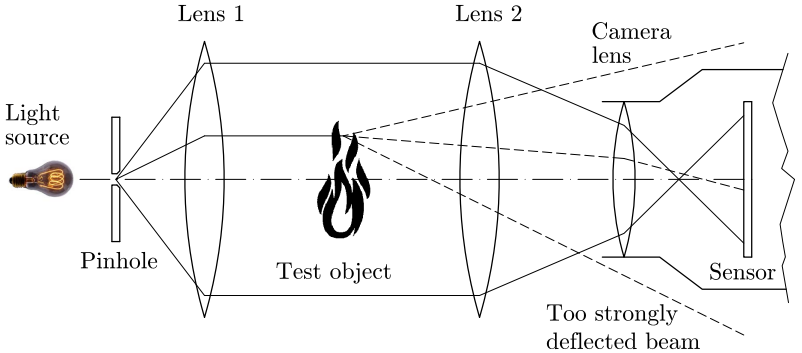

(b)

Fig. 5.1: Schlieren technique. Dark-field schlieren technique (a). Schlieren system applying a camera acting as schlieren stop (b).

5.1.2 Schlieren system

As a light source a slide projector was used. Depending on the exposure time, gray (short exposure time) or dark (long exposure time) filters were used (*Fig. 5.2*). The light beam was guided through a pinhole of about 2 mm in diameter. A plane mirror deflected the light beam onto a parabolic mirror with a focal length of $f_L = 2032$ mm which created a parallel light beam going through the measurement volume. The succeeding parabolic mirror ($f_L = 2032$ mm) focused the light beam on the CCD chip of the video camera employed (Panasonic NV-DX100EG). Prior to this, the light beam was deflected by a second plane mirror. For standard schlieren images an exposure time of 1/8000 sec was chosen. For images showing both the natural light emission and schlieren, an exposure value of 1/50 sec was set. In order to prevent interlacing, the camera had to be operated in the progressive scan mode. This setting was also to be made in the video recording software Magix Video deluxe 16 Plus. On average 300 frames were recorded per projection of an operating point.

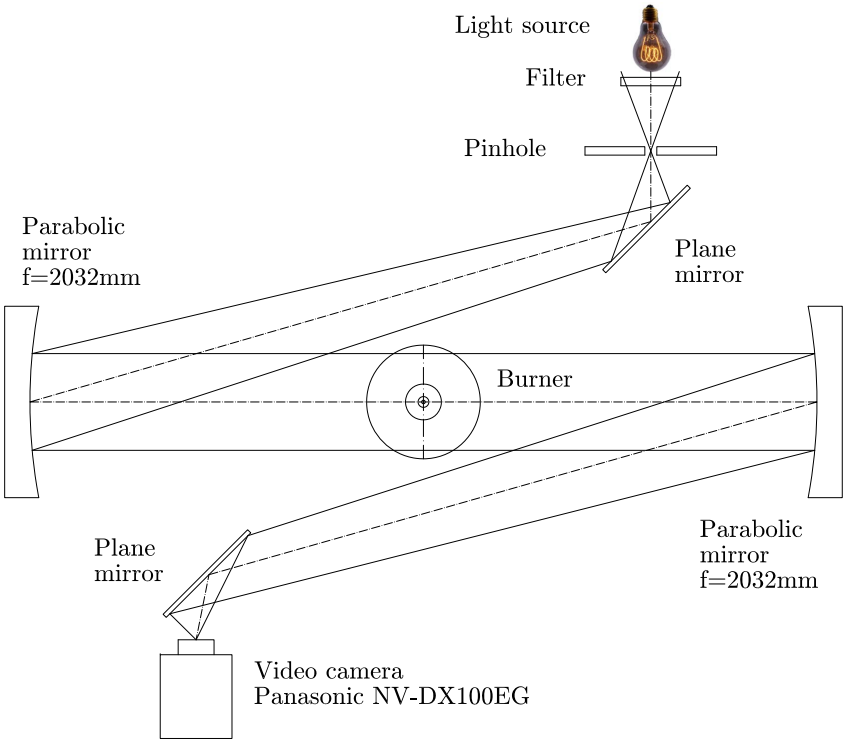

Fig. 5.2: Schlieren layout used for the measurements on the variable geometry burner.

5.2 Particle image velocimetry

Particle image velocimetry (PIV) is a planar laser measurement technique which allows the determination of the whole flow field in either isothermal or reactive flows. The technique determines the displacement of particles within a well defined time interval to obtain the velocity vectors. For that a laser light sheet, appropriate tracer particles, and at least one camera are necessary. The tracer particles can be liquid or solid particles, the latter are used for PIV applied in flames or reactive flows. Depending on the application, two

component PIV (2C PIV) or three component PIV (3C PIV) setups are possible. The first applies one camera and allows the determination of the velocity components within the laser light sheet. The latter uses two cameras, both looking at the laser light sheet under certain angles and hence the third velocity component can be calculated applying special algorithms.

5.2.1 Fundamentals

Upstream of the measurement area the seeding material has to be fed into the flow. This can be realized either by introducing the seeding directly into the flow channel or by introducing it into one of the supply lines as it was done at the variable geometry burner. However, attention has to be paid that the mixing distance for the seeding material and the working fluid is sufficient long in order to obtain a homogeneous mixture. In the measurement plane a pulsed laser produces two bursts with a temporal spacing of Δt which enlight the particles (pulse duration 3-5 ns). The scattered light is caught by a charged coupled device (CCD) camera. The camera is triggered by the laser system and writes two frames into one image recording. Each frame of an image recording is then divided into interrogation areas and the corresponding areas of frame 1 and frame 2 are then correlated. The result of the correlation is the displacement vector. With the help of Δt the velocity components can then be obtained. Prior to this, a calibration procedure has to be performed in order to get the right scale of the displacement vector. This is done mainly by employing a calibration target which defines the image scale. For 2C PIV measurements one calibration image is sufficient. Three component PIV needs at least three images per camera, shifted perpendicular to the laser light sheet, in order to calculate the image scale. The thickness δ of the laser light sheet and the temporal spacing Δt mainly depend on the prevailing velocity field within the measurement area. Common values for δ and Δt are 2 mm and 100 μs, respectively, for moderate velocities at the order of 10 m/s. By using 3C PIV the Scheimpflug condition has to be met. As the cameras are positioned under certain angles to the laser light sheet, the CCD chip plane, the object plane, and the imaging lens plane have to intersect in a common line in order to obtain a focused image.

5.2.2 PIV system

The main parts of the PIV system are a laser light source, CCD cameras, a controller, and a personal computer (PC) for the data acquisition (*Fig. 5.3*). The laser light source is a pulsed Nd:YAG laser (New Wave GEMINI, Sunnyvale, California) producing laser bursts at a wavelength of 532 nm (green light) with a duration of 3-5 ns and a maximum energy of 120 mJ at a repetition rate of 15 Hz. As two separate laser-resonators (double cavity) are employed the time between the laser bursts can be set depending on the investigated flow field. In this case here, the time interval was set to 100 μs. A light guide arm and a light sheet probe (spherical lens with $f_L = 600$ mm, cylindrical lens with $f_L = -10$ mm), which is described in detail in [59] produced the light sheet with a thickness δ of 2 mm. The cameras employed from Dantec of type 80C60 HiSense had a resolution of 1280×1024 pixels, a dynamic range of 12 bit and were operated in the double-frame mode. They were mounted on a Scheimpflug-mount and used AF-Micro Nikkor 60/2.8 lenses resulting in a field of view of 50×50 mm. The angle between the cameras was 60° and the distance to the burner center axis was 370 mm. As the natural light emission of the flame would have

caused overexposed images interference filters (Dantec) centered at 532 nm with a bandwidth of 10 nm have been used. The controller (Dantec, FlowMap 1500) was necessary for the image acquisition and the synchronization of laser bursts and cameras. The communication between the controller and the PC (Windows NT 4.0, FlowManager 4.60.28) was established via a 100 Mbit ethernet connection. As tracer particles for isothermal investigations Di-Ethyl-Hexyl-Sebacat (DEHS), which is a non-soluble, colorless and odorless liquid was used which produced particle sizes of the order of 0.5 μm. For reactive investigations titanium dioxide (TiO_2) was used which produced particle sizes of about 0.8 μm. For DEHS an aerosol-generator from Palas of type AGF2.0D was used. When using TiO_2, a Pivtec PivSolid 3 seeding generator was employed. In all cases, the tracer particles were injected into the axial air supply of the burner shortly before the air distribution box. In total 1200 double-frame images have been taken at an operating point to obtain a sufficient number of validated vectors as the natural light emission of the flame was influencing the camera images despite the interference filters used. Additionally, in recirculating zones the concentration of tracer particles was weak.

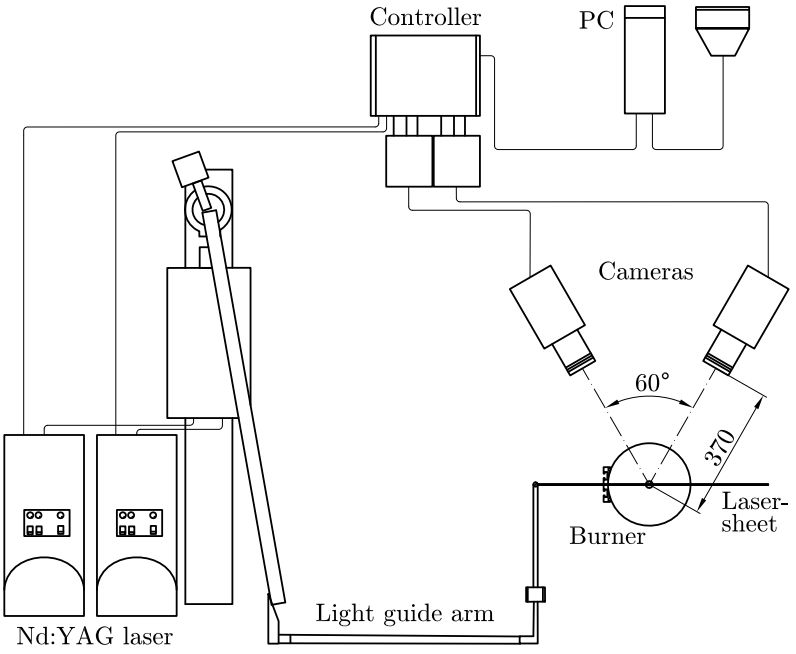

Fig. 5.3: 3C PIV setup

5.2.3 Postprocessing

Postprocessing of the images is done via cross-correlating the corresponding interrogation areas of the two frames of an image recording. The cross-correlation R can be defined as follows [60]:

$$R_{(m,n)} = \sum_{i=1}^{M} \sum_{j=1}^{N} g_{1(i,j)}\, g_{2(i+m,j+n)} \tag{5.3}$$

where g_1 and g_2 denote as the grayscale intensity distribution of frame 1 and frame 2, respectively, M and N as the size of the interrogation areas, whereas i, j, m, and n are integers indicating the coordinates within the interrogation area. The calculations were

performed in the frequency domain and the result of $R_{(m,n)}$ is the mean displacement distribution of the tracer particles within the interrogation area. The size of the interrogation areas was chosen to be 64x64 pixels with an overlap of 50 %. The software package used was the Dantec FlowManager 4.60.28.

However, due to erroneous correlations, displacement vectors are obtained which are evidently incorrect. Therefore, three validation criteria were used to eliminate those vectors. These have been peak, range, and moving average validation. At the peak validation the correlations were eliminated if there was no distinct difference between the two highest correlation peaks. The default peak-height-ratio was set to 1.2. The range validation removed unrealistic vectors by fixing range limits for displacement and velocity. At the moving average validation adjacent vectors were compared. If the vector investigated exceeded a specified limit ($7 \times$ standard deviation) it was rejected.

5.2.4 Calibration

For the calibration procedure a calibration image was positioned in the laser light sheet. It was a white 100×100 mm plate with black dots equidistantly distributed in horizontal and vertical direction. The center marker was 2 mm in diameter, the axis markers were 1 mm and the normal markers 1.5 mm in diameter. For 2C PIV one calibration target was sufficient to calculate the image ratio. For 3d PIV the target was moved back and forth perpendicular to the light sheet in steps of 0.5 mm. In total three calibration images for stereo PIV were taken at $z = -0.5, 0, 0.5$ mm with respect to the center of the laser light sheet. At every position an image was taken in order to obtain the information necessary for the reconstruction. The procedure was always performed before the measurement campaign started.

5.2.5 Uncertainties

The uncertainty of the in-plane results calculate to 2 %, as a dynamic range of 50 was used. According to [61], the uncertainty ratio S_{op}, which is the ratio of the out-of-plane error and the in-plane error of 3d PIV can be estimated as:

$$S_{op} = \frac{1}{\tan(\alpha/2)} \tag{5.4}$$

where α denotes the angle of the optical axes of the PIV cameras. Applying *Eq. (5.4)*, for an angle of 60° S_{op} equals $\sqrt{3}$, which means that the out-of-plane error is 1.73 times higher than the in-plane error, which can be estimated by assuming a normal distribution of independent measurement values [62].

Although interference filters centered at the wavelength of the laser were applied, the natural light emission of the flame was still influencing the camera images. Furthermore, the concentration of tracer particles in recirculating zones was weak. Therefore, 1200 images per operating point investigated were taken in order to obtain a sufficient number of validated vectors in the weak zones.

5.3 Light emission

5.3.1 Fundamentals

Light emission measurement through detection of CH^*, OH^* or C_2^* radicals in hydrocarbon flames is a well known technique to gain information about the flame front and the heat release rate. Light is emitted when excited species fall back to a state of lower energy. Depending on the prevalent species, light at characteristic wavelengths is recorded, e.g. OH^* emits light at 309 nm, CH^* at 431 nm, and C_2^* at 519 nm. In lean flames mainly OH^* and CH^* are observed giving the flame a blue hue, in rich flames the intensity of C_2^* is higher, making the flame greenish [63]. If soot particles occur the flame emits light in the yellow range. In order to reduce the influence of parasitic light, narrow band-pass filters are often applied.

Light emission measurement works well in premixed flames [64, 65], however, the emission depends on local equivalence ratio [66–69], turbulence intensity [69, 70], flame front properties [71], and temperature and pressure [72–75]. To obtain quantitative information of the heat release rates, the signals have to be calibrated [69, 76, 77]. Furthermore, the information obtained through these measurements are integrated values along the line-of-sight which makes it necessary to use deconvolution methods to obtain spatial resolved data. Either an Abel transform [78–80] or tomographic reconstruction techniques [81, 82] are eligible.

5.3.2 System

The images for the light emission measurements were taken with the video camera Panasonic NV-DX100E. The camera was placed at a radial distance of 1350 mm from the central burner axis. In order to reduce parasitic light a band-pass filter from Thorlabs of type FB25S was used. It allowed light with wavelengths of 315–445 nm and 715–1095 nm to pass, hence, focussing on the intensity of the CH^* radical. A second filtering process was applied afterwards by taking only the blue channel of the RGB images. Each recording per projection consisted of 300 frames. The camera was operated in the progressive scan mode. Exposure time, aperture, and gain were set to 1/100 sec, f/0.0, and 6 dB, respectively. The software used for performing the recordings was Magix Video Deluxe 16 Plus Special edition. From each recording per projection a mean image and an image of the root-mean-square (RMS) values have been created in Matlab R2009b. Hence, for one operating point 18 images (10° spacing) of the mean and RMS values were obtained (*Fig. 5.4*), which were then loaded into the software program IDEA 1.7. IDEA is a digital fringe evaluation software described in [83, 84], which was developed at Graz University of Technology. This software performed the tomographic reconstruction to obtain local data. The procedure approximated the so-called Radon Inversion (*Eq. (5.5)*), named after the Austrian mathematician Johann Radon) by applying a convolution which eliminated the direct calculation of the derivation within the integral [85]. The explanation of the notation of the following equation is given in *Fig. 5.5*.

$$f(r,\varphi) = \frac{1}{2\,\pi^2} \int_0^{\pi} d\theta \int_{-\infty}^{+\infty} dp \, \frac{1}{r\,\cos(\theta-\varphi)-p} \, \frac{\partial h(p,\theta)}{\partial p} \tag{5.5}$$

In literature the method is also known as 'Filtered Backprojection with Convolution' and can be interpreted as a differentiation of the projections, a subsequent Hilbert transform, and a closing backprojection. The algorithms used by this software are described in detail in [85, 86]. The local data have been visualized with the help of Matlab R2009b. In *Fig. 5.6* the intermediate images as well as the final image of the postprocessing procedure are depicted.

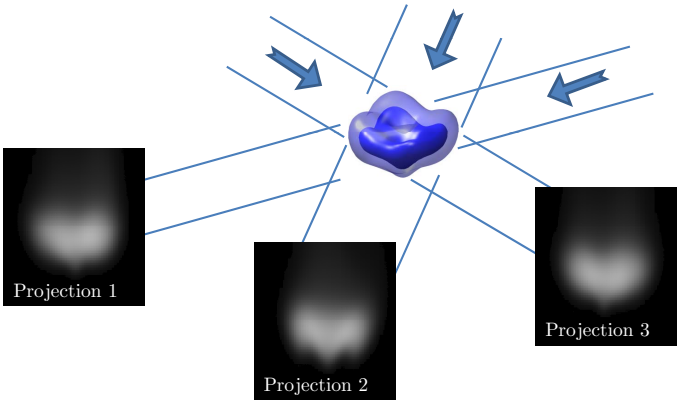

Fig. 5.4: Mean images of the light emission of a flame of different projections for further processing in IDEA to obtain local data.

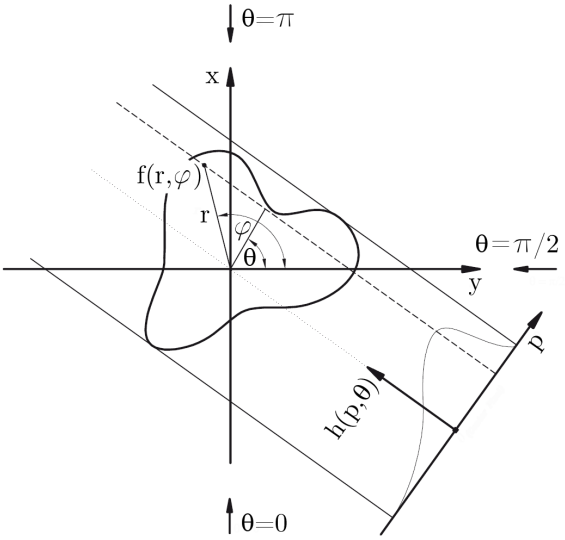

Fig. 5.5: Notation for the Radon Inversion [85]. Local data $f(r, \varphi)$ are reconstructed from one-dimensional data $h(p, \theta)$. Viewing directions are indicated by arrows at $\theta = 0$, $\pi/2$ and π.

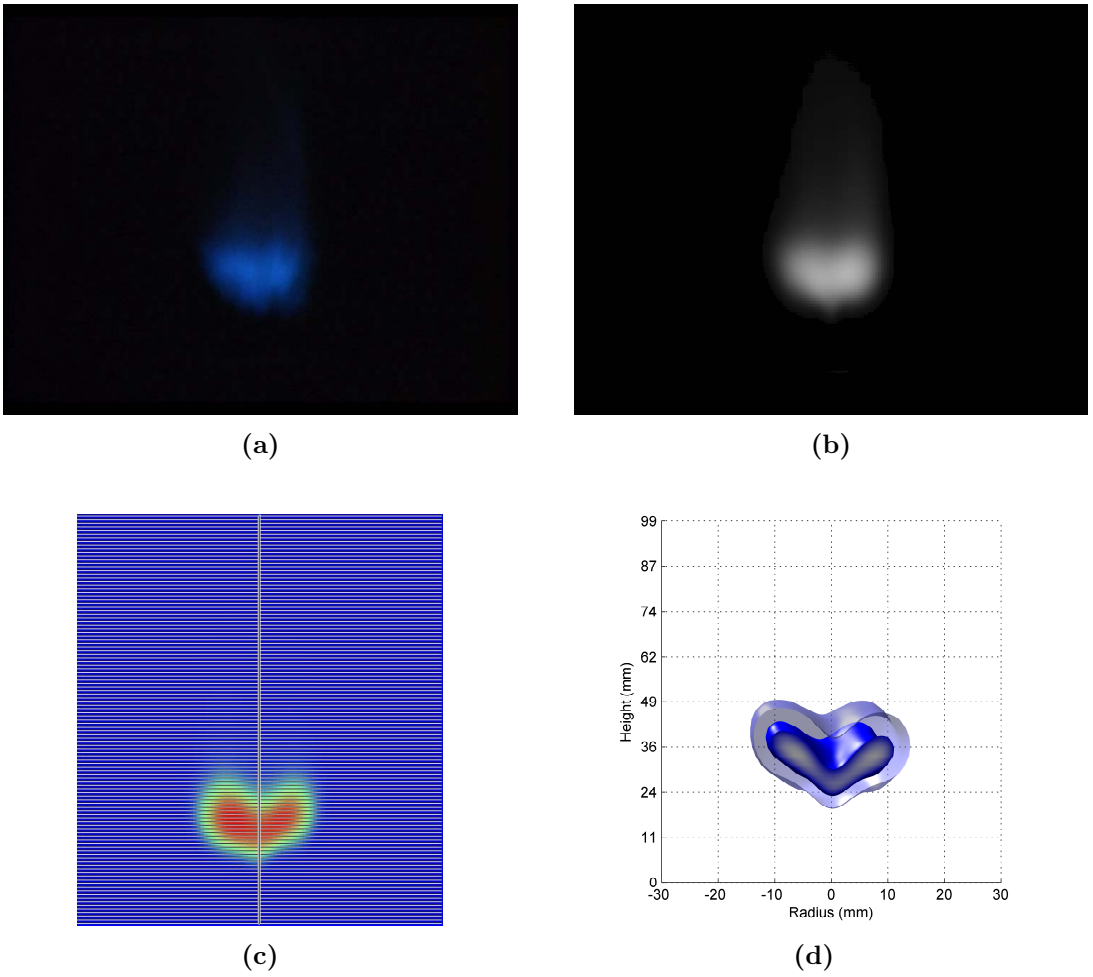

Fig. 5.6: Light emission post-processing steps. Single image (a) and averaged image obtained from 300 single frames. (b). Averaged image of one direction after importing into IDEA. Also shown are the horizontal planes in which the local data are calculated (c). Visualizing the flame by displaying iso-surfaces of light intensity for two arbitrary values in Matlab R2009b (d).

5.3.3 Sensor characteristics

As the sensor of the video camera (Panasonic NV-DX100E, H8HYO1974) showed nonlinear behavior all images have been corrected according to *Fig. 5.7*, where the grayscale intensity of the blue channel with respect to the energy can be found. The settings have been 1/50 sec, f/0.0, and 6 dB for exposure time, aperture and gain, respectively. The curve was obtained by employing a white light source (halogen lamp) and combinations of neutral filters with different optical thicknesses (0.1, 0.2, 0.3, 0.4, and 0.5) from Melles Griot (Irvine, California, USA), covering an optical thickness range of 0.1 to 1.5.

The sensor seems to behave like a technical film as the range of operation at these settings spans only one order of magnitude. This behavior results in a narrow exposure latitude but provides good performance in terms of contrast. In the case here, the emittance of the flame in W/m^2 results in an irradiation in W/m^2 of the camera sensor. This value multiplied by the exposure time results in an energy in $W\,s/m^2$, which is captured by the

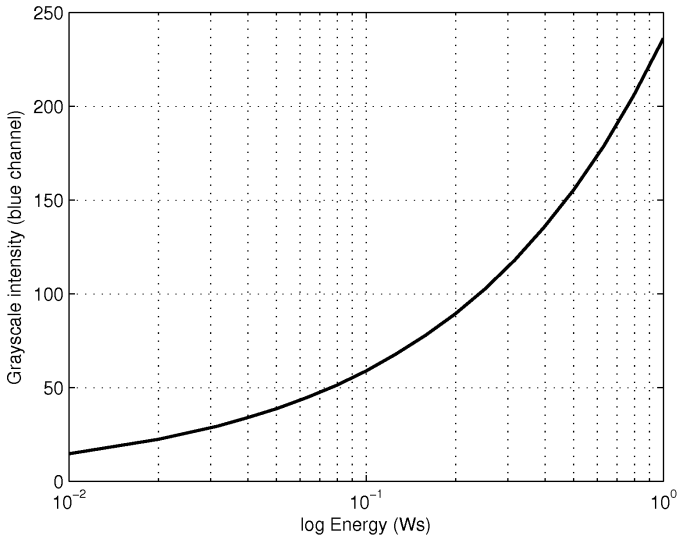

Fig. 5.7: Characteristic curve of the Panasonic NV-DX100E video camera. The graph is approximated through the equation $y = 236.0111 \cdot x^{0.6038}$

chip. Depending on the field of application, luminance in $\mathrm{cd/m^2}$ is equivalent to irradiation, exposure in lux·s to energy, and density to grayscale intensity.

5.3.4 Uncertainties

With the camera settings used a signal-to-noise ratio (SNR) of 4.4 can be calculated. A measurement uncertainty of ±3.5 % was estimated for a 95 % confidence interval and 300 images to average [62].

5.4 Laser interferometric vibrometry

Laser interferometric vibrometry (LIV) relies on the ability of monochromatic light to interfere. Devices performing LIV are called laser vibrometers (LV) and were originally used to detect surface vibrations. A LV is a compact device which basically consists of a laser, a Mach-Zehnder interferometer, a photo-detector, and a decoder-unit.

5.4.1 Fundamentals

The generated laser beam is split into a reference and an object beam. The object beam is reflected on the surface to be investigated and re-enters the LV through the aperture while the reference beam remains in the sensing head comprising the laser and the Mach-Zehnder interferometer. As the object and reference beam interfere in the sensing head, changes in the geometrical beam path lead to intensity variations which are detected by the photo-detector. Assuming a constant refractive index n, surface vibrations can be determined [87, 88]. By replacing the vibrating surface by a rigidly fixed mirror, keeping the geometrical beam path constant, changes in refractive index n can be used to determine density variations ρ' within the measurement volume [89].

The LV employed here were equipped with a Bragg cell which is an acousto-optical modulator. It diffracts and Doppler shifts the reference beam using sound waves created by a piezoelectric element. When the frequency modulated reference beam and the object beam interfere a beat frequency is detected even if the optical beam path remains unchanged. The detected beat frequency acts as a carrier frequency of the output signal of the photo-detector and is modulated by changes in optical path length of the object beam. In this mode, the vibrometer velocity mode, the rate of change of the signal is detected rather than the absolute value which improves the signal-to-noise ratio by the factor $2\,\pi\,f$ compared to the common displacement mode. The frequency spectrum in *Fig. 5.8* depicts the difference between these two modes [90]. Clearly visible is the higher sensitivity of the velocity decoding mode at higher frequencies.

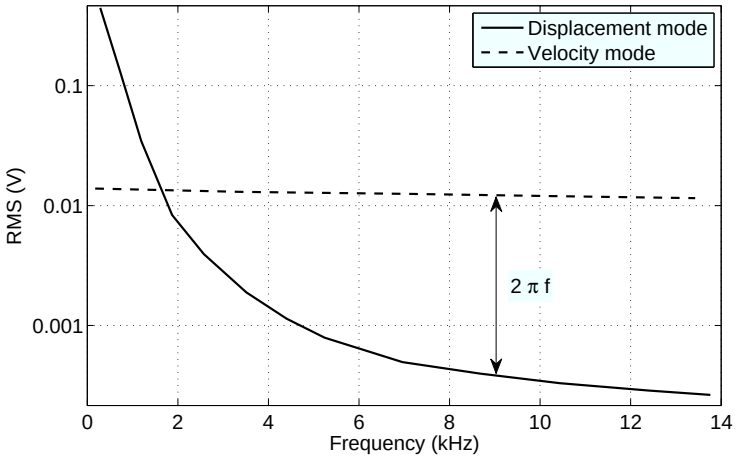

Fig. 5.8: Comparison between displacement (solid line) and velocity (dashed line) decoding mode of the LV.

In an optical thin medium where the difference between the refractive index n and unity is much less than unity, the relation between density ρ and the refractive index n can be written as follows [91]:

$$n - 1 = G\,\rho \tag{5.6}$$

where G denotes the Gladstone-Dale constant in m^3/kg. A change in density within the time interval $\triangle t = t_1 - t_2$ will result in a change in refractive index $\triangle n$ and thus in a change of the optical path $\triangle L$ detected by the LV:

$$\triangle L(t) = \int_x (n_{t_1} - n_{t_2})\,dx \tag{5.7}$$

Substituting *Eq. (5.6)* in *Eq. (5.7)* and assuming that the Gladstone-Dale constant G remains unchanged along the line-of-sight, leads to:

$$\triangle L(t) = G \int_x \rho'(t)\,dx \tag{5.8}$$

Between reference and object beam in the interferometer a phase difference $\triangle\phi$ is measured depending on the optical path difference in both beams. Whenever the density starts to fluctuate in the object beam, the optical path changes accordingly and so does the phase at the detector:

$$\triangle\phi(t) = \frac{4\,\pi}{\lambda}\,\triangle L(t) \tag{5.9}$$

where λ is the laser wave length. The factor 4 accounts for the fact that the density fluctuation is passed twice by the object laser beam. Combining *Eq. (5.8)* and *Eq. (5.9)* leads to:

$$\triangle\phi(t) = \frac{4\,\pi}{\lambda}\,G \int_x \rho'(t)\,dx \tag{5.10}$$

Using the velocity decoder of the vibrometer the signal $U(t)$ is recorded:

$$\frac{\partial}{\partial t}\triangle\phi(t) = \frac{4\,\pi}{\lambda}\,\frac{\partial}{\partial t}\triangle L(t) = \frac{4\,\pi}{\lambda}\,k\,U(t) \tag{5.11}$$

where k is the vibrometer calibration factor. Combining *Eq. (5.10)* and *Eq. (5.11)* results in an expression for the density fluctuation (integral data):

$$\int_x \frac{\partial \rho'}{\partial t}\,dx = \frac{k}{G}\,U(t) \tag{5.12}$$

5.4.2 Local data

As mentioned above, LIV provides integral data of the rate of change of density fluctuations along the line-of-sight. For obtaining local data two interferometry units have been used which were aligned such that the two laser beams intersected in a single point. The angle between the two units was 90°.

Additionally, a signal correlation method was necessary, which could reveal information contained in two signals recorded at a time. Therefore, the Fourier transform was applied according to *Eq. (5.13)*, which decomposes an arbitrary signal into oscillatory functions by correlation of the time signal with complex oscillations $e^{-i2\pi f}$.

$$F_t(f) = FT\{X(t)\} = \int_{-\infty}^{\infty} X(t)\,e^{-i2\pi f}\,dt \tag{5.13}$$

The numerical computation of *Eq. (5.13)* is realized by the discrete fast Fourier transform algorithm (FFT) which is optimized for sample lengths $N = 2^m$, where m is an integer value.

The fundamental idea of the correlation method is to calculate the correlation function R_{12} of two signals X_1 and X_2 in the time domain (*Eq. (5.14)*). The factor $1/T$ accounts for the signal length and τ is the time-shift of the second signal X_2. If both signals contain a correlated part which is shifted by τ_0, the maximum of the correlation function can be found at $t = \tau_0$ on the time axis.

$$R_{12}(\tau) = \frac{1}{T}\int_0^T X_1(t)\,X_2(t+\tau)\,dt \tag{5.14}$$

The calculation of R_{12} is performed in the frequency domain by calculating a cross spectrum, as the multiplication and the following integration in the time domain are reduced to a single multiplication, as shown in *Eq. (5.15)*.

$$C(f) = F_1(f)\,F_2^*(f) = FT\{R_{12}(\tau)\} \tag{5.15}$$

Here, $C(f)$ denotes as the cross spectrum. It is the product of the spectrum $F_1(f)$ of a signal and the complex conjugate spectrum $F_2^*(f)$ of the other, which is marked by an asterisk. The cross spectrum can be interpreted as the coupling strength of both spectra. Its magnitude denotes as the power spectrum of the correlated fraction, the complex angle of the cross spectrum is the phase difference between the equal parts contained in both signals.

If the signals are completely random, magnitude and phase will average out. However, as the signals are of turbulent and stochastic nature, a statistical approach was necessary to extract the deterministic part. Averaging of complex spectra was therefore applied. The time signals were cut into sets of equal length and a fast Fourier transform was done to obtain an ensemble $\{F\}$ of complex spectra F_i for each signal. Subsequently, from every spectra F_i, magnitude and phase at frequency f_j are taken to build an ensemble $\{F_i(f_j)\}$. The cross spectrum of two ensembles $\{F_1(f)\}$ and $\{F_2(f)\}$ can be defined according to *Eq. (5.16)*.

$$\overline{\{C(f)\}} = \overline{\{F_1(f)\, F_2^*(f)\}} \tag{5.16}$$

However, there are several parameters which can influence the results of the LIV measurements. Sound waves and spatially separated but correlated fluctuations may produce artefacts which have to be identified. This can be done via a Gaussian filter function which corrects the cross spectrum, as shown in *Eq. (5.17)*,

$$C_F(f) = C(f)\, e^{-\left(\frac{\varphi(f)}{\Delta\varphi(f)}\right)^2} \tag{5.17}$$

where $C_F(f)$ is the filtered cross spectrum, $\varphi(f)$ the phase and $\Delta\varphi(f)$ the filter width. Another possibility is to perform measurements from different directions damping the unwanted peaks by averaging. Scanning from different viewing angles is advantageous when the phase lags between correlated artefacts are rather small, making the Gaussian filter ineffective. Parasitic surface vibrations and electronic noise can be identified straightforwardly, as they produce an elevated cross spectrum for all scanned measurement points at single frequencies.

5.4.3 LV system

The LV from Polytec (Waldbronn, Germany) consisted of the sensing head (OFV-353) and the controller (OFV-3001). It was operated in the velocity decoding mode. The settings for the laser vibrometers are shown in *Tab. 5.1*. In front of the aperture a collimation lens was mounted with a focal length of $f = -40\,\text{mm}$ forming a parallel laser with a diameter of approximately 2 mm. In order to reflect the object beam back to the aperture a mirror was placed at the opposite side of the measurement volume. The carrier frequency of the LV is 40 MHz.

Data acquisition was done with a National Instruments PXI chassis 1033 and an I/O board of type BNC 2110 (both National Instruments, Austin, Texas, USA). The software programs for data acquisition and controlling the LV were programmed in National Instruments LabVIEW 8.6. In order to perform the LV measurements, the burner was mounted on a 3-axis Dantec Lightweight traversing system. The accuracy of the system was $10^{-6}\,\text{m}$ and it was controlled through a RS 232 interface. The layout for the measurements can be seen in *Fig. 5.9*. Sampling frequency has been 16 384 Hz, 491 520 samples have been taken per measurement and spacing between two points was 3.5 mm. The input coordinates for

the measurement points were read from a tab delimited text file. A single row contained three tab delimited values (x, y, z), specifying one measurement point. In order to control the LV measurement quality a normalized signal-to-noise ratio was written into a separate file, which contained maximum, minimum, and mean value for each position. After moving to the next point, the data acquisition system waited for seven seconds before the actual measurement started in order to let the vibrations of the structure fade away.

Tab. 5.1: LV settings

Description	Value
Tracking filter	off
Velocity range	5 mm/s/V
Velocity filter	off
Displacement range	0.5 μm/V

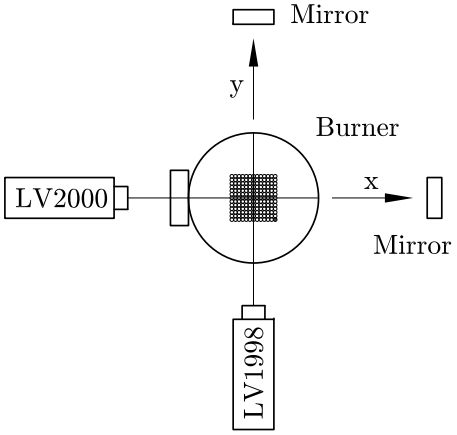

Fig. 5.9: Layout for the LV measurements. The variable geometry burner was mounted on a traversing system with the measurement grid fixed to the burner. The positive z-direction is pointing in the direction of flow.

5.4.4 Uncertainties

Generally the laser vibrometers used have a good signal-to-noise ratio. The biannual calibrations of the system estimated a set-value of 4.950 Vrms ±40 mV (full scale at 5 mm/s/V nominal scale factor, velocity decoder output). The signal quality is controlled by a diode array at the back-side of each vibrometer. Assuming a nearly full signal amplitude, when the light beam is reflected back by a mirror, a 25 % turbulence level and averaging over 240 single spectra, the uncertainty of the laser vibrometer signal can be given by ±3.5 % for a 95 % confidence interval.

5.5 Shearing interferometry

Shearing interferometry relies on the ability of coherent light to interfere. Light waves going through a measurement volume are afterwards superimposed and the obtained interference pattern allows the determination of the density gradient. The sensitivity of the system is set by the shear δ of the superimposed light waves (tilting one mirror). Basically, two arrangements of the optical setup are possible. At the first arrangement two sheared light beams are going through the test section and are afterwards imposed, at the second arrangement one light beam is going through the test section and is afterwards split in two equal portions which are then sheared in an interferometry unit (*Fig. 5.10*). Both arrangements deliver the same results.

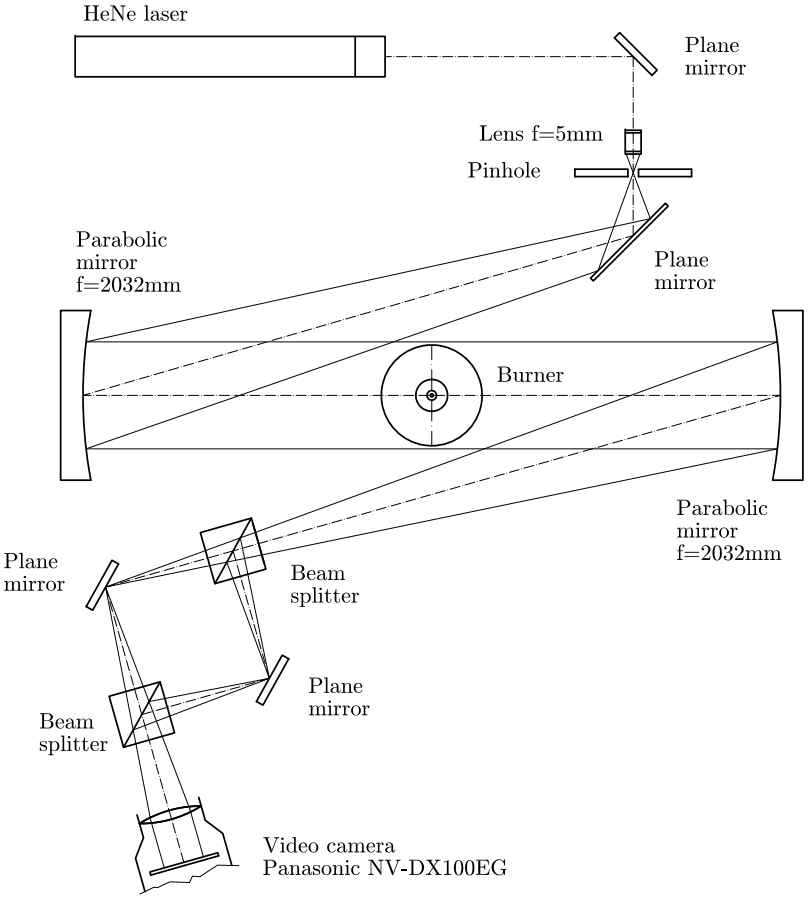

Fig. 5.10: Differential interferometry layout

5.5.1 Fundamentals

As for all techniques relying on interference, a coherent light source is needed. Coherence means, that there is no phase lag between light waves within a cross section of a light beam. Applying laser light (coherent light), a detected phase difference between two beams can either be caused by different geometrical paths or by different optical properties of the penetrated medium i.e. varying refractive index n along the line-of-sight. Hence, the

optical path l_{opt} can be defined which depends on the geometrical path z and the refractive index n.

$$l_{opt} = \int_{z_1}^{z_2} n(z)\, dz \tag{5.18}$$

By applying the Gladstone-Dale relation as stated in *Eq. (5.6)*, the phase difference $\Delta\phi$ can be calculated as follows:

$$\Delta\phi(x,y) = \frac{2\,\pi}{\lambda} \int_{z_1}^{z_2} (G\,\rho(x,y,z) + 1)\, dz \tag{5.19}$$

where x and y denote the coordinates perpendicular to the line-of-sight coordinate z and λ the wavelength. Furthermore, it is assumed that the Gladstone-Dale constant G remains unchanged in the whole measurement volume. This assumption is justified, as shown in previous works by [92] and [93]. Considering only the x-coordinate, the phase difference between two adjacent light waves can be written as:

$$\Delta\phi(x) = \frac{2\,\pi}{\lambda}\, G \int_{z_1}^{z_2} [\,\rho(x_0,z) - \rho(x_1,z)]\, dz \tag{5.20}$$

If the wave fronts are sheared by δ in x-direction *Eq. (5.20)* can be stated as:

$$\Delta\phi(x) = \frac{2\,\pi}{\lambda}\, G \int_{z_1}^{z_2} [\,\rho(x+\delta/2,z) - \rho(x-\delta/2,z)]\, dz \tag{5.21}$$

Dividing *Eq. (5.21)* by δ, replacing δ on the right hand side by Δx and assuming that δ is much less than unity, one obtains [94, 95]:

$$\frac{\Delta\phi(x)}{\delta} \approx \frac{2\,\pi}{\lambda}\, G \int_{z_1}^{z_2} \frac{\partial\rho}{\partial x} dz \tag{5.22}$$

The phase difference $\Delta\phi$ (proportional to the spatial density gradient) is obtained by evaluating the interferogram recorded by a video camera (*Fig. 5.11*). Therefore, a two-dimensional fast Fourier transform (FFT) is applied. As the signal containing the interferometric information $\mathfrak{B}$ is shifted to higher frequencies in the frequency domain by introducing the carrier fringe system, applying a filter (rectangular window) allows separation of the low-frequency background. A succeeding back-transformation of the filtered signal results in the phase distribution (*Eq. (5.23)*) of the wave front.

$$\Delta\phi(x,y) = \arctan \frac{Im\{\mathfrak{B}(x,y)\}}{Re\{\mathfrak{B}(x,y)\}} \tag{5.23}$$

The interferogram, FFT and filtering process, back-transformation, and the calculated phase distribution are shown in *Fig. 5.12*, which were created in IDEA 1.7. The shear δ has to be determined in a separate procedure. This was done by placing a calibration target in the measurement volume and measuring the displacement (in pixels) of the two images recorded by the video camera. For calculating the density distribution the density gradient has to be integrated numerically in shear-direction. As starting point for the integration an undisturbed position has to be chosen where $\partial\rho/\partial x = 0$. As the result is of integral nature

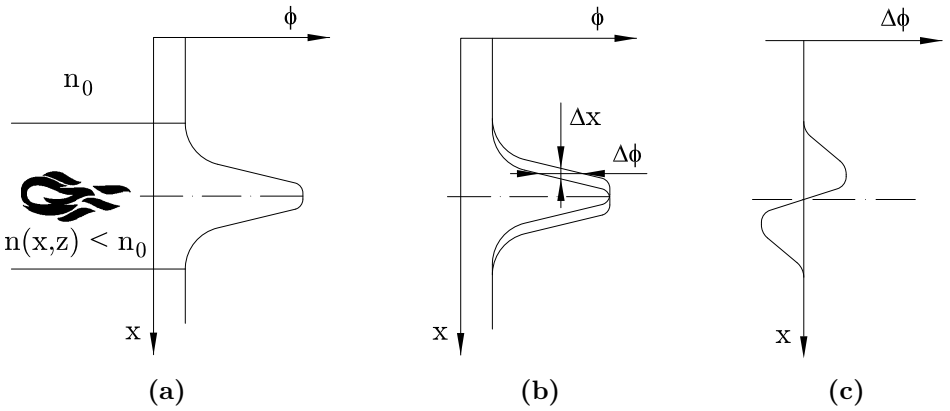

Fig. 5.11: Shearing interferometry fundamentals. An object distorts a plane wave front (a), splitting up into two beams afterwards and superimposing with the shear Δx (b), phase difference $\Delta\phi$ with respect to the image coordinate x (c).

along the line-of-sight coordinate z, local data are obtained by applying a tomographic reconstruction technique.

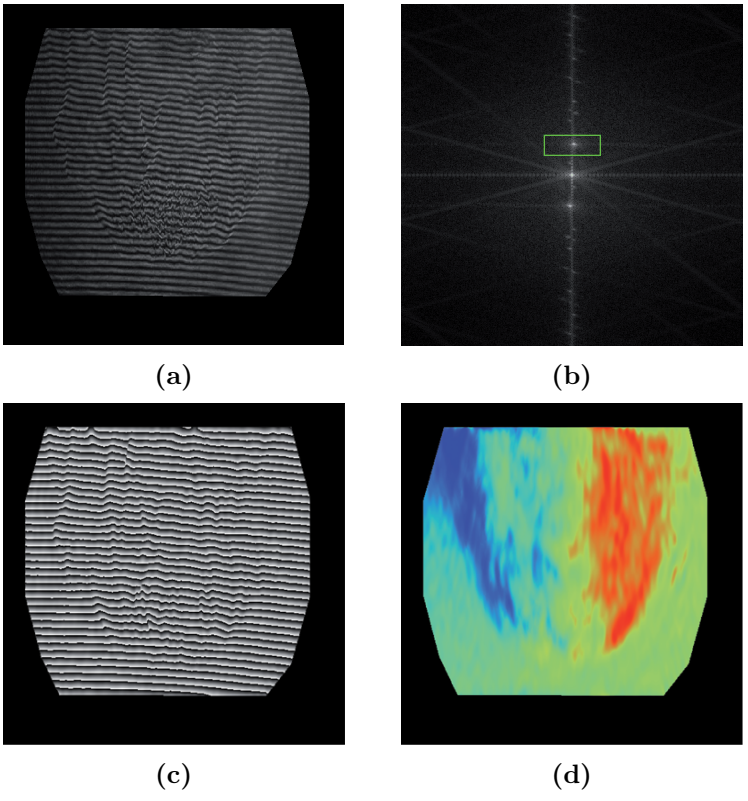

Fig. 5.12: Evaluation steps of the interferograms obtained through shearing interferometry [96]. Interferogram (a), FFT and filtering (b), back-transform (c), calculated phase distribution, linear tilt removed and averaged over 400 frames (d).

5.5.2 System

The layout of the measurement system is shown in *Fig. 5.10*. As coherent light source a continuous 20 mW HeNe laser was used ($\lambda = 632\,\text{nm}$). By means of a lens with a focal length of $f_L = 5\,\text{mm}$ and a pinhole with a diameter of $12.5\,\mu\text{m}$ the laser beam was expanded. Via parabolic mirrors ($f_L = 2032\,\text{mm}$) the now parallel beam is guided through the measurement volume and afterwards focused on one of the mirrors of the interferometry unit (Mach-Zehnder interferometer). Tilting one mirror introduces the shear δ between the two wave fronts (*Fig. 5.13a*). The shear is necessary for the evaluation and simultaneously sets the sensitivity of the system. By tilting one of the beam splitters (*Fig. 5.13b*) a carrier fringe system is produced as the wave fronts are inclined against each other by the angle α. The carrier fringe system can be set independently of the shear δ and is needed for the digital fringe evaluation process, as described above.

The interferograms were recorded by a Panasonic NV-DX100EG video camera at an exposure time of 1/8000 sec through the software program Magix Video deluxe 16. For the tomographic reconstruction algorithm applied afterwards, 400 frames were taken at every projection. In total 18 projections per operating point were investigated, which means steps of 10 degrees.

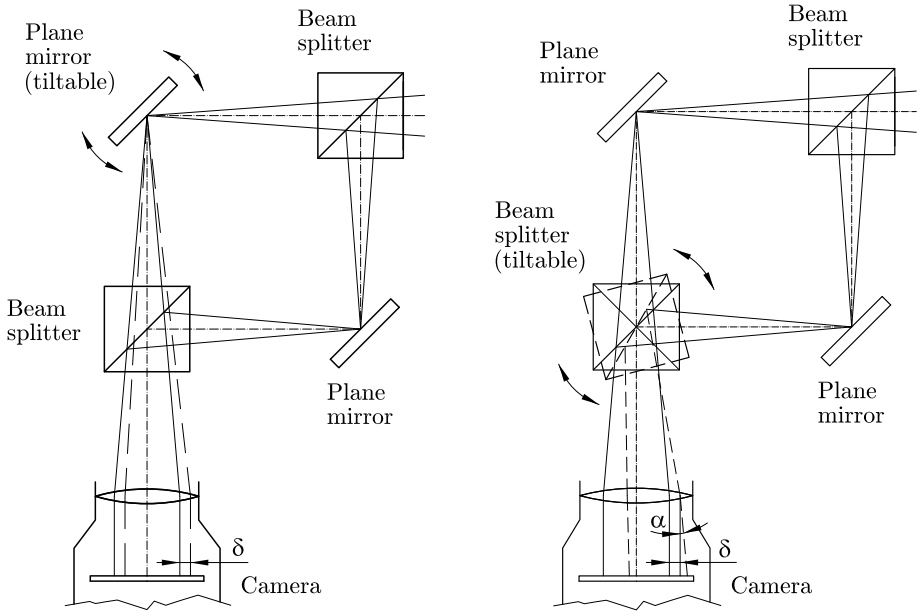

Fig. 5.13: Effects when tilting a mirror or a beam splitter of an interferometer unit. Tilting the mirror causes a shear δ. As the focal point lies on the rotational axis of the mirror the optical path length remains unchanged (a). By rotating the beam splitter an additional angle α is introduced producing a carrier fringe system (b).

5.5.3 Uncertainties

The main sources of uncertainty of this measurement technique are the determination of the shear δ and the signal-to-noise ratio, which imposes a phase-error during the FFT

process. This phase-error can be calculated according to [94], as shown in *Eq. (5.24)*.

$$\Delta(\Delta\phi) = \frac{1}{\mathrm{SNR}} \frac{\sqrt{\mathrm{SNR}} + 1}{\sqrt{\mathrm{SNR}} - 1} \tag{5.24}$$

Assuming a shear of 0.3 mm and a SNR of 3.5, a measurement uncertainty of $\pm 7\,\%$ can be estimated.

5.6 Raman spectroscopy

5.6.1 Fundamentals

If monochromatic light with the frequency f_0 is incident on transparent gases or liquids scattering will occur. By analyzing the frequency content of the scattered light, in addition to f_0 associated with the incident radiation (Rayleigh scattering), frequency pairs of type $(f_0 \pm f_M)$ are detected. This type of scattering where the frequency changes is called Raman scattering [97] and was first described in [98]. If the detected frequency is less than f_0 it is referred to as Stokes Raman scattering, if it is greater then f_0 it is called anti-Stokes Raman scattering. Stokes Raman scattering involves transitions from a lower energy level W_1 to a higher energy level W_2 (*Fig. 5.14*). Anti-Stokes Raman scattering is detected when transitions from W_2 to W_1 occur. By evaluating the ratio between Stokes Raman and anti-Stokes Raman scattering the temperature can be determined. However, temperature must be high enough to observe the anti-Stokes Raman bands as at room temperatures the ground energy levels are populated only. Therefore, anti-Stokes Raman scattering is about three orders of magnitude less than Stokes Raman scattering.

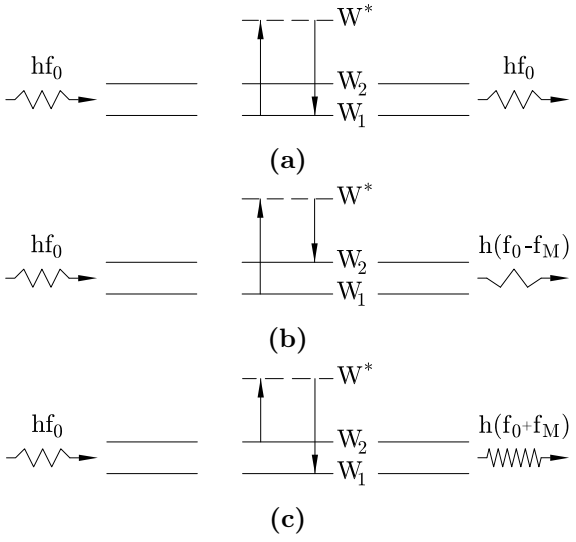

Fig. 5.14: Types of scattering. Rayleigh scattering (a), Stokes Raman scattering (b), anti-Stokes Raman scattering (c). The vibrational energy levels are denoted as W_1 and W_2, the virtual energy level as W^*.

The detected frequency bands constitute the so called Raman spectrum (*Fig. 5.15a*). The scattered light is polarized and the intensity as well as the polarization depend on the direction of observation. Furthermore, the intensity also depends on the physical state

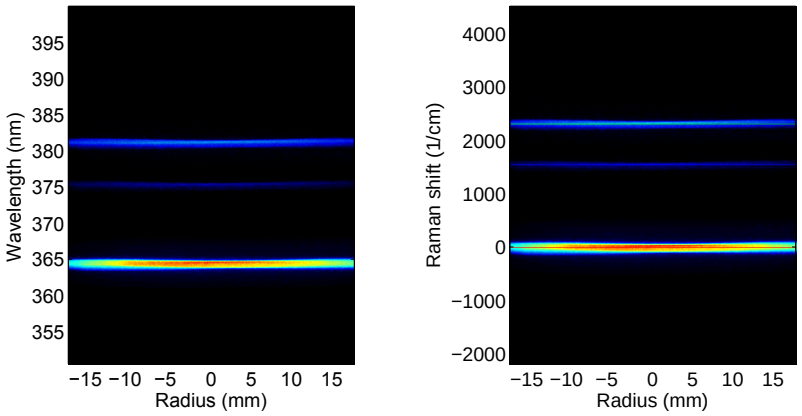

Fig. 5.15: Raman spectrum of air at room temperature (a) and Raman shifts obtained after scaling (b). The Rayleigh signal in (b) can be found at $0\,\mathrm{cm}^{-1}$, the Stokes Raman band for oxygen is located at $1555\,\mathrm{cm}^{-1}$ and the band for nitrogen at $2331\,\mathrm{cm}^{-1}$.

and the chemical composition of the fluid [97], which means, Raman scattering can be used to evaluate temperature and species concentrations as the energy transitions result in a wavenumber shift (Raman shift) characteristic for each species (*Fig. 5.15b*). These wavenumber shifts are independent of the incident light waves, but the intensity of the scattered light is inversely proportional to the wavelength, namely $1/\lambda^4$ [99, 100]. Hence, ultra violet laser light is mainly employed to stimulate the molecules. If the anti-Stokes Raman bands cannot be determined, the temperature cannot be calculated and thus the species concentration remains unknown. Therefore, the intensity of the Rayleigh scattering signal is used to estimate the temperature and an estimation of the concentration can be given by evaluating the Stokes Raman intensities. From that the temperature is calculated again. This iterative process is repeated until temperatures and concentrations of Rayleigh and Raman scattering match [101].

5.6.2 System

The layout of the Raman spectroscopy setup is depicted in *Fig. 5.16*. The system employed a SpitLight 600 Nd:YAG laser (InnoLas GmbH, Germany) and frequency multipliers producing ultra violet laser light with a wavelength of 355 nm. Pulse duration was 7 ns and the maximum pulse energy at the wavelength employed was 200 mJ. A polarization rotator (LaVision GmbH, Germany) allowed adjusting the polarization of the laser light in order to set the intensity of the scattered light. In front of the polarization rotator a collecting lens with a focal length of $f_L = 500\,\mathrm{mm}$ was placed which ensured a focused laser light beam within and outside the flame zone. Perpendicular to the laser beam an imaging lens with a focal length of $f_L = 50\,\mathrm{mm}$ and two bandpass filters, reducing the Rayleigh signal at 355 nm, were positioned. The rectangular entry slit (slit width 0.35 mm) for the scattered light of the spectrograph (Acton SpectraPro 2300i, Princeton Instruments, USA) was aligned horizontally in order to collect the scattered light in radial direction. Data was obtained within the radial distance $|r| = 40\,\mathrm{mm}$ which made it necessary to move the burner by $\pm 25\,\mathrm{mm}$ from the default position as the spectrograph covered 30 mm. Connected to

the spectrograph was an intensified charged coupled device (CCD) camera NanoStar S-25 (LaVision GmbH, Germany). Data acquisition and post-processing was done with the software program DaVis 7.2.1.64 (LaVision GmbH, Germany), the laser was controlled by the software package SpitLight 1.4.5 (InnoLas GmbH, Germany). To improve the signal-to-noise ratio averaging of the recorded images had to be performed. At each operating point 300 images á 10 laser bursts were taken which were then averaged. In order to eliminate the influence of background noise and parasitic light this was done for maximum and minimum scattering intensity by rotating the polarization of the incident laser light waves. The resulting figure obtained by subtracting those two images is then processed in the succeeding steps of the Raman evaluation.

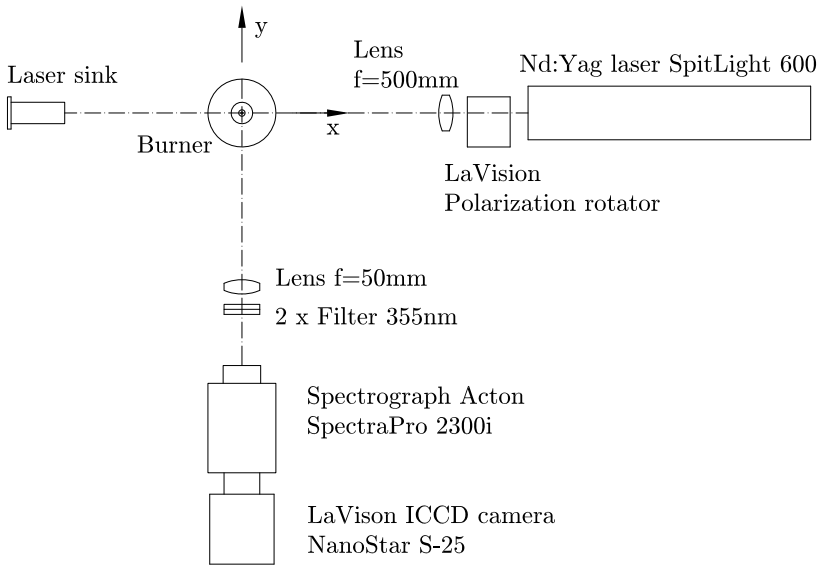

Fig. 5.16: Raman spectroscopy layout

Figure 5.17a shows a single image of a reference measurement for air at room temperature. *Figure 5.17b* and *Fig. 5.17c* depict averaged images at maximum and minimum scattering intensities, respectively. The resulting image for further processing is shown in *Fig. 5.17d*. The Raman spectrum of a methane/air flame and the spectrum of the according reference measurement of air with respect to the radius are shown in *Fig. 5.18*. Comparing the reference spectrum in *Fig. 5.18a* and the spectrum in *Fig. 5.18b* reveals the Stokes Raman band for methane. The band for oxygen has nearly vanished.

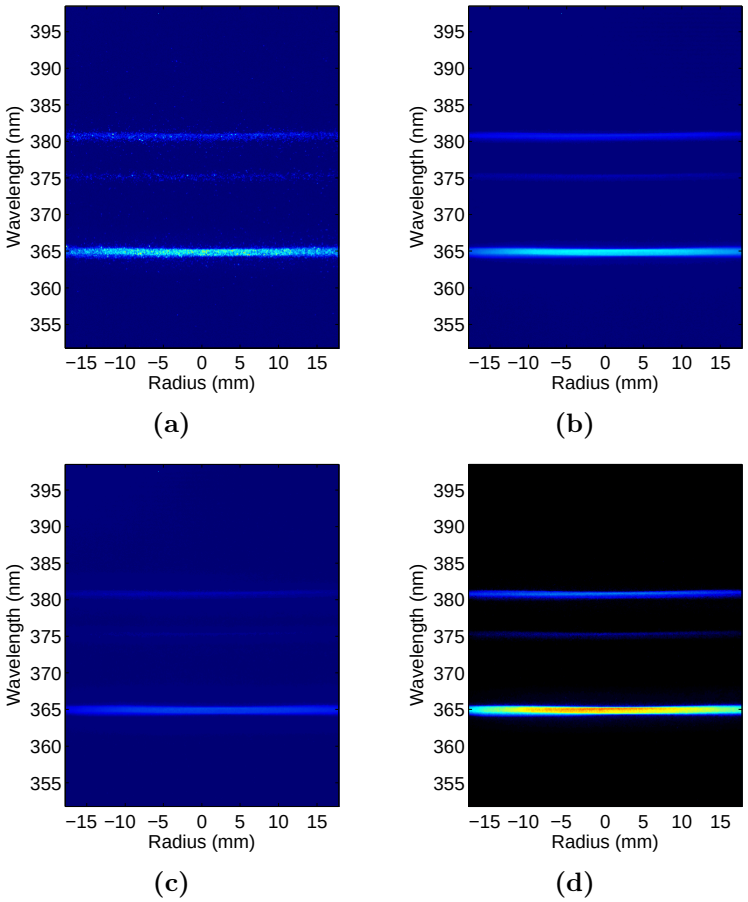

Fig. 5.17: Raman post-processing steps shown for reference measurements. Single Raman spectrum of air at ambient conditions (a), averaged image at maximum intensity obtained from 300 single frames (b), averaged image at minimum intensity (c), subtracted image for further processing (d)

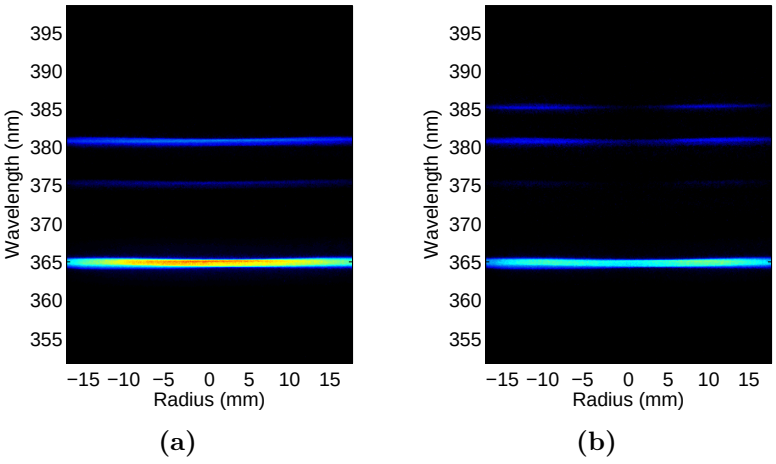

Fig. 5.18: Raman evaluation. Spectrum of reference measurement (a), spectrum of a methane/air flame (b)

After the calibration process through the post-processing procedure the temperature distribution can be calculated. For the reference measurements the distribution should be uniform, resulting in a horizontal line as can be seen in *Fig. 5.19a*. However, there is a difference between the calculated (280 K) and actual (300 K) temperature, which might be due to the iterative calculation process as the anti-Stokes Raman bands are not detectable. The calculated temperature distribution of a reference measurement of air as well as the distribution in the flame with a peak temperature of around 1200 K at the centerline are shown in *Fig. 5.19*.

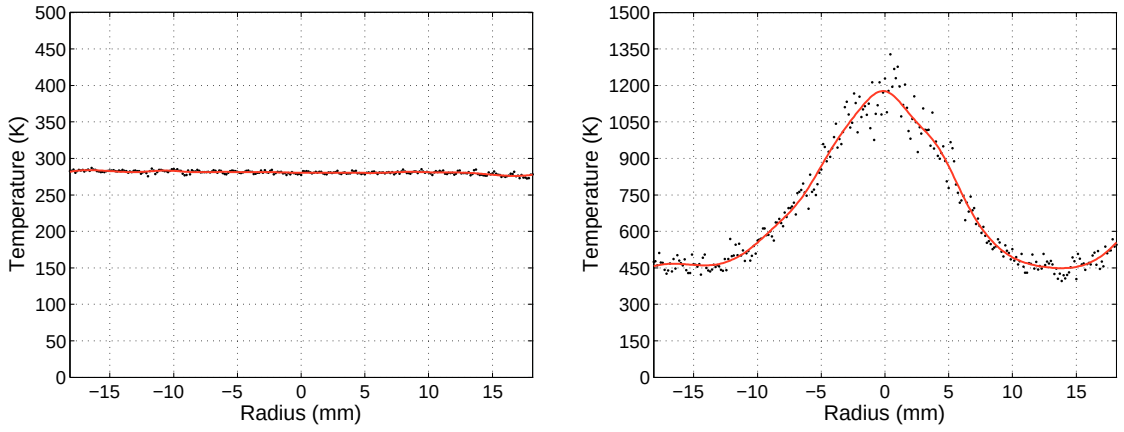

(a) **(b)**

Fig. 5.19: Temperature distribution. Reference temperature distribution (a), temperature distribution of a methane/air flame (b)

5.6.3 Uncertainties

The main source of noise is the image amplifier of the intensified CCD camera. Considering a SNR of the camera of 3, a turbulence level of the flame of 25 % and 300 images recorded, a measurement uncertainty of ±6 % can be estimated for a 95 % confidence interval. An additional source of noise could be an alternating laser intensity while flashing. In the LaVision system the energy output is monitored and the data corrected accordingly.

Chapter 6

Test rig

The test rig for the variable geometry burner basically consists of separate feed lines for axial and tangential air as well as for the fuel supply. Distribution boxes for all feeds ensured a uniformly splitting. Because of the modular structure of the rig, additional components, for instance a seeding generator, were easily to implement. The schematic layout of the test rig is illustrated in *Fig. 6.1*, the according descriptions are given in *Tab. 6.1*.

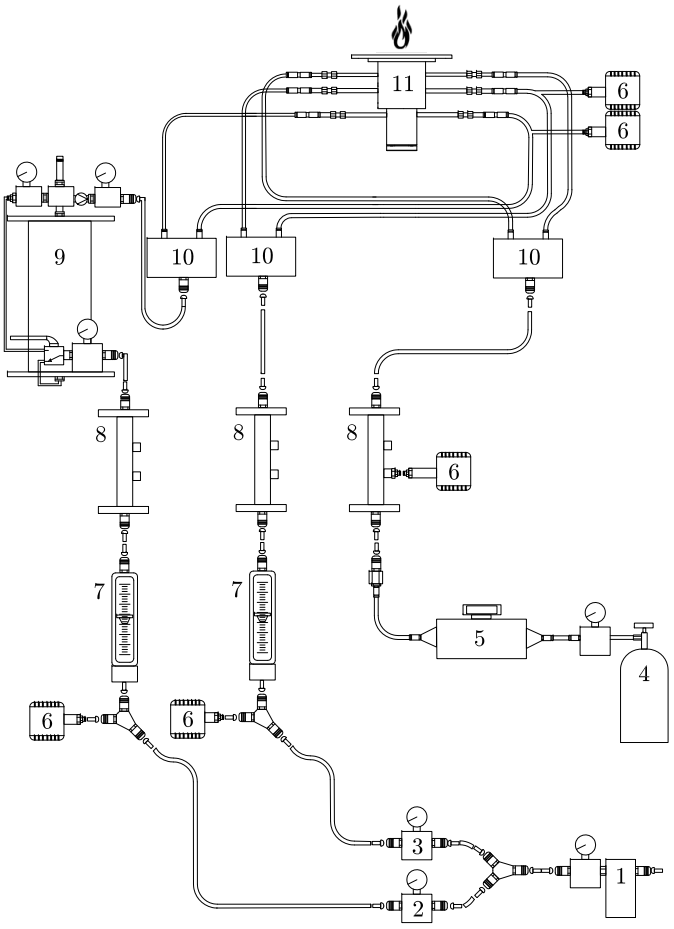

Fig. 6.1: Test rig layout

Tab. 6.1: Test rig description

Pos.	Description
1	Air supply
2	Control valve axial air
3	Control valve tangential air
4	Methane supply
5	Methane mass flow metering point
6	Pressure transducers
7	Air mass flow metering points
8	Temperature metering points
9	Seeding generator (only PIV measurements)
10	Distribution boxes
11	Variable geometry burner

The experiments with the burner were mainly performed in the laser lab of the institute except for the 3C PIV measurements, which were then performed outside the building. For the measurements in the lab the burner and all diagnostics were placed on a pneumatically damped support (1), as shown in *Fig. 6.2*, which shows the rig setup for confined PIV measurements. In order to enhance the movability, the burner was mounted on a rotation and linear moving unit (*Fig. 6.3*).

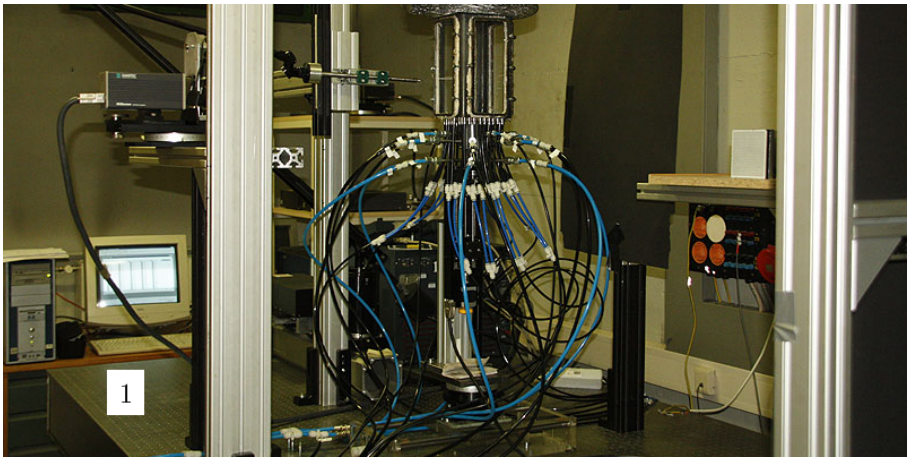

Fig. 6.2: Test rig setup for the experiments in the laser lab

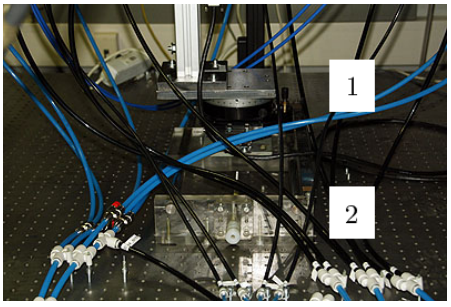

Fig. 6.3: Rotation (1) and linear moving unit (2) of the burner

As mentioned above, the 3C PIV experiments were performed outside the building due to safety reasons as titanium dioxide (TiO_2) was used as seeding material. For that purpose a movable containment ('PIV-o-mobil') was built in which the burner and the PIV diagnostics were placed. The test rig, the lasers and the control PC were placed next to it, as shown in *Fig. 6.4*. The containment ensured not only the safe disposal of the seeding material but also served as protection against the laser light sheet.

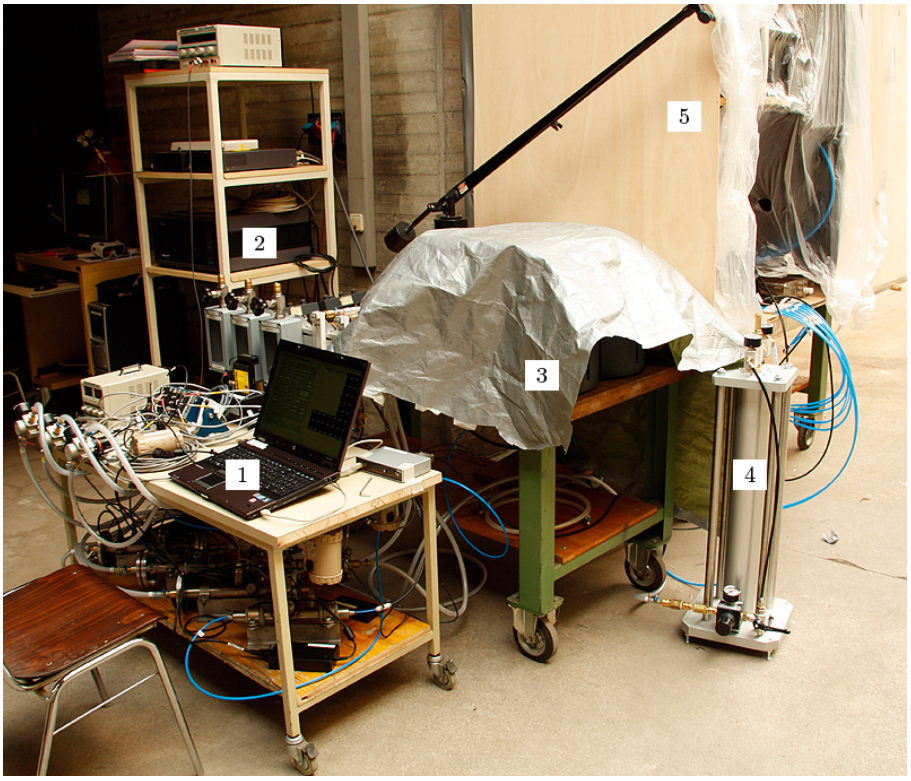

Fig. 6.4: 3C PIV setup. Descriptions are listed in *Tab. 6.2*

Tab. 6.2: 3C PIV setup description

Pos.	Description
1	Instrumentation, control and data acquisition trolley
2	PIV controllers
3	PIV lasers
4	Seeding generator
5	Containment

In both cases, experiments in the lab and outside the building, the burner was operated vertically due to reasons of operability.

6.1 Instrumentation of the test rig

The pressure measurements have been done with pressure transducers from Samsomatic (type 6051, Frankfurt am Main, Germany). Temperatures were measured with resistive thermal devices (RTD) of type P-MTF-A-6-300-0-T-5M (4-wire configuration). The fuel mass flow was measured with an Aalborg GFM77 mass flow meter (Orangeburg, New York, USA). The mass flows of axial and tangential air were measured with rotameters from InFlux (type LPL, Hampshire, United Kingdom). The mass flow rates of main air and fuel have been set by manually actuated valves. Data acquisition was performed with a National Instruments CompactDAQ chassis cDAQ-9178 in combination with the analog input modules NI 9203 and NI 9217 (Austin, Texas, USA). The data acquisition software was programmed in National Instruments LabVIEW 8.6. The axial position of the bluff body of the burner, for varying the exit nozzle area, was altered by a linear moving system from OWIS (Staufen, Germany) and controlled by the proprietary software program OWIS Motion Control v2.60. As control PC an EliteBook 8740w (Hewlett-Packard, Palo Alto, California, USA) was used. The operating system was Windows 7 32 bit (Microsoft, Redmond, Washington, USA). More details about the instrumentation and data acquisition as well as about the software routines can be found in [96].

The measurement uncertainties of the pressure transducers are less than 0.2% of the characteristic curves. The uncertainties of the fuel mass flow meter and the temperature measurements are ±1% FS and ±0.5 K, respectively. The air mass flow meters meet the requirements for the VDI/VDE 2.5 class. The uncertainty of the input module NI 9203 is given with ±0.5% of the characteristic curve.

6.2 Important parameters

6.2.1 Reduced mass flow rate

In order to eliminate the influence of weather conditions (pressure, temperature) during the experiments as they were performed on different days, a similarity parameter was needed to obtain a certain general validity. Therefore, the reduced mass flow rate $\dot{m}_{red}$ was introduced which is derived from the so-called Mach number similarity.

Starting from the definition of the Mach number M which is the ratio of the local velocity w and the speed of sound c, Mach number similarity is obtained by substituting the speed of sound by $\sqrt{\gamma\, R\, T}$ where T denotes as the temperature and assuming the specific heat ratio γ and the gas constant R being constant (*Eq. (6.1)*).

$$M = \frac{w}{c} = \frac{w}{\sqrt{\gamma\, R\, T}} \propto \underbrace{\frac{w}{\sqrt{T}}}_{\text{Mach number similarity}} \tag{6.1}$$

Considering the equation of continuity and the ideal gas law the mass flow rate can be written as:

$$\dot{m} = A\, w\, \frac{p}{R\, T} = A\, w\, \frac{p}{R\, \sqrt{T}\, \sqrt{T}} \tag{6.2}$$

where A and p denote as reference area and pressure, respectively. Rearranging *Eq. (6.2)* results in:

$$\dot{m}\frac{\sqrt{T}}{p} = \frac{A}{R}\frac{w}{\sqrt{T}} \propto \frac{w}{\sqrt{T}} \tag{6.3}$$

The term on the left in *Eq. (6.3)* denotes as the reduced mass flow rate where temperature T has to be used in Kelvin and pressure p in bar.

$$\dot{m}_{red} = \dot{m}\frac{\sqrt{T}}{p} \tag{6.4}$$

6.2.2 Equivalence ratio

The equivalence ratio ϕ is mainly used to describe the combustion in the primary zone of the combustor. It is the ratio of the stoichiometric air/fuel ratio AFR_{sto} and the actual air/fuel ratio AFR_{act}.

$$\phi = \frac{\mathrm{AFR}_{sto}}{\mathrm{AFR}_{act}} \tag{6.5}$$

Stoichiometric means that the quantities of reactants and products in a chemical reaction (e.g. combustion process) are balanced resulting in an equivalence ratio $\phi = 1$. Equivalence ratios greater than unity represent excess fuel and the term rich applies, equivalence ratios less than unity represent excess air and the mixtures are called lean. All experiments here have been performed at unconfined conditions. It is assumed that 50 % of the ambient air is participating in the combustion process.

The stoichiometric air/fuel ratio can be obtained by applying the reaction equation, as 23.1425 % by mass of oxygen in the air takes part in the combustion process, For instance, one mole of methane (CH_4) requires 2 moles of oxygen for complete combustion, as shown in *Eq. (6.6)*.

$$CH_4 + 2\,O_2 \longleftrightarrow CO_2 + 2\,H_2O \tag{6.6}$$

Substituting the atomic weights for carbon ($C = 12.011$), hydrogen ($H = 1.0079$) and oxygen ($O = 15.9994$), above equation can be written as:

$$16\,\mathrm{g} + 64\,\mathrm{g} \longleftrightarrow 44\,\mathrm{g} + 36\,\mathrm{g} \tag{6.7}$$

Hence, 1 g of methane requires 4 g of oxygen or 17.2 g of air. The stoichiometric air/fuel ratio for methane therefore is 17.2. In the same way the stoichiometric air/fuel ratio for kerosine (n-dodecane, $C_{12}H_{26}$ [102]) can be calculated, which is 15.

Chapter 7

Feasibility of variable geometry

Before the actual variable geometry burner was realized, a numerical analysis of a well known burner was performed. The question which was assessed, was to which extent combustion could be sustained with the help of variable geometry when operating conditions had changed. This analysis focused on the isothermal flow field at the injection. For the purpose of this study it was assumed that the information of the non-reactive flow field is sufficient. It was further assumed that combustion enhances the turbulence but the main flow field structure should remain unchanged [103]. The parameters which were altered were the strength of swirl, the area at the injector exit nozzle, and the mass flow rate.

7.1 Lang burner

The reference burner (*Fig. 7.1a*) for the pre-design simulation was a dump combustor with a swirl-stabilized flame, which was already experimentally investigated at Graz University of Technology [44, 104, 105]. The burner consists of a pressure casing for intermediate pressure (up to 5 bars) including a liner. Effusion cooling takes place around the flametube until both exhaust and cooling gases mix shortly before the exhaust nozzle. The nozzle is an air-cooled variable geometry Laval nozzle in order to set the pressure level inside the pressure casing. The burner facilitates an axial swirler (*Fig. 7.1b*) which has a conical shape to prevent flashback of the flame as a methane/air mixture is used as fuel. The maximal thermal power was 25 kW. The flow field was investigated by means of particle image velocimetry (PIV) at atmospheric unconfined conditions and under intermediate pressure at confined conditions. Optical access was provided through three rectangular windows. The main dimensions of the burner are 240 x 100 x 100 mm, which are length, width, and height, respectively. The experimental results are reported in [104, 105].

7.2 Numerical simulation

7.2.1 Settings

For all numerical investigations the software package Fluent (version 6.3.26) was used. Solver settings have been '2d axisymmetric swirl pressure based' applying the standard k-ϵ turbulence model. In a feasibility study it was found that 55 000 nodes were a good compromise between reproducing the physics and optimizing the computational costs. In total 20 cases have been investigated during the feasibility analysis, where the number of cells, the type of solver, and the turbulence model have been varied. As a result of this,

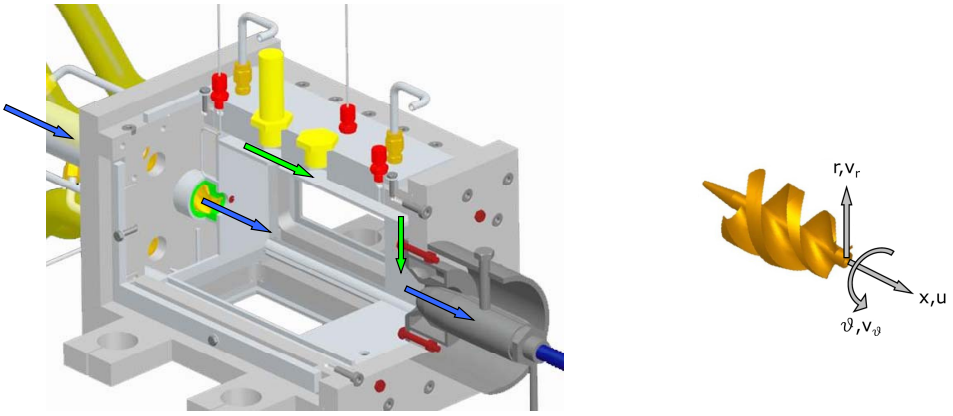

(a) **(b)**

Fig. 7.1: Sectional view of the Lang burner (a) and axial swirler (b) [104]. The direction of flow for both (a) and (b) is from left to right. Blue arrows are indicating the main air flow, green the cooling air flow (a). Gray arrows are indicating the coordinate system (b).

the main settings for the numerical simulation are summarized in *Tab. 7.1*. All meshes were created in Gambit (version 2.3.16) using text-based input files in order to vary the geometric parameters. The mesh used for the simulation of the baseline case is shown in *Fig. 7.2*. The swirling and cooling air inlets were defined as mass flow inlets whereas the exit was defined as pressure outlet. Swirl strength was adjusted by the velocity components. In *Tab. 7.2* the geometrical parameters varied in the numerical investigation can be found.

Tab. 7.1: Main settings for the numerical simulations

Description	Value
Number of nodes	55 000
Type of solver	2d axisymmetric swirl pressure based
Turbulence model	standard k-ϵ

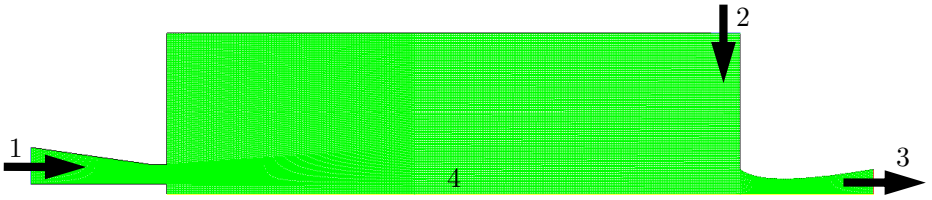

Fig. 7.2: Structured 2d mesh of the Lang burner. (1) Swirling air inlet, (2) cooling air inlet, (3) exit, (4) symmetry axis. Flow direction is from left to right. The maximum axial dimension is 285 mm, the maximum radial dimension 48 mm.

Tab. 7.2: Parameters varied in the numerical simulations

Case	Description	Mass flow	Swirl	Nozzle area	Subject
1	Baseline	fixed	fixed	fixed	Isothermal flow field
2	Small modulation	-7 %	fixed	fixed	Isothermal flow field
3	Critical modulation	-30 %	fixed	fixed	Isothermal flow field
4	Similarity	-30 %	varied	varied	Isothermal flow field

In all cases the swirl number S, as defined in *Sec. 3.1.1*, is calculated at $x/D = 1$, where x is the distance downstream of the head-plate of the burner and D being the burner exit nozzle diameter (*Fig. 7.3*).

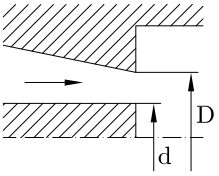

Fig. 7.3: Detail of the simulated burner exit nozzle

When working with compressible fluids, changing ambient conditions have to be considered for setting the operating point. This is done by introducing the reduced mass flow rate by employing the Mach number similarity. This relation calculates as $\sqrt{T}/p$, where T is the fluid temperature in Kelvin and p the pressure in bar at the nozzle inlet. For the deduction of this relation refer to *Sec. 6.2*. To obtain the same unit as the actual mass flow rate, the corrected mass flow rate is calculated by using reference values of temperature and pressure. These have been 288.15 K for T_0 and 1.013 bar for p_0.

$$\dot{m}_{corr} = \dot{m}\,\frac{\sqrt{T/T_0}}{p/p_0} \tag{7.1}$$

Reference velocity for all figures shown in *Sec. 7.3.1* is the mass averaged axial velocity at the burner exit nozzle at $x/D = 0$ of the reference case. It is calculated according to *Eq. (7.2)*, where $\dot{m}$ denotes as the mass flow rate, $\dot{m}_i$ and u_i as the mass flow rate and the axial velocity at the i^{th} cell, respectively, and N as the number of cells involved.

$$u_{ref} = \frac{1}{\dot{m}} \sum_{i=1}^{N} \dot{m}_i\, u_i \tag{7.2}$$

7.2.2 Operating conditions

The operating conditions for the different cases are listed in *Tab. 7.3*. Basis of the numbers given was the work of [6] as already mentioned in *Sec. 1.1*. Starting from the baseline, mass flow rate was successively decreased to -30 %. In the first three cases, geometry remained unchanged, in case four the geometry has been altered in order to establish a similar flow field compared to the baseline. Similarity was supposed to be achieved if the reference velocity and the swirl number at $x/D = 1$ were within a 5 % interval compared to the reference case.

Tab. 7.3: Operating conditions of the different cases

Description	Case 1	Case 2	Case 3 & 4
Main air mass flow rate (g/s)	6.50	6.045	4.55
Cooling air mass flow rate (g/s)	25.00	23.25	17.50
Burner nozzle inlet pressure (kPa)	219	245	282
Temperature (K)	300	300	300

7.3 Results

7.3.1 Fixed geometry

The simulation results of the different operating conditions listed above are shown in *Fig. 7.4*. Depicted are velocity profiles of radial velocity v_r, tangential velocity v_ϕ, and axial velocity u. It can be seen that by reducing the mass flow rate and simultaneously increasing the inlet pressure the velocity profiles flatten which means that the magnitudes of the velocities are reduced. As a result the inner recirculation zone (IRZ) changes its size. The swirl number calculated at $x/D = 1$ remains nearly unchanged and stays within the 5 % interval. In *Tab. 7.4* the input conditions of mass flow rate $\dot{m}$ and pressure $p_{tot\,in}$ as well as the results for the axial velocity u at $x/D = 0$ and the swirl number S at $x/D = 1$ are shown.

Tab. 7.4: Input conditions and results for parameter variation with fixed geometry

Case	D	d	$\dot{m}$	$p_{tot\,in}$	u	S
Case 1 (reference)	18 mm	6 mm	31.5 g/s	219 kPa	15.6 m/s	0.598
Case 2	18 mm	6 mm	-7 %	+12 %	-18 %	-0.6 %
Case 3	18 mm	6 mm	-30 %	+29 %	-46 %	-4.5 %

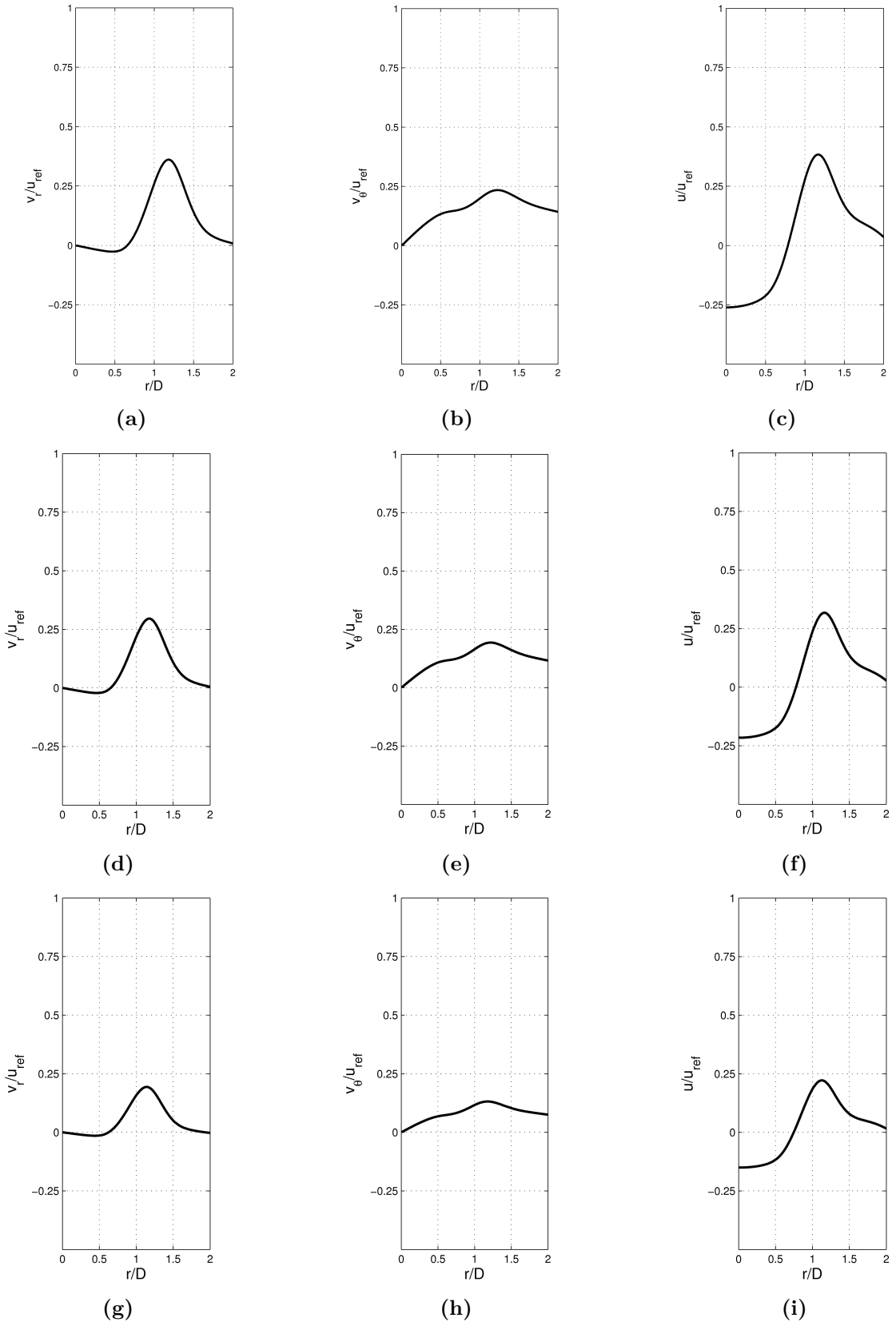

Fig. 7.4: Velocity profiles employing fixed geometry. Reference case: radial (a), tangential (b), axial (c). Small modulation of mass flow rate: radial (d), tangential (e), axial (f). Critical modulation of mass flow rate: radial (g), tangential (h), axial (i)

7.3.2 Variable geometry

In order to establish a similar flow field, when the mass flow rate was reduced by 30 % compared to that obtained at the reference case, the nozzle exit area and the inlet flow angle of the nozzle were varied. As the flow field of the case with small modulation of the mass flow rate (case 2) can be handled with a fixed geometry combustor, only the case with critical modulation (case 3) will be considered employing variable geometry (case 4). Quite a few possibilities exist though to change geometry, hence several cases have been investigated. Three cases, 4A - 4C, which show similarity with respect to the flow field are presented more in detail. At case 4A the outer diameter D was altered, at case 4B only the inner diameter d had been changed. Results when changing D and d simultaneously are shown in case 4C. In *Tab. 7.5* the geometry parameters as well as the results for the axial velocity u at $x/D = 0$ and the swirl number S at $x/D = 1$ are shown.

Tab. 7.5: Parameters and results employing variable geometry

Case	D	d	Swirl angle	u	S
Case 1 (reference)	18 mm	6 mm	73°	15.6 m/s	0.598
Case 4A	-30 %		+8 %	+1.3 %	-2.7 %
Case 4B		+139 %	+7 %	-1.0 %	-4.0 %
Case 4C	-8 %	+106 %	+7 %	-3.0 %	+0.3 %

Velocity profiles of radial velocity v_r, tangential velocity v_ϕ, and axial velocity u can be seen in *Fig. 7.5*. By reducing the exit nozzle area and adjusting the swirl angle accordingly, settings could be found, which allowed flow field similarity as defined before, although the velocity profiles differ slightly from that obtained at fixed geometry. In general, the magnitude of the three velocity components were raised. The highest increase of velocity was observed at the radial velocity profiles. The peaks of the profiles of radial and axial velocities were slightly shifted to greater values of r/D which corresponds to a wider inner recirculation zone.

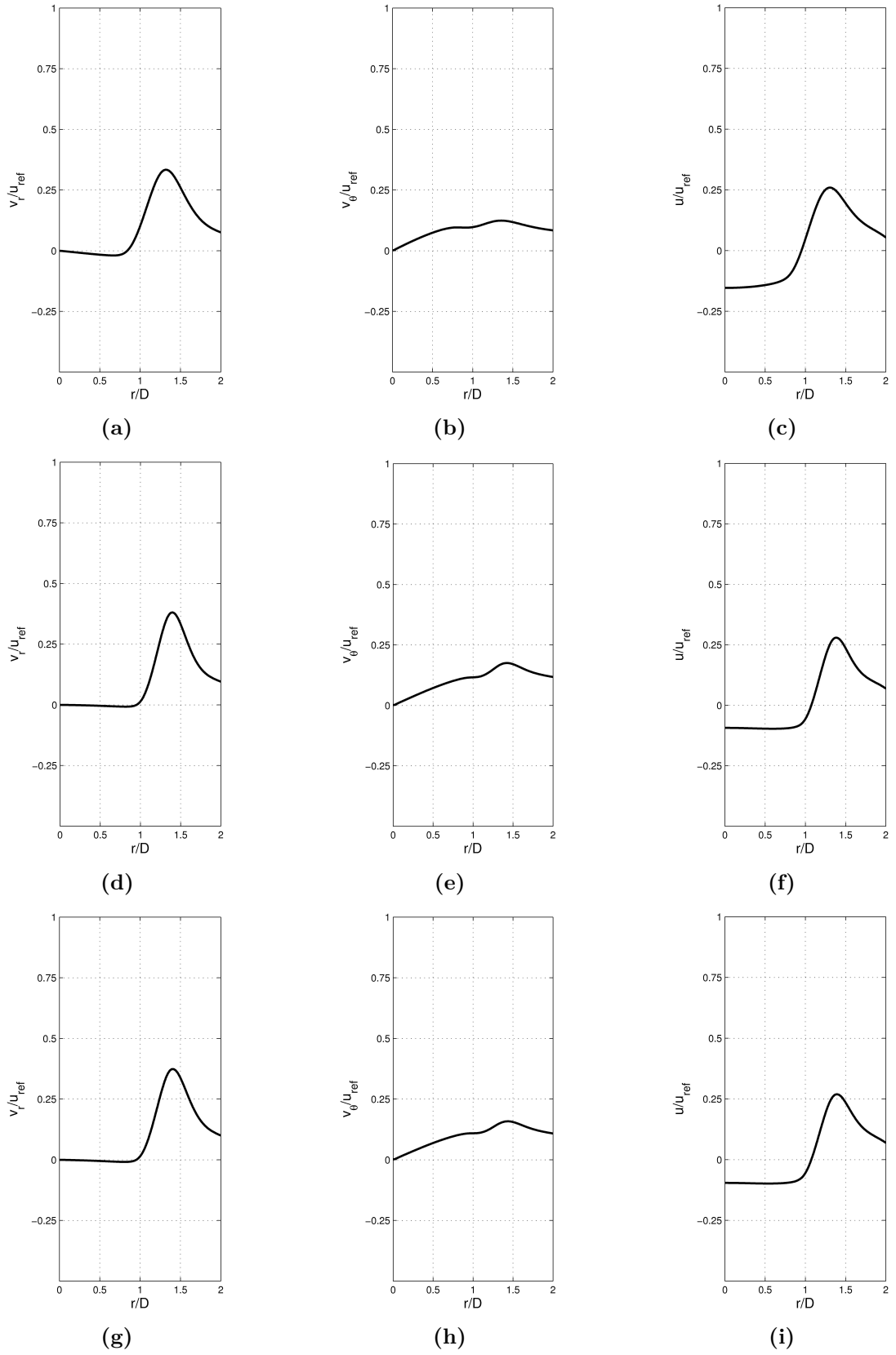

Fig. 7.5: Velocity profiles applying variable geometry. Changing the outer nozzle diameter D: radial (a), tangential (b), axial (c). Altering the inner nozzle diameter d: radial (d), tangential (e), axial (f). Changing both outer nozzle diameter D and inner nozzle diameter d: radial (g), tangential (h), axial (i)

7.4 Conclusion

It has been shown that reductions in mass flow rate alter the combustion aerodynamics. To a certain extend it can be adjusted by changing the burner exit nozzle area and setting a different swirl strength. The simulations performed showed promising results for an application of a variable geometry burner.

Chapter 8

Variable geometry burner

8.1 Burner Concept

After the literature research and the results found during the numerical simulation, it was found that the burner should employ a tangential swirl generator with an annular passage, as shown in *Fig. 3.3a* and *Fig. 8.1a*, where the mixing of axial and tangential air is performed. A movable center-body, concentrically mounted inside the annular passage, blocks the exit nozzle of the burner and varies the exit area. The novelty of this concept is, that both parameters can be set continuously and independently during operation. The swirl strength is set by the ratio of axial and tangential air mass flow by keeping the overall mass flow constant (*Fig. 8.1b*). For the experiments, the burner was rigidly coupled to a 1d actuation system and operated vertically. The assembly 'burner and actuation' was fixed on a mounting system, which was changed depending on the measurement technique (*Fig. 8.2a*). The coordinate system used throughout the evaluation is illustrated in *Fig. 8.2b* as well as the direction of the fluid rotation.

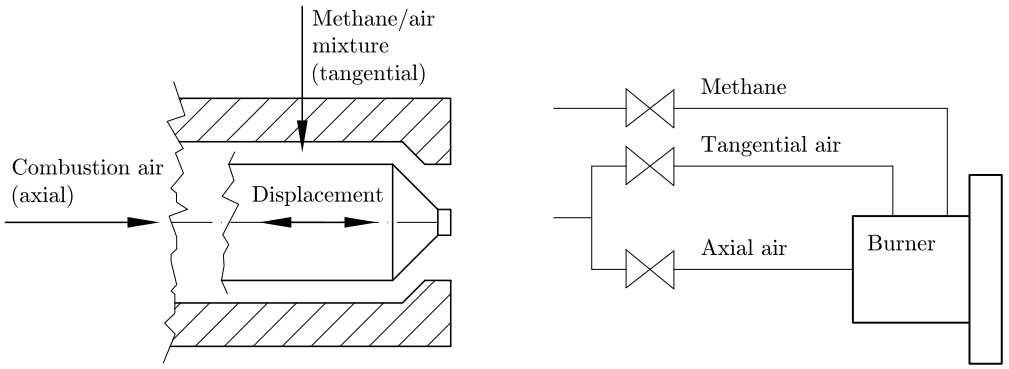

Fig. 8.1: Variable geometry burner. Principle of the variable geometry burner (a), separate feeds for axial and tangential air as well as for the fuel supply (b)

The variable geometry burner (*Fig. 8.3*) basically consists of three main parts. A movable center-body (1) which can be moved ±3 mm axially, an inner bushing (2), and an outer bushing (3). The outer bushing has six connectors for the tangential air (4) and four connectors for the fuel supply (5). The six connectors for the axial air (6) are mounted at the inner bushing which has also four tangential inlet slots (7) for introducing the swirl to the flow, shown in *Fig. 8.4*. The axial air has to pass a stratifier (8) before mixing between air and fuel is performed in the cavity (9) of the outer bushing. In order to adjust the momentum of the swirl flow into the cavity, the entries can be blocked with inserts (10).

The size of the inserts have been set to obtain equal momenta of axial and swirl flow at the mixing zone. The exit area of the quarl (11) is altered by the axial position of the center-body. The tip of the center-body and the quarl can be changed easily in order to investigate different nozzle geometries. The ratio of the inner diameter of the quarl and the outer diameter of the center-body controls both the mixture velocity and the bluff body effect of the center-body [19]. The design parameters are listed in *Tab. 8.1*. All detail and assembly drawings of the burner can be found on the attached DVD.

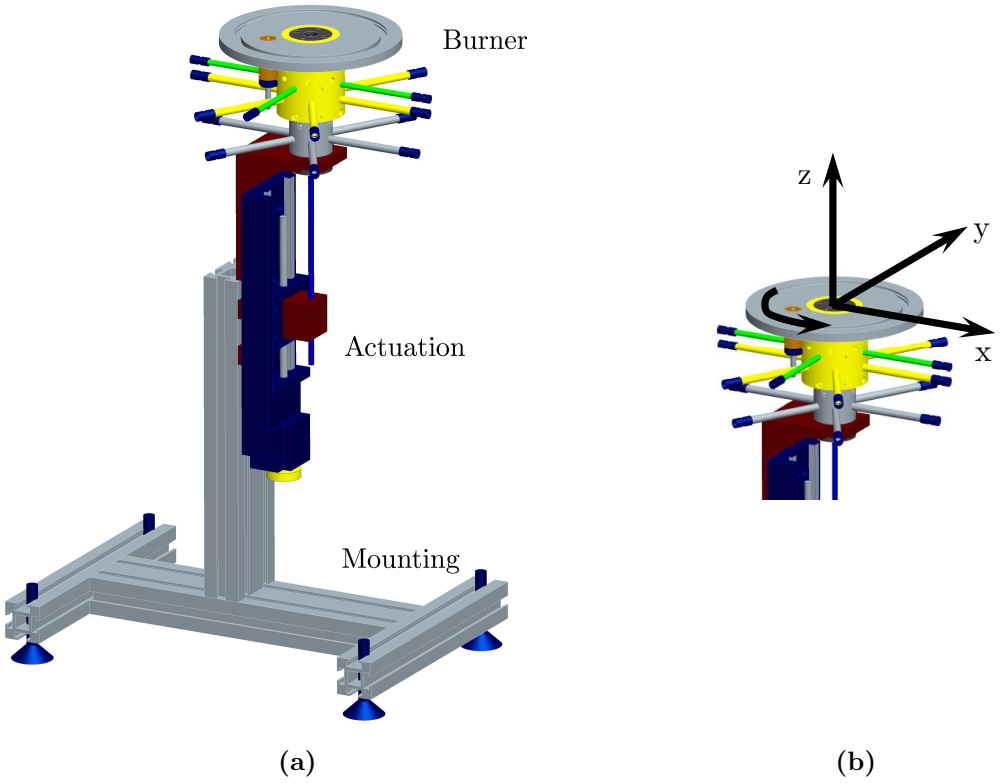

Fig. 8.2: Variable geometry burner. 3d model and mount (a), coordinate system and direction of fluid rotation (b)

Tab. 8.1: Design parameters of the variable geometry burner

Description	Value
Thermal power	up to 10 kW
Fuel	Methane
Equivalence ratio ϕ	0.3 – 1.2
Air mass flow	0.3 – 5 g/s
Pressure level	up to 5 bar
Nozzle diameter D	18 mm

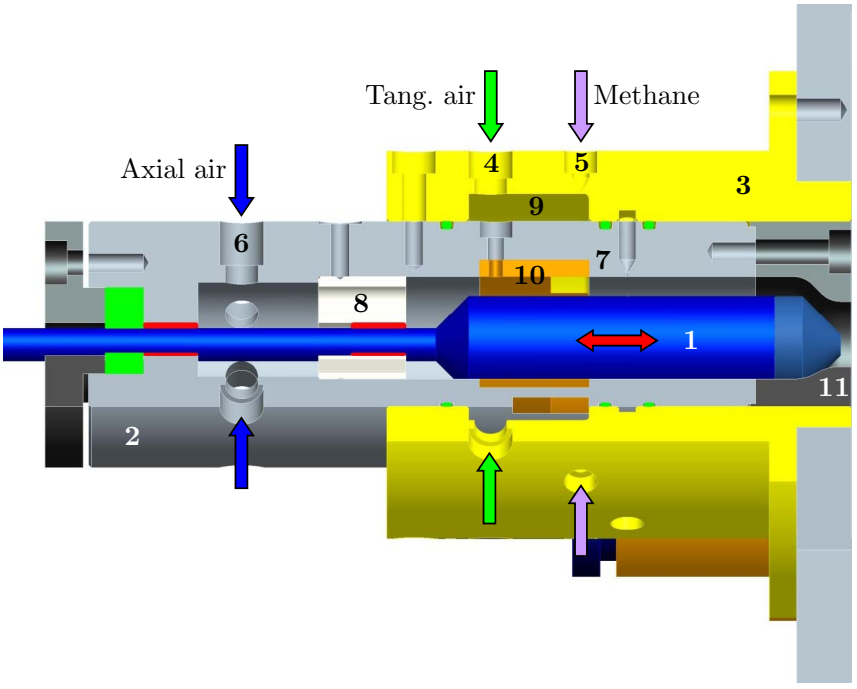

Fig. 8.3: Partial section of the variable geometry burner. Flow direction is from left to right.

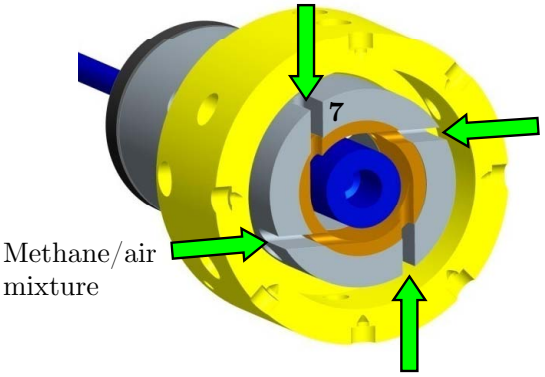

Fig. 8.4: Cross-section at the plane of the tangential injection of the methane/air mixture

8.2 Operating conditions

The extremal values of the operating conditions which have been used during this work are listed in *Tab. 8.2*, where $\dot{m}_{red}$ denotes the reduced air mass flow, $\dot{m}_{tan}/\dot{m}_{main}$ the ratio of tangential to main air, $\dot{m}_{CH_4}$ the fuel mass flow, and A the narrowest section in the burner exit nozzle. For the experiments four operating points have been investigated in particular; the default operating point denoted by DP or OP1a, OP1b with an increased swirl strength compared to the default operating point, and the operating points OP2a and OP2b with the mass flow rate reduced by approximately 50 % compared to OP1a. At OP2b the exit nozzle area has been reduced additionally. The operating conditions for the different points are listed in *Tab. 8.3*. The Reynolds numbers have been obtained by calculating the mean velocities in the narrowest cross-sections of the exit nozzle, as characteristic length the exit nozzle diameter D was used.

These points (OP1a – OP2b) have been selected for a deeper analysis in order to show the effectiveness of the actuation and as they may represent possible operating conditions within the operational envelope of an aircraft engine. Results will be compared between these points and might help to determine eligible control parameters for a later use of variable geometry in combustion processes.

Tab. 8.2: Extremal values of the operating conditions

Parameter	Range	Default operating point (default)
$\dot{m}_{red}$ (g/s (K$^{0.5}$/bar))	7 – 92	23.5
$\dot{m}_{tan}/\dot{m}_{main}$ (%)	0 – 60	43.5
$\dot{m}_{CH_4}$ (g/s)	0.02 – 0.1	0.08
A (mm^2)	29 – 80	$A_0 = 53$

Tab. 8.3: Operating conditions of the points investigated

Point	P kW	Mass flow rate g/s (K$^{0.5}$/bar)	ϕ –	Air split % ($\dot{m}_{tan}/\dot{m}_{main}$)	Area ratio % (A/A_0)	R_e –
OP1a, DP	4	23.5	0.7	43.5	100	24 800
OP1b	4	23.5	0.7	48.7	100	24 800
OP2a	2	12.3	0.7	45.7	100	12 100
OP2b	2	12.3	0.7	45.7	65	18 400

8.3 Variable geometry nozzle

As a solely swirl-stabilized flame might have been to unstable in terms of keeping a lifted flame during the measurements, a design was chosen which mitigated these circumstances. The center-body which not only blocked the exit nozzle area was used to support the flame stabilization [36, 37]. This was realized by the shape of the tip of the center-body which produced a wake right after the nozzle exit plane (*Fig. 8.5*).

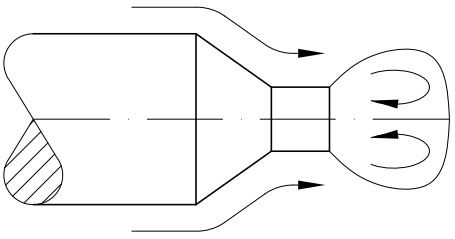

Fig. 8.5: Exit nozzle wake

As shown in *Chap. 7*, the shape of the injector nozzle has a major influence on the flow field. Therefore, numerous shapes of nozzles have been investigated numerically in order to obtain an optimal solution for the operating conditions applied. In *Fig. 8.6* a selection of nozzles are shown, which have been simulated in Fluent (version 6.3.26) at isothermal flow conditions. Details on the numerical simulations are given in *Sec. 8.3.1*.

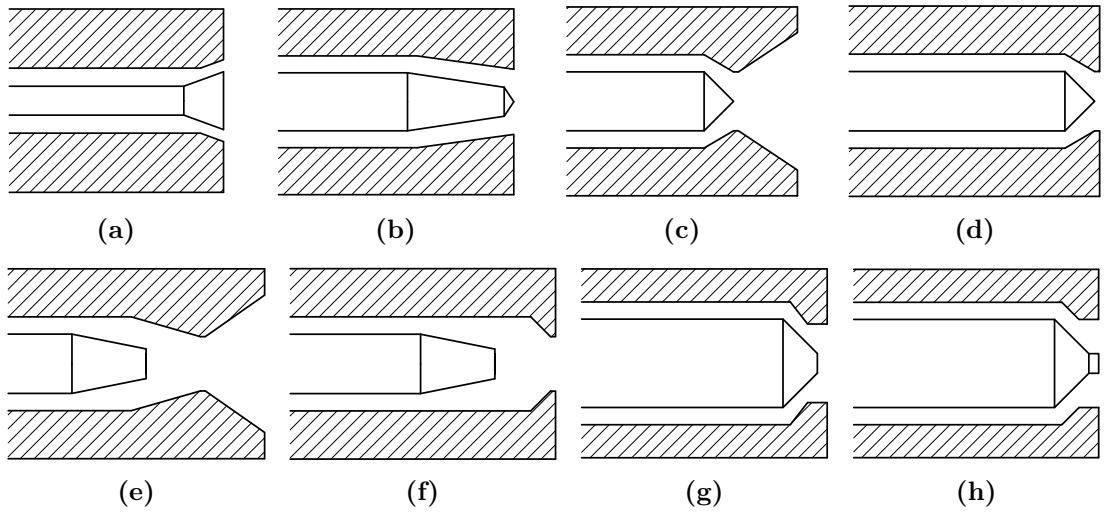

Fig. 8.6: Numerical investigated injector nozzles. Direction of flow is from left to right.

Following points have to be considered when designing a nozzle:

- The angles at the tip of the cone of the center-body should not be too small as the axial movement for a noticeable area change increases with acute angles. Furthermore, as the center-body anchors the flame, the movement has a strong influence on the flame position, as illustrated in *Fig. 8.7a*.
- When using a convergent nozzle (*Fig. 8.7b*), the velocity profiles are widened and flattened downstream of the injection zone. However, it is very likely that the flame attaches at the walls of the quarl.
- It was found during the numerical simulations of the different nozzle geometries, that the thickness of the bluff body has a strong influence on the shape of the recirculation zone and hence on the flame shape, which is indicated in *Fig. 8.7c*.
- At confined conditions, the ratio of flame-tube height and exit nozzle diameter influences the opening angle of the flame and the flame shape.

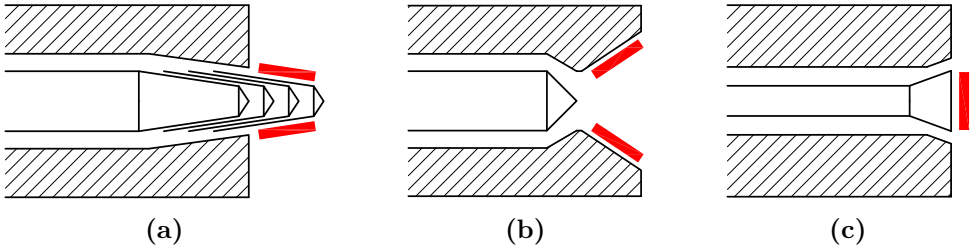

Fig. 8.7: Guidelines on nozzle design. Direction of flow is from left to right.

The area change of the burner exit nozzle (*Fig. 8.6h*) used for the variable geometry burner is shown in *Fig. 8.8* as a function of the axial position of the center-body. The default position is where the center-body's top face is adjacent to the exit nozzle plane. Limits for the movements have been ±2.5 mm (for the chosen nozzle type), resulting in area changes of -55 % and +64 %, respectively.

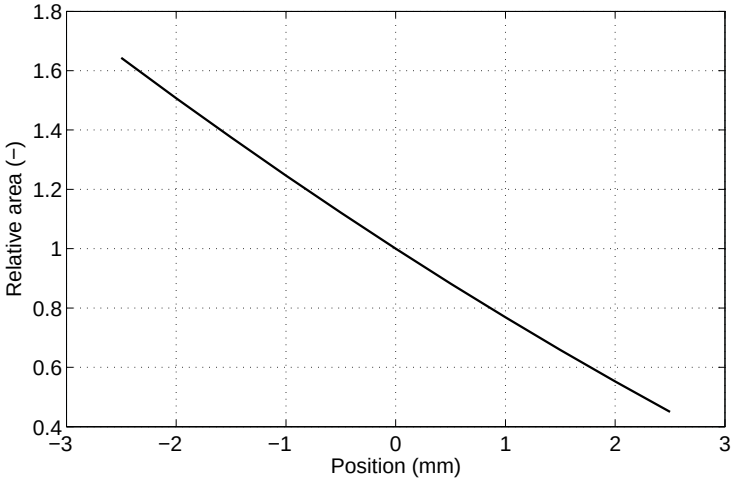

Fig. 8.8: Relative area of the burner exit nozzle depending on the position of the centerbody

8.3.1 Numerical simulation of the exit nozzles

The numerical simulations of the exit nozzles have been performed in order to gain information on the general flow field produced by the investigated nozzle types (*Fig. 8.6*) and on the effectiveness of the actuation system at several operating conditions. Based on the results, a nozzle geometry was chosen, which was then used for the variable geometry burner. As done in the feasibility study in *Chap. 7*, the parameters altered were the strength of swirl, the area at the injector exit plane (characterized by the axial position of the bluff body), and the mass flow rate. The range of the parameter variations are listed in *Tab. 8.4*. All calculations have been done at non-reactive conditions.

Tab. 8.4: Main parameter ranges of the numerical simulations

Parameter	Range
$\dot{m}$ (g/s)	3.5 – 10
$\dot{m}_{tan}/\dot{m}_{main}$ (%)	0 – 100
p (bar abs)	1 – 5
Nozzle geometry	Shown in *Fig. 8.6*
Axial position bluff body (mm)	±5 (depending on the nozzle type)

For all numerical investigations the software package Fluent (version 6.3.26) was used. Solver settings have been '2d axisymmetric swirl pressure based' applying the standard k-ϵ turbulence model. The meshes were created in Gambit (version 2.3.16) using text-based input files (*.jou) in order to vary the geometric parameters. The settings for the numerical simulations are summarized in *Tab. 8.5*. The mesh is shown in *Fig. 8.9*. The swirling air inlet was defined as mass flow inlet, the exit as pressure outlet. Swirl strength was set by adjusting the velocity components. In order to verify the numerical calculations a test case applying a well known geometry was investigated. Details about the validation simulations are given in *App. B*.

Tab. 8.5: Settings for the numerical simulations

Description	Value
Number of cells	20 000
Type	Tetrahedron
Type of solver	2d axisymmetric swirl pressure based
Turbulence model	standard k-ϵ

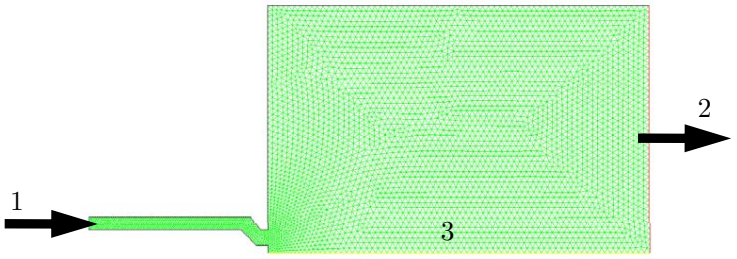

Fig. 8.9: 2d mesh of the nozzle design simulations for the nozzle type shown in *Fig. 8.6h*. Swirling air inlet (1), exit (2), symmetry axis (3). The maximum axial and radial dimensions are 147 mm and 65 mm, respectively. Arrows are indicating the flow direction.

8.3.2 Selection of the nozzle geometry

As mentioned above, calculations have been performed in order to obtain the optimal nozzle geometry for the variable geometry burner in terms of similarities in nozzle exit velocities and swirl numbers. Parameters have therefore been altered systematically according to *Tab. 8.4*. The chosen nozzle geometry is illustrated in *Fig. 8.10*.

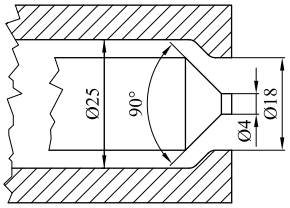

Fig. 8.10: Nozzle geometry selected

Following premisses for choosing the nozzle geometry by means of the numerical simulations should be met:

1. It was assumed that at a distance of $z/D = 1$ downstream of the head-plate the swirl number S should be around 0.6 for stable combustion [11].
2. The actuation should be kept at a minimum in order to remain the flame lifted if the operating conditions change.

For the chosen geometry, as illustrated in *Fig. 8.6h* and *Fig. 8.10*, profiles of radial, tangential and axial velocities of the numerical default operating point and a point with reduced

mass flow (-30 %) are shown in *Fig. 8.11*. In order to obtain an appropriate flow field again, the swirler angle and the exit nozzle area had to be changed. The resulting profiles flatten slightly at the changed operating conditions, but the structure compared to the default conditions remains the same. The reference velocities at the narrowest cross-section of the nozzle differ by 5 %. The swirl number remains nearly unchanged. The input parameters as well as the reference velocities and the swirl numbers at $x/D = 1$ of these two points are listed in *Tab. 8.6*.

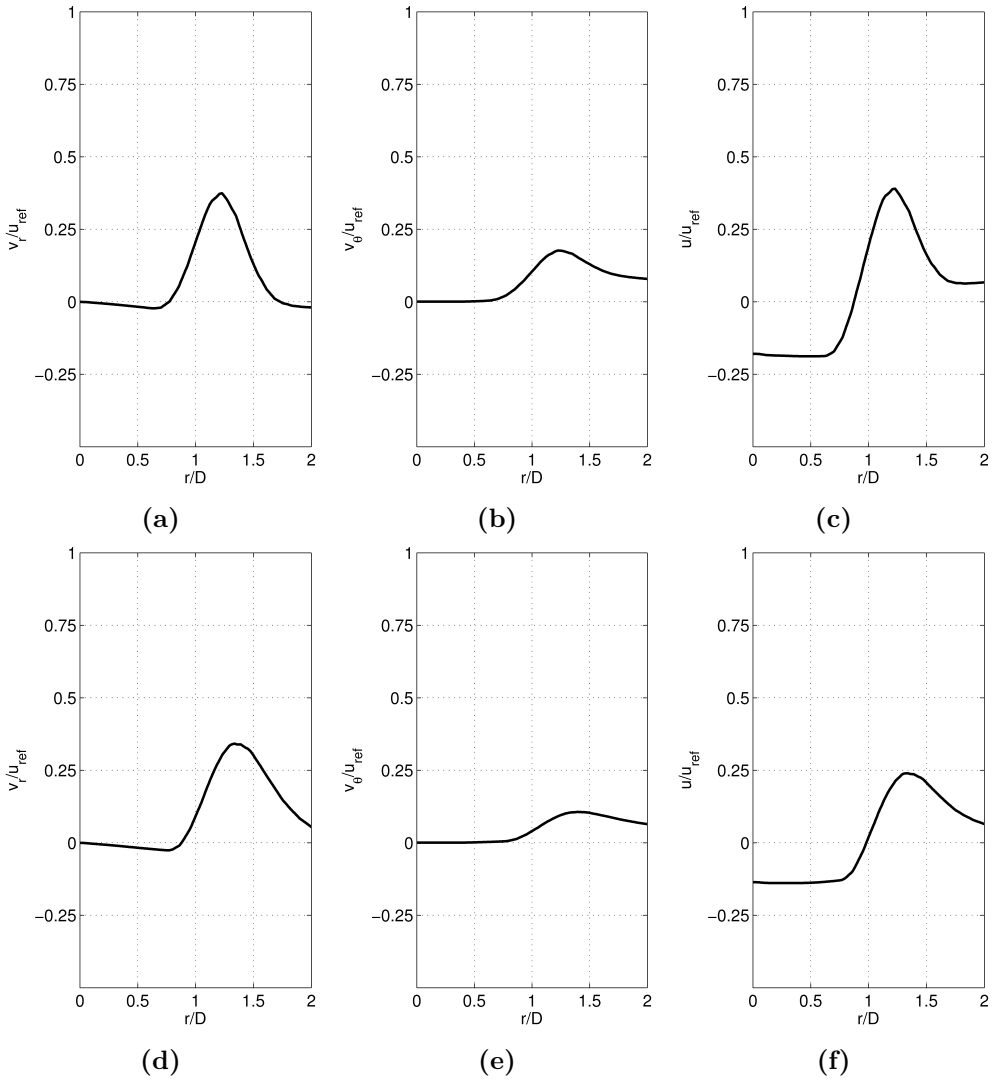

Fig. 8.11: Velocity profiles. Default operating point: radial (a), tangential (b), axial (c). Critical modulation of mass flow rate: radial (d), tangential (e), axial (f)

Tab. 8.6: Input values and results of the simulation of the chosen geometry

Point	$\dot{m}$ (g/s)	p_{in} (bar abs)	T (K)	Swirler angle (deg)	Axial displacement (mm)	u_{ref} (m/s)	S –
Default	5	1	300	63	0	40	0.564
Altered	3.5	1	300	67	2.5	38	0.567

Chapter 9

Experimental results

9.1 Pressure loss

Pressure loss measurements have been performed at isothermal and reactive conditions. The pressure loss of the burner is expressed as pressure rise, as all experiments have been performed at ambient conditions, which served as reference.

Figure 9.1 illustrates the pressure rise as a function of the reduced mass flow $\dot{m}_{red}$. It shows two separate curves, one for the axial and one for the tangential air supply. At around 75 g/s ($K^{0.5}$/bar) the maximum pressure rise is reached, which is nearly 250 mbar. It can also be observed, that starting from 22 g/s ($K^{0.5}$/bar) the pressure rise in the tangential line is slightly larger than in the axial.

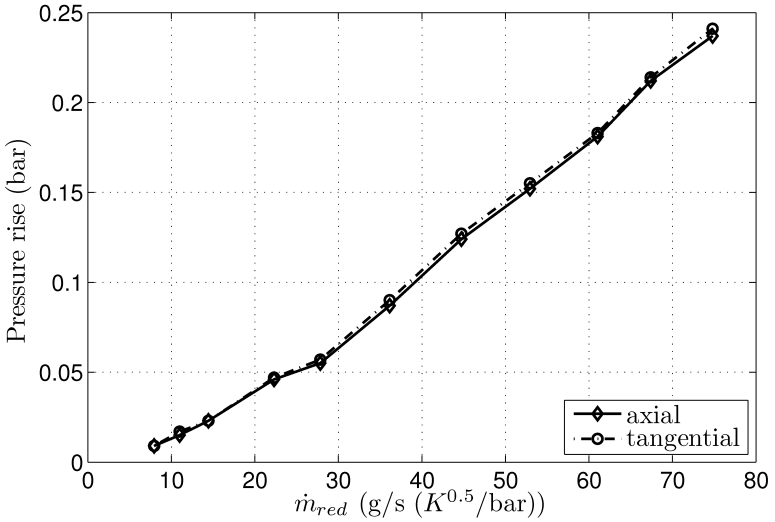

Fig. 9.1: Pressure rise at isothermal conditions including feed supply chain

However, the graph in *Fig. 9.1* includes the pressure losses of the whole feed lines and the burner module. To illustrate the pressure loss of the burner module, separate experiments have been carried out. *Figure 9.2* illustrates the pressure rise of the burner module with respect to the dynamic pressure p_{dyn}, as defined in *Eq. (9.1)*. Shown are three curves at different area ratios A/A_0, namely 1.48, 1 and 0.54. The resulting numbers have been normalized with the maximum values obtained at $A/A_0 = 1$. It can be seen that with increasing area ratio A/A_0 the slopes of the curves are becoming steeper. This may be

related to the fact, that the increase in mass flow rate is greater than that in pressure rise in that operating range.

$$p_{dyn} = \frac{1}{2}\,\rho\, w^2 \tag{9.1}$$

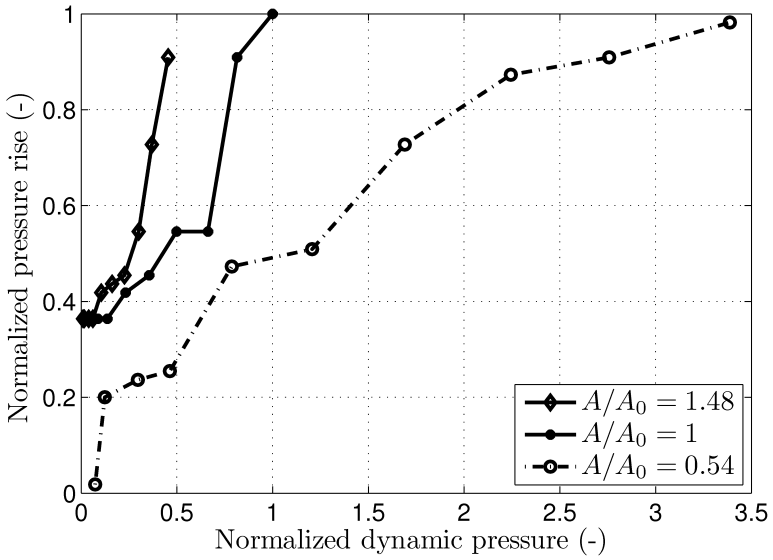

Fig. 9.2: Pressure rise due to area change

The previous figures have been obtained at isothermal conditions. *Figure 9.3* shows the pressure rise at three specific operating points under reactive conditions, namely OP1a, OP1b and OP2a. The curves include the feed lines as well as the burner module. At OP1a there is an obvious difference between axial and tangential feed lines, with the axial line producing the higher pressure rise. Increasing the swirl strength at OP1b, which means a higher tangential mass flow rate, entails a larger pressure rise of the tangential line. At OP2a the pressure rise drops to nearly a third compared to the other operating points due to the overall reduction of the mass flow rate.

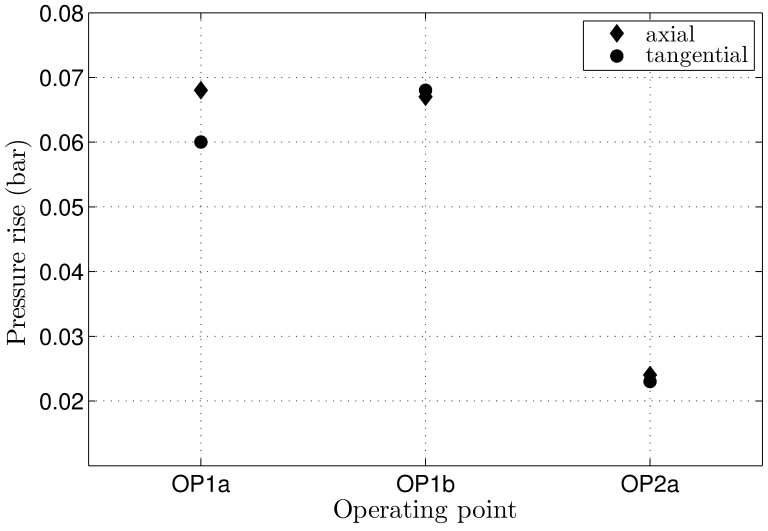

Fig. 9.3: Pressure rise including feed supply chain at OP1a, OP1b and OP2a

9.2 Spectral analysis

In order to identify certain frequencies, which may be excited during operation, a frequency analysis has been performed at the operating points OP1a, OP1b, OP2a and OP2b. This analysis used the voltage output signal of the laser vibrometer LV1998, as explained in *Sec. 5.4.3*. The measurement position was at $z = 25\,\text{mm}$ downstream of the head plate at the central burner axis, according to *Fig. 5.9*. Sampling frequency has been 16 384 Hz and measurement time was 30 sec resulting in 491 520 samples per measurement position. The discrete fast Fourier transform (FFT) has been performed in Matlab R2009b according to *Eq. (5.13)*. The figures shown have been averaged over 240 spectra with a frequency resolution of 8 Hz.

At OP1a (*Fig. 9.4a*) one distinctive peak is observed at 376 Hz. In contrast to OP1b (*Fig. 9.4b*), where two peaks are detected at 312 and 576 Hz. The magnitudes of the peaks are at the same level for OP1a and OP1b. The attached flame at OP2a produces a spectrum with a distinctive frequency band, ranging from 232 to 320 Hz (*Fig. 9.4c*). The magnitude of this band is approximately 40 % less compared to the one found at OP1a. At OP2b (*Fig. 9.4d*) one peak is detected at 176 Hz at an increased magnitude compared to OP2a, which is nearly 13 % less than the magnitude found at OP1a. In general, higher magnitudes are observed at the lifted flames (OP1a, OP1b and OP2b), which can be related to the higher turbulence levels. Furthermore, these results demonstrate vividly the problematic when it comes to combustion control, as depending on the operating point different frequencies are excited or amplified.

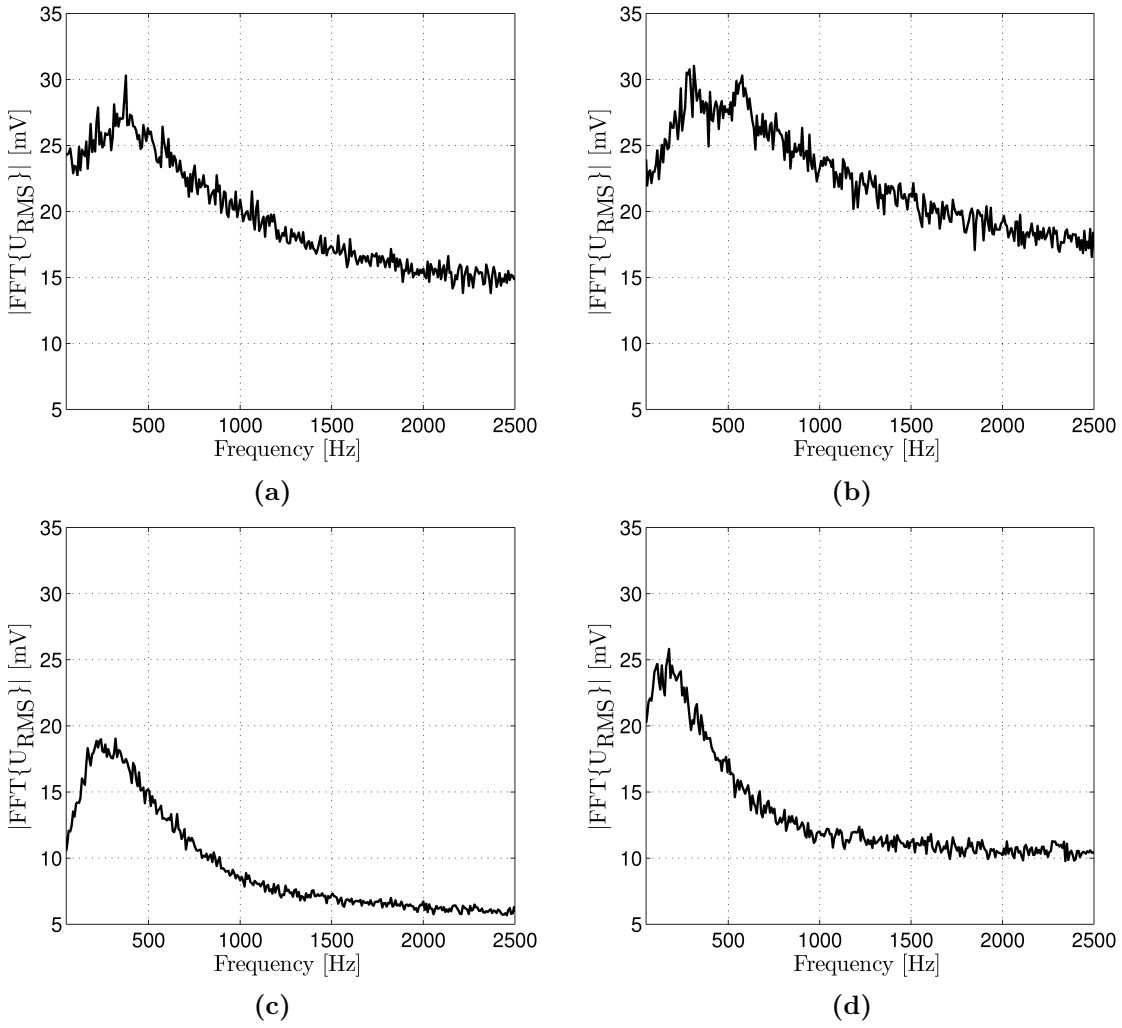

Fig. 9.4: Spectral analysis. OP1a (a), OP1b (b), OP2a (c), OP2b (d)

9.3 Flame shapes

With this burner different flames can be established depending on the settings of the overall air mass flow, the air split, the fuel mass flow, and the exit nozzle area ratio. At the default operating point the burner produces a swirl-stabilized lifted methane/air flame. Typically, these flames are characterized by turbulent combustion resulting in a complex and structured flame front [10]. However, for the experiments performed, specific points were defined in order to demonstrate the effectiveness of the actuation.

All operating points are explained in detail in *Sec. 8.2* and the according conditions are listed in *Tab. 8.3*. The experimental setup used for these measurements is explained in *Sec. 5.3.2*.

Instantaneous, averaged and fluctuating light emission images are illustrated in *Fig. 9.5*. Averaging has been performed over 250 images. The settings of the Panasonic NV-DX100E camera for exposure time, aperture and gain have been 1/50 sec, f/0.0 and 6 dB, respectively. Additionally, a band-pass filter centered at 380 nm has been applied. Contrast and brightness of all images shown, especially the fluctuating photographs, have been increased

for a better visualization quality. *Table 9.1*, which was deduced from the light emission, lists the dimensions and shapes of the operating points mentioned above, where L denotes the distance of the flame base from the head-plate, H the height of the flame, and W the width.

Tab. 9.1: Flame dimensions and shapes of specific operating points

	OP1a	OP1b	OP2a	OP2b
Distance L (mm)	22	11	–	29
Height H (mm)	31	34	157	31
Width W (mm)	46	52	46	38
Shape	heart-shaped	'M'-shaped	tubular	board-shaped
Base	lifted	lifted	attached	liftted

The default configuration, OP1a or DP, produces a lean premixed lifted flame, which stabilizes approximately 22 mm downstream of the head-plate. Instantaneous, mean and fluctuating images are shown in *Fig. 9.5a*, *Fig. 9.5e* and *Fig. 9.5i*, respectively. The strongest fluctuations of light emission of the heart-shaped flame appear on the upstream end (bottom side), as for all lifted flames produced by this burner.

Increasing the air split by 12 % according to *Tab. 8.3*, the burner stabilizes a flame which anchors at 11 mm above the head-plate. The shape of the flame changes from heartlike to 'M'-shaped compared to OP1a, as can be seen in *Fig. 9.5f*. Additionally, the flame slightly increases its width.

By reducing the air mass flow by 48 % the flame attaches at the outer rim of the exit nozzle. The flame shape changes from heartlike to tubular and significantly enlarges its height from 31 mm to 157 mm, compared to the operating point OP1a. The strongest fluctuations in light emission occur at 2/3 of the flame height, as can be seen in *Fig. 9.5k*.

Decreasing the exit nozzle area by 35 % compared to OP1a results in a detached flame. It stabilizes around 29 mm downstream of the head-plate and forms a slightly slanted board-shaped contour (*Fig. 9.5h*). The strongest fluctuations again emerge at the bottom of the flame.

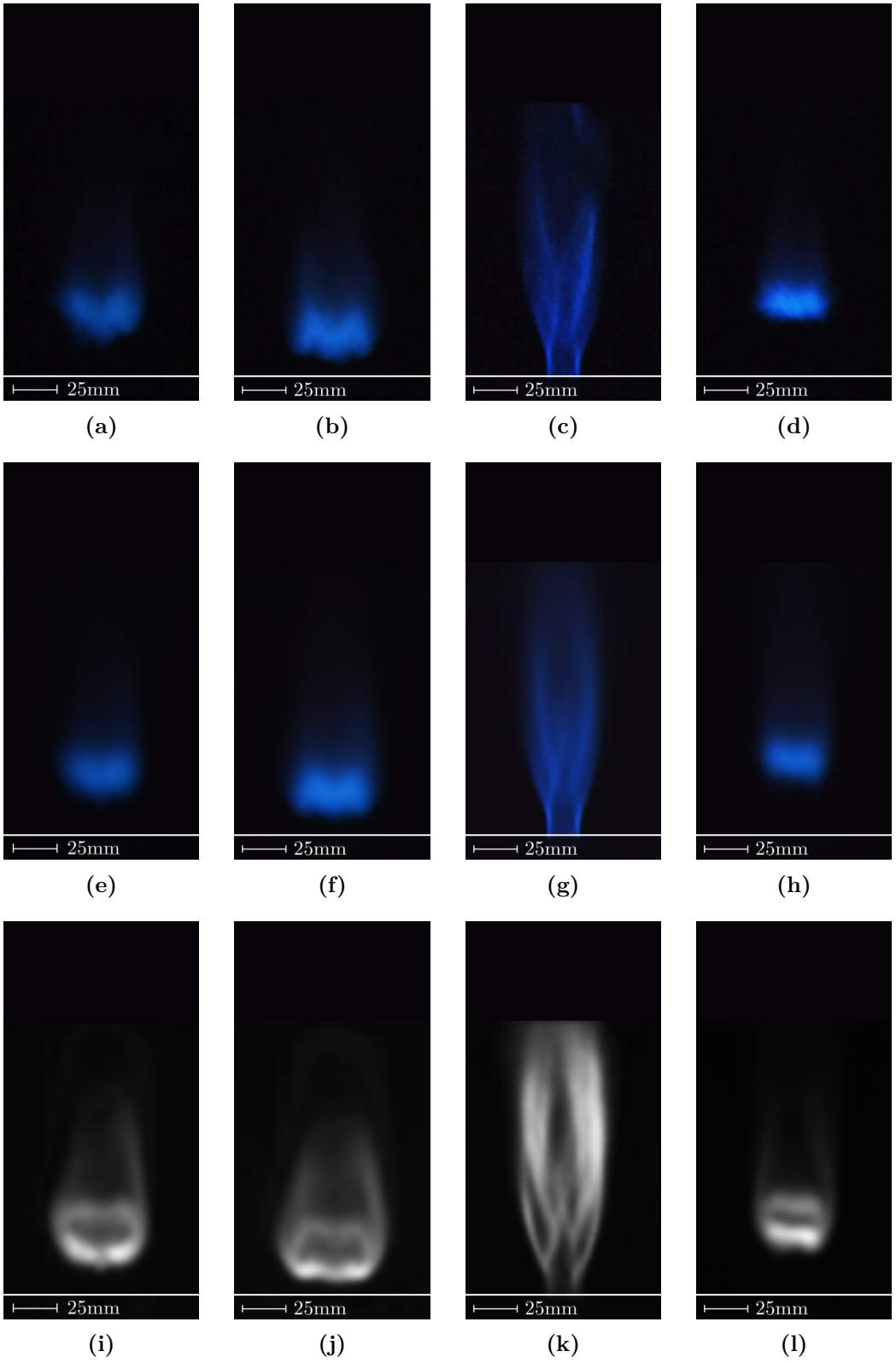

Fig. 9.5: Flame shape at different operating conditions. Instantaneous images: OP1a (a), OP1b (b), OP2a (c), OP2b (d). Averaged images: OP1a (e), OP1b (f), OP2a (g), OP2b (h). Fluctuating component images: OP1a (i), OP1b (j), OP2a (k), OP2b (l)

9.4 Reconstructed flame shapes

It is generally assumed, that under well premixed conditions, the flame shape can be given by the main reaction zone (see *Sec. 5.3.1*). However, as will be shown for instance in *Fig. 9.18*, the influence zone of the flame is significantly larger. As the flame images shown above are integral data, no satisfying statement can be given on the flame shape. Therefore, the flame was recorded from several directions and by means of a tomographic reconstruction technique, explained in *Sec. 5.3*, local data were obtained.

Figure 9.6 shows cross-sectional views of the light intensity at different operating points. Illustrated are two arbitrary iso-surfaces, which vividly visualize the flame shape. For the compact flames (*Fig. 9.6a*, *Fig. 9.6b* and *Fig. 9.6d*) these iso-values are five times larger than that of the attached flame, shown in *Fig. 9.6c*, as it forms a long tubular reaction zone with lower light intensity. The values concerning flame dimension and shapes listed in *Tab. 9.1*, which were extracted from integral data, correspond to the information obtained through tomographic reconstruction. As observed before, the flames are not exactly symmetrical. This is mainly influenced by the manufacturing process of the burner as small crates or different hose length of the air or fuel supply have an impact on the pressure loss coefficient.

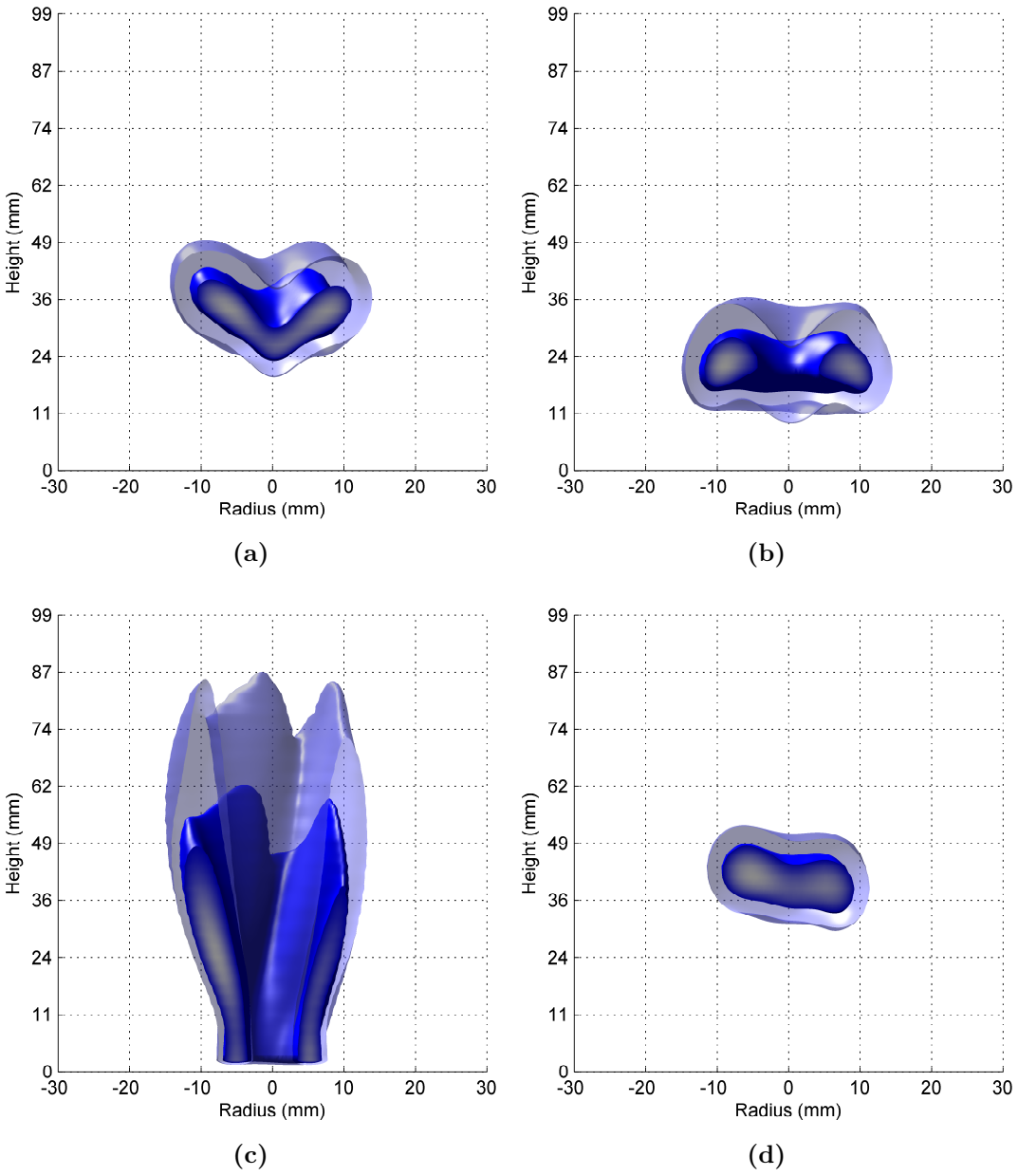

Fig. 9.6: Cross-sectional views of light intensities at different operating points. OP1a (a), OP1b (b), OP2a (c), OP2b (d)

In *Fig. 9.7* 3d views of the light emission at different operating points are presented. For the iso-surfaces illustrated the same values as in *Fig. 9.6* have been used. When considering the flame shapes, two points attract attention. Firstly, the slight asymmetry of the flames as mentioned above. Secondly, as the burner employs four tangential inlet slots for introducing the swirling air and the fuel, four prongs are observed. Depending on the operating point, the circumferential position of the prongs varies slightly. To obtain a more unified distribution, it might be advantageous to employ a greater number of tangential inlet slots, 8-10 slots should be sufficient.

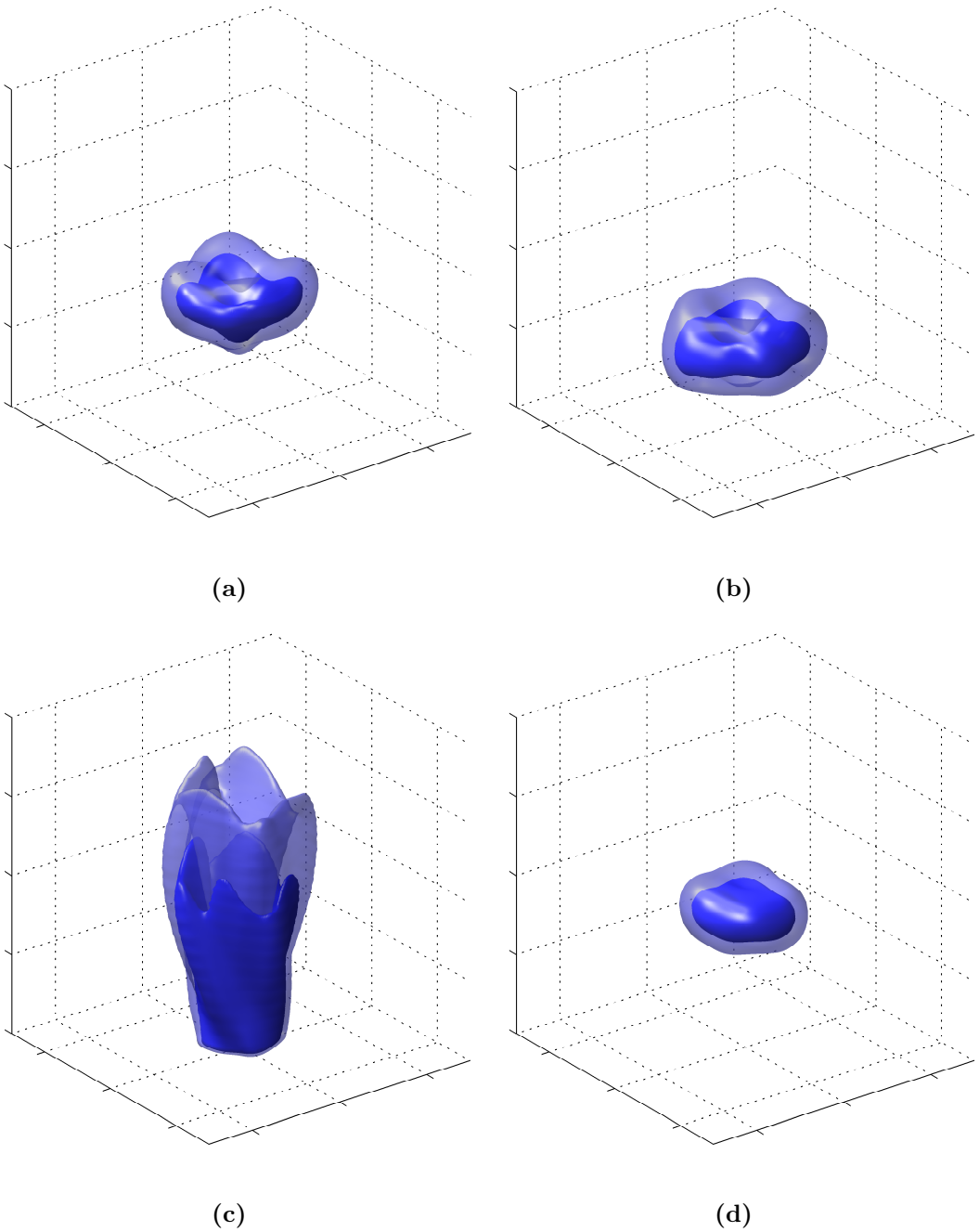

(a) **(b)**

(c) **(d)**

Fig. 9.7: 3d views of light intensities of different operating points. OP1a (a), OP1b (b), OP2a (c), OP2b (d)

9.5 Varying the fuel mass flow rate

Figure 9.8 shows snapshots of the flame when the fuel mass flow rate is altered at a constant air mass flow and an air split $\dot{m}_{tan}/\dot{m}_{main}$ of 46 %. The white horizontal line marks the plane of injection ($z = 0$ mm) in all four images. The settings of the Panasonic NV-DX100E camera for exposure time, aperture and gain have been 1/50 sec, f/0.0 and 6 dB, respectively. Additionally, a band-pass filter centered at 380 nm has been applied.

Starting from an equivalence ratio $\phi = 0.42$ the flame settles at the tip of the center-body and receives a conical shape, as shown in *Fig. 9.8a*. By increasing the fuel mass flow rate ($\phi = 0.75$), the flame detaches and settles approximately 10 mm downstream of the head-plate (*Fig. 9.8b*). At an equivalence ratio of $\phi = 1$ the flame is attached again. In contrast to the lean conditions, the flame settles at the rim of the nozzle and forms a long, tubular reaction zone (*Fig. 9.8c*), which becomes even larger when the fuel mass flow is increased further ($\phi = 1.87$), shown in *Fig. 9.8d*. This flame already produces soot at the tip of the flame, which is indicated by the pink area due to the band-pass filter applied. Brightness and contrast of the images shown in *Fig. 9.8* have been set independently due to illustration reasons, as the brightness of each flame varies with the fuel mass flow rate. Hence, hardly any statement concerning heat release may be drawn from this images. However, they nicely show the transition of the flame from the lean to the rich regime.

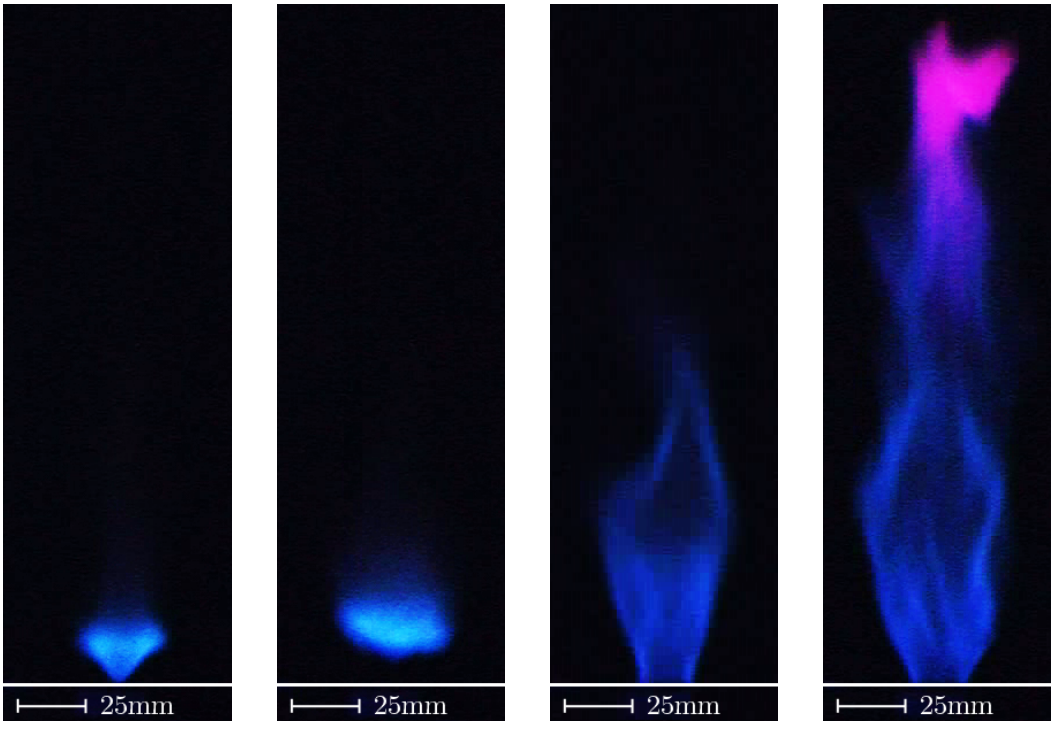

Fig. 9.8: Snapshots of the flame when varying the fuel mass flow rate and keeping the air mass flow constant. Equivalence ratio $\phi = 0.42$ (a), $\phi = 0.75$ (b), $\phi = 1.00$ (c), $\phi = 1.87$ (d)

9.6 Effect of axial and tangential air

Figure 9.9 illustrates flame shapes which are produced when using either the axial or the tangential air supply at a constant fuel mass flow rate. Basis for the images shown is the default operating point as described in *Tab. 8.3*. The camera settings were the same as those used for *Fig. 9.8* including the band-pass filter centered at 380 nm. As the brightness and contrast of each image was set independently for a better visualization quality, no conclusions concerning heat release rate may be drawn. The fluctuating images are held in grayscale due to visualization reasons.

The upper row of *Fig. 9.9* shows instantaneous, the middle row averaged, and the bottom row fluctuating component images of three different configurations. The left column is related to a diffusion flame, as only the fuel supply was activated. The feed lines for axial and tangential air had not been used. The center column belongs to an axial flame, as only the axial air supply was used. The right column on the other hand is related to a tangential flame, as only the tangential air supply was activated.

Figure 9.9a shows a snapshot of the diffusion flame which incorporates strong flame front oscillations. Due to the heavy soot production, the flame appears pink which is a result of the band-pass filter applied. By averaging approximately 350 snapshots, *Fig. 9.9d* was created. A tube of around 30 mm in diameter can be identified along the flame height which remains in all single snapshots. The fluctuating contributions are depicted in *Fig. 9.9g*. The amplitudes of the fluctuations are of the order of the mean value and are situated at the border of the flame.

In contrast to the diffusion flame, the configuration with additional axial air (equivalence ratio $\phi = 1.37$) produces a long axial jet flame which stabilizes on the outer ring of the burner exit nozzle (*Fig. 9.9b*). The instantaneous and the averaged image differ just at the top of the flame, this is hence the area where the brightest pixels can be found, as shown in *Fig. 9.9h*. At the bottom of the axial jet flame, bright areas (main reaction zones) can be identified, as the fuel is injected into the annual passage of the burner via four inlet slots. Due to the missing portion of tangential air, the momentum of the fuel injection is much weaker than that of the axial air. As a result, nearly no swirl is introduced to the flow and the main reaction zones appear undistorted.

When using only tangential air (equivalence ratio $\phi = 1.85$) a flame is stabilized which again anchors at the rim of the exit nozzle (*Fig. 9.9c*). This flame is significantly thicker and shorter than the axial flame as a result of the increased swirl strength. Due to the higher equivalence ratio ϕ soot production can be observed. The strongest fluctuations appear at the top of the flame, as illustrated in *Fig. 9.9i*.

Depending on the air supply and split the flame shape and behavior change drastically. By injecting only fuel a diffusion flame is produced, injecting only axial air a premixed jet flame can be observed. When using just tangential air a shorter but wider flame is produced compared to the premixed jet flame. The flame shape and the type of flame have an effect on the size of the reaction zone which in turn influences the thermal loading of the structure and the emission production. A concise overview of the emission formation mechanisms and on emission reduction technologies are given in *App. E* and *App. F*.

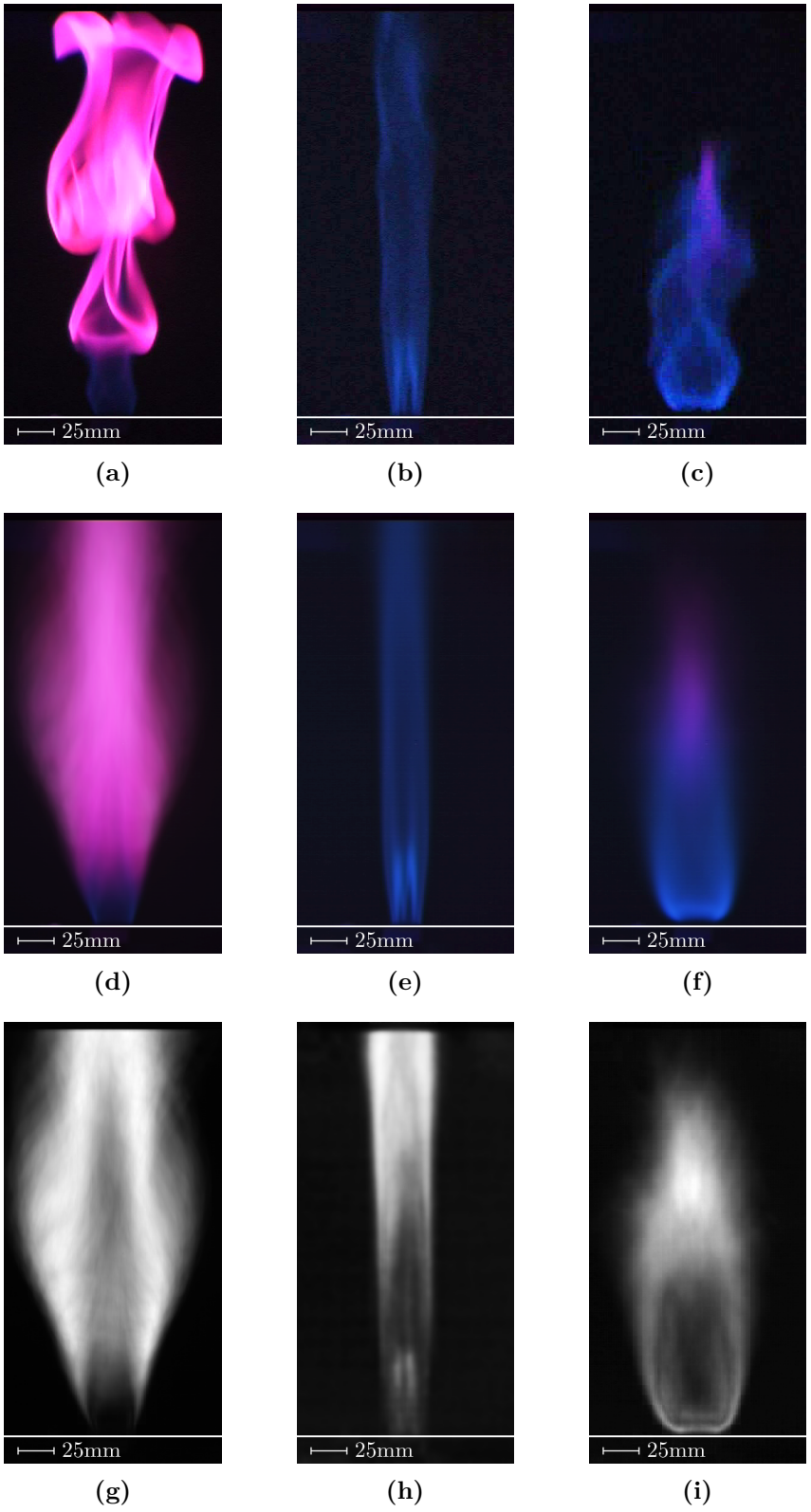

(a) **(b)** **(c)**

(d) **(e)** **(f)**

(g) **(h)** **(i)**

Fig. 9.9: Effect of axial and tangential air supply on the flame shape when keeping the fuel mass flow constant. Instantaneous images: diffusion flame (a), axial (b), tangential (c). Averaged images: diffusion flame (d), axial (e), tangential (f). Fluctuating component images: diffusion flame (g), axial (h), tangential (i)

9.7 Varying the exit nozzle area ratio

9.7.1 Default operating point

Figure 9.10 shows images (instantaneous, averaged, fluctuating) of the light emission of the flame at OP1a when varying the exit nozzle area ratio. Averaging has been applied over 300 images. The settings of the Panasonic NV-DX100E camera for exposure time, aperture and gain have been 1/50 sec, f/0.0 and 6 dB, respectively. A band-pass filter centered at 380 nm has been applied.

When increasing the exit nozzle area to 164 %, the flame anchors 18 mm downstream of the head-plate (*Tab. 9.2*). A difference of 4 mm is observed, as stated in *Tab. 9.1*. The width slightly increases although the height of the flame remains unchanged, as shown in *Fig. 9.10c*. The contour transforms from heartlike to 'M'-shaped.

Decreasing the area to 75 % results in a flame which stabilizes around 27 mm above the head-plate. The width of the flame decreases and the height remains unchanged (*Fig. 9.10d*). Due to the increased flow velocity, the opening angle of the flame cone becomes smaller, the flame shape remains heartlike though.

Tab. 9.2: Flame dimensions and shapes when varying the exit nozzle area ratio at OP1a

Area ratio (%)	164	75
Distance L (mm)	18	27
Height H (mm)	31	31
Width W (mm)	51	41
Shape	'M'-shaped	heart-shaped
Base	lifted	lifted

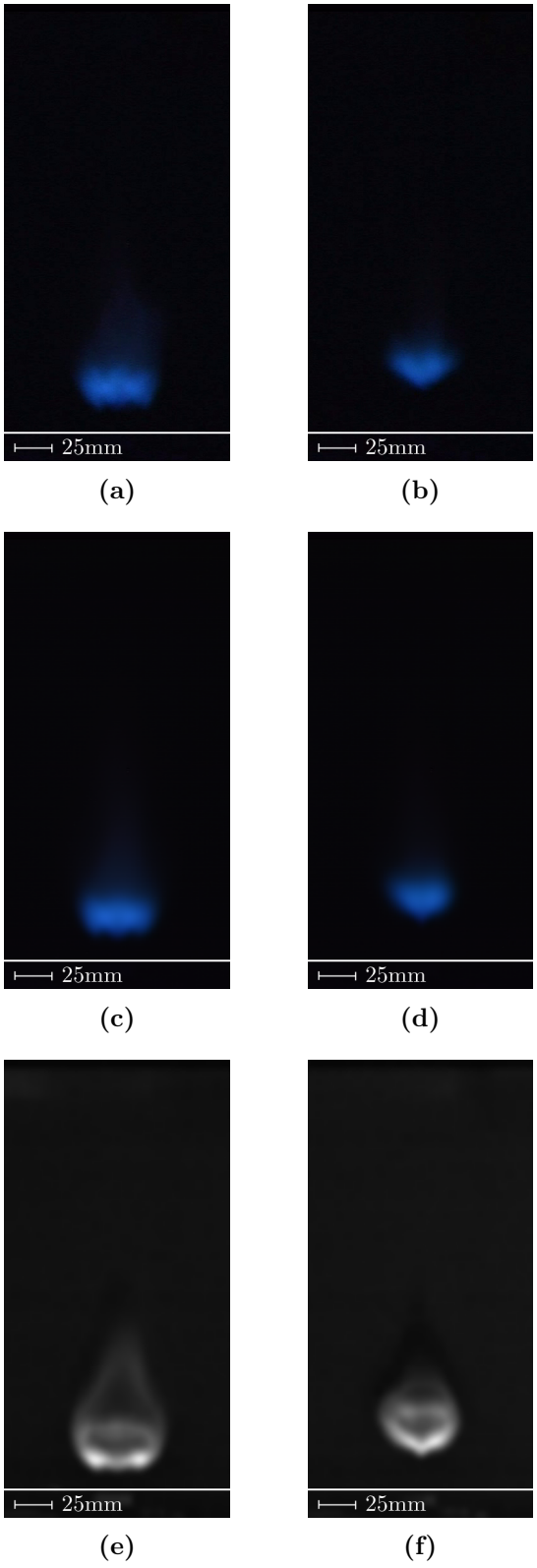

Fig. 9.10: Varying the exit nozzle area ratio at the default operating point. Instantaneous images: max. area (a), min. area (b). Averaged images: max. area (c), min. area (d). Fluctuating component images: max. area (e), min. area (f)

9.7.2 Off-design points

Figure 9.11 shows snapshots of the light emission of the flame when varying the nozzle exit area between the operating points OP2a and OP2b. Compared to the default operating point OP1a, the nozzle exit area ratio has been set to 65 % at OP2b in order to obtain a lifted flame. The settings of the Panasonic NV-DX100E camera for exposure time, aperture and gain have been 1/50 sec, f/0.0 and 6 dB, respectively. A band-pass filter centered at 380 nm has been applied. Contrast and brightness of all images shown have been increased for a better visualization quality.

Starting from the operating point OP2b (*Fig. 9.11a*), the nozzle exit area ratio is gradually increased to 100 % in order to reach OP2a. By enlarging the nozzle area, the axial flow velocity decreases and the flame starts moving upstream towards the burner head-plate. Furthermore, as the swirl strength increases, the flame widens. The leap from 'detached' to 'attached' starts at *Fig. 9.11q* and lasts until *Fig. 9.11s*, when the flame eventually completely anchors on the rim of the exit nozzle. A prong is formed on the flame bottom and establishes the contact to the head-plate. The rest of the flame follows and the contour changes from board-shaped to tubular. Compared to the process of bringing the flame towards the head-plate, the actual leap is a rather short event.

By decreasing the nozzle exit area, the tubular flame starts to get thinner over the whole flame height. Especially on the base, the flame tube constricts and finally the flame detaches. Again, a prong is observed (*Fig. 9.11v*), which vanishes as soon as the flame starts to stabilize in its new equilibrium state. The flame contour changes from tubular to board-shaped and the starting point, OP2b, is reached again.

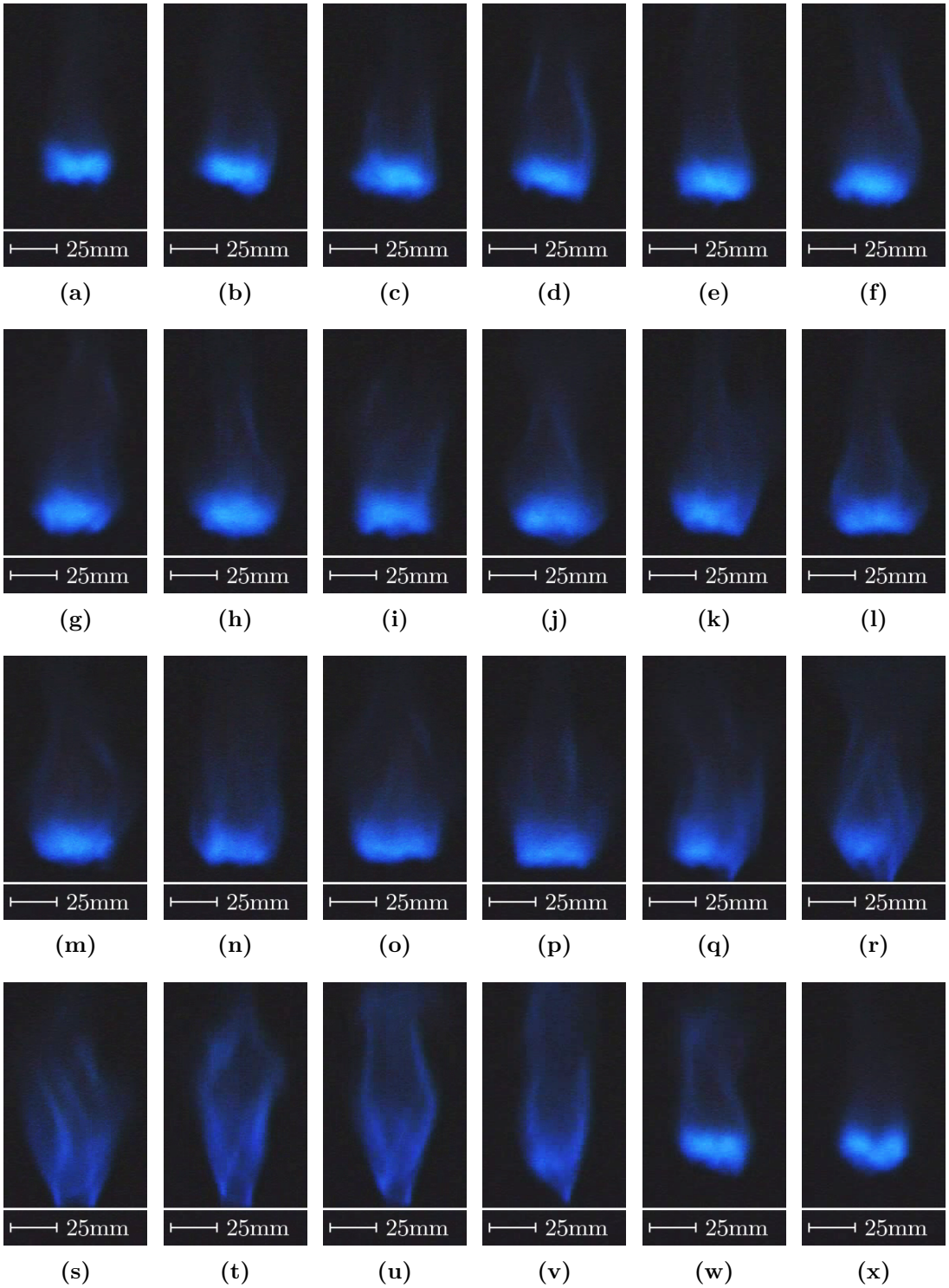

Fig. 9.11: Snapshots of the 'attach/detach'-sequence OP2b-OP2a-OP2b when varying the exit nozzle area ratio. Time step τ between the images is 4/100 sec. Contrast and brightness have been increased for better visualization.

9.8 Light emission analysis

In the previous sections images of the fluctuating portions of the different flames have been shown. However, for a better visualization quality, brightness and contrast have been increased independently. Hence, no conclusions can be drawn concerning the fluctuation level by comparing the illustrations but the spatial occurrence. *Figure 9.12* shows 2d plots of mean and RMS values of the whole light emission of the flame at the four operating points listed in *Tab. 8.3*. The values illustrated in *Fig. 9.12a* and *Fig. 9.12b* have been normalized with the according values at OP1a.

Figure 9.12a reveals that OP1b produces a slightly higher average light emission than OP1a, in contrast to OP2a and OP2b, which have lower values. One would assume this intuitively, as the fuel mass flow rate at the latter two points was reduced drastically. However, differences between according operating points can be observed. OP1a and OP1b differ by approximately 8 %, OP2a and OP2b by 14 %. The main influence on the intensity of the light emission can be traced back to fuel mass flow rate, however, there are other influence parameters like local equivalence ratio fluctuations, turbulence intensities and flame front properties, as already stated in *Sec. 5.3.1*, which may be responsible for the differences.

In *Fig. 9.12b* normalized RMS values are depicted. It can be observed that according operating points (OP1a/OP1b and OP2a/OP2b) have similar values. For OP2a and OP2b these values are approximately 15 % higher than those of OP1a. Although the flame shapes between OP2a (attached flame) and OP2b (lifted flame) differ drastically, the fluctuation level is nearly the same. However, the fluctuations at OP2a arise from the flame tip movements (*Fig. 9.5k*), the ones produced at OP2b from the movements of the flame base (*Fig. 9.5l*).

Figure 9.12c illustrates the ratio between the RMS and the mean values of the light emission. Again, for OP1a and OP1b these are lower than that of OP2a and OP2b. The fluctuations of OP1a and OP1b are of the order of 14 %, compared to the according mean value, of OP2a and OP2b they are 19 % and 22 %, respectively. It seems that increasing swirl reduces the fluctuation level slightly, however, reducing the exit nozzle area increases the fluctuations drastically.

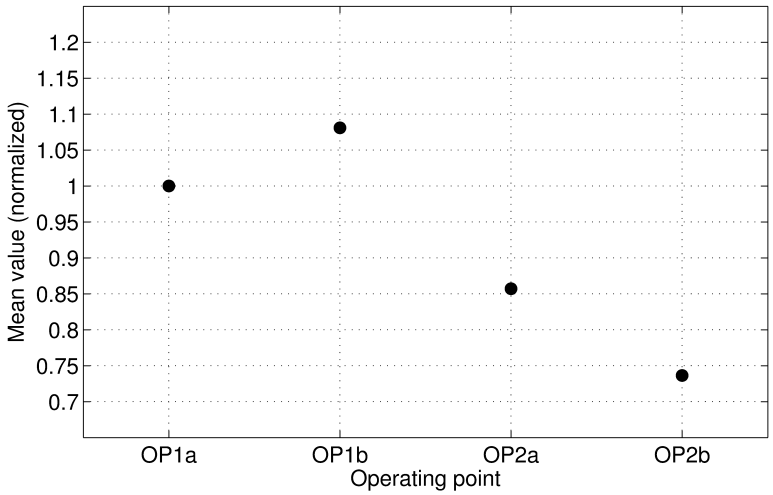

(a)

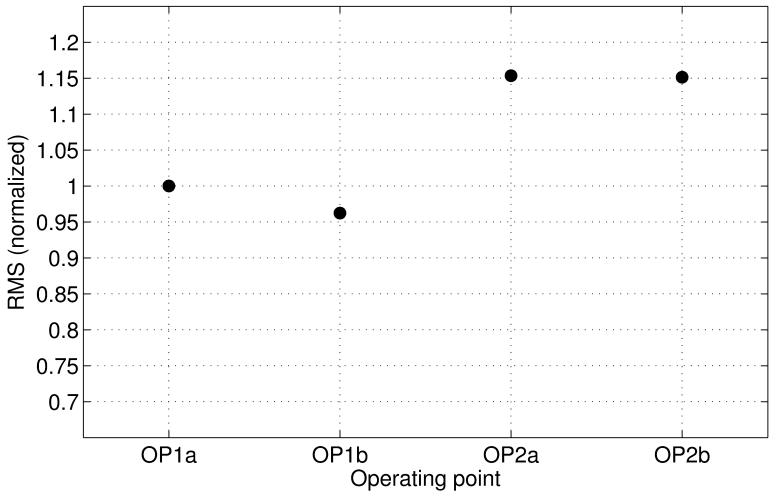

(b)

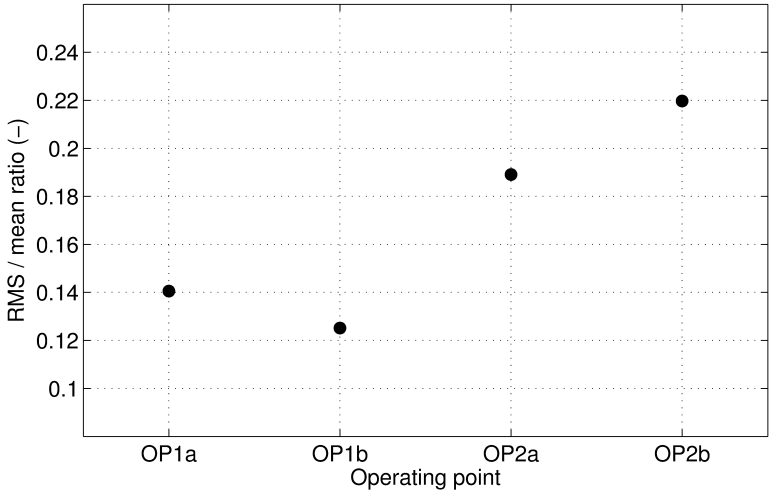

(c)

Fig. 9.12: Light emission analysis (integral data). Mean value (a), RMS (b), RMS/mean ratio (c)

9.9 Hysteresis

An issue of controlling the burner is that at some operating points two flame types are possible. Depending on the direction of parameter change, a specific shape is preferred. For instance, considering *Fig. 9.8*. The sequence was started at $\phi = 1$, where the burner produces an attached tubular flame (*Fig. 9.8c*). Subsequently, the equivalence ratio was gradually increased to $\phi = 1.87$, monotonically reduced to $\phi = 0.42$, and finally increased to $\phi = 1$ to obtain the images shown. However, in order to settle the flame on the rim of the exit nozzle when coming from $\phi = 0.42$, the equivalence ratio had to be increased to as high as $\phi = 1.7$ before coming back to $\phi = 1$. On the other hand, when coming from the rich regime, the flame remains attached until $\phi = 0.9$. *Figure 9.13* illustrates this hysteresis in terms of flame compactness with respect to the equivalence ratio qualitatively. The red arrows indicate the path into the rich regime, and the black into the lean. This burner produces a long tubular flame attached at the rim of the nozzle if the methane/air mixture is rich, a compact attached flame at the tip of the bluff body for lean mixtures and a compact lifted flame for mixtures in between. The changes in flame shape are sudden applying a certain degree of hysteresis, as mentioned before. Due to this fact, all investigations concerning stability limits have been started at the default operating point to ensure reproducibility.

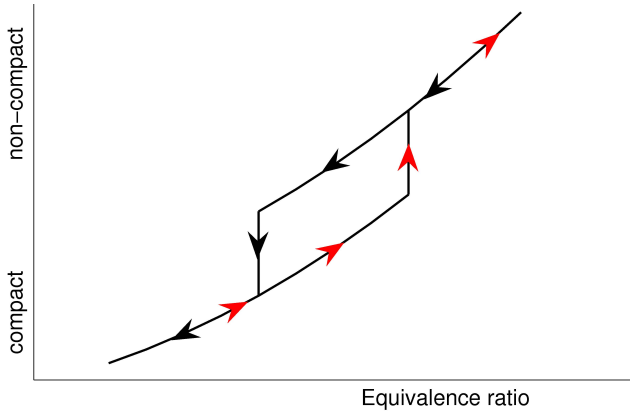

Fig. 9.13: Hysteresis of the flame compactness as a function of the equivalence ratio ϕ

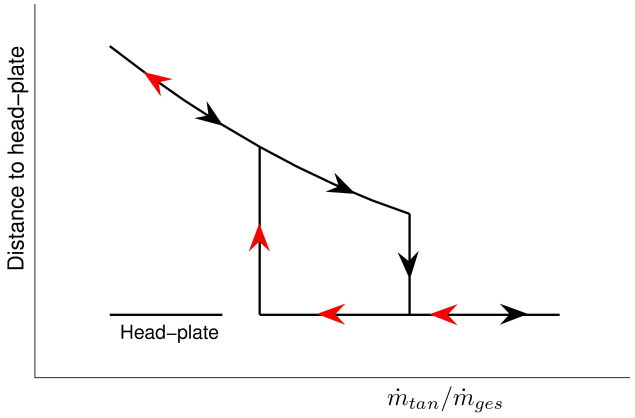

Fig. 9.14: Distance of the flame base to the head-plate as a function of the air mass flow split

The hysteresis behavior can also be qualitatively expressed in terms of the distance of the flame base to the head-plate as a function of the air mass flow split (*Fig. 9.14*). Generally, increasing the swirl strength forces the flame to move upstream, broadens it (*Fig. 9.6a* and *Fig. 9.6b*) and simultaneously has a shortening effect (*Fig. 9.9e* and *Fig. 9.9f*). If the swirl strength is too large, the flame will settle on the tip of the bluff body. Again, the transition happens suddenly with a certain degree of hysteresis.

9.10 Stability limits

The operational envelope of the burner in terms of thermal power over reduced mass flow $\dot{m}_{red}$ is depicted in *Fig. 9.15*. The grayed area between the black solid lines indicates the regime of a stable lifted flame employing fixed geometry. The default operating point (DP) which is indicated by a black dot, has sufficient margins to the transition borders. By reducing the overall air mass flow rate and keeping the fuel mass flow as well as the geometry parameters constant, the operating point shifts to the left into the rich regime. The flame will eventually settle then on the rim of the burner exit nozzle. By increasing the overall air mass flow at an unchanged fuel mass flow rate and geometry, the operating point is shifted to the right into the lean regime. The flame will settle finally on the center-body of the burner. For changes in overall air mass flow rate greater than 25 % the geometric parameters have to be adjusted to sustain a stable lifted flame. The hatched area between the blue solid lines indicates the regime for stable combustion employing variable geometry. For changes up to approx. 50 % of the air mass flow rate at a constant fuel mass flow rate, the burner produces a stable detached flame.

By changing the operating conditions at constant equivalence ratio ϕ, which is the more realistic scenario than keeping the fuel mass flow rate constant, flame transitions are also observed. This is indicated in *Fig. 9.15* by the red lines ranging from $\phi = 0.5$ to $\phi = 1.0$. When operating the burner at equivalence ratios between $\phi = 0.7$ and $\phi = 0.8$ the fixed geometry setup covers the gross of the operational envelope of the burner, i.e. drastic air mass flow reductions. At richer or leaner regimes the variable geometry setup is necessary to sustain a stable lifted flame.

What is more, applying variable geometry allowed shifting the lean blow-off limit (b/o) to higher reduced air mass flows by approximately 5 %. The two solid lines on the right in *Fig. 9.15* are indicating the limits for the fixed (black) and variable (blue) geometry setups. The rich blow-off limit on the left could not be reached as the experiments were performed under unconfined conditions and sufficient oxygen was provided by the ambient air.

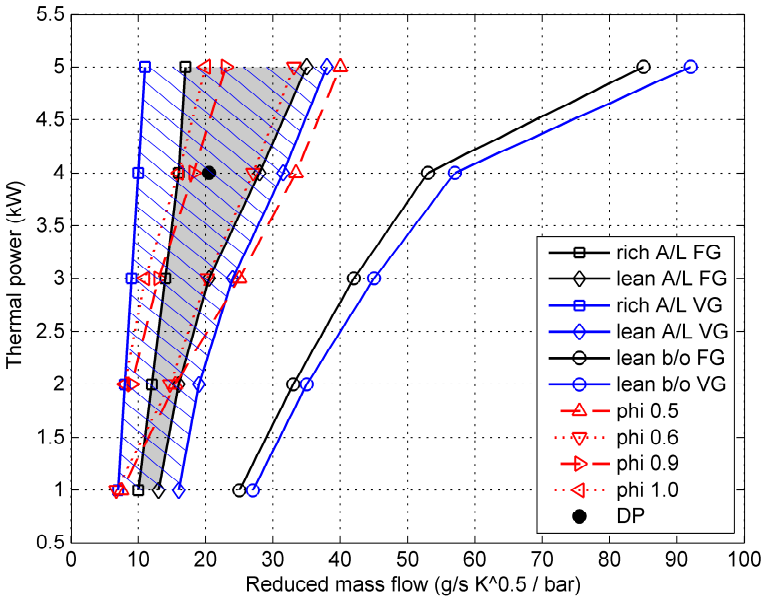

Fig. 9.15: Stability limits at atmospheric unconfined conditions. Shown are the regimes for a stable lifted flame applying fixed and variable geometry as well as the lean blow-off limits.

Figure 9.16 was deduced from *Fig. 9.15*. It shows the flame regimes as a function of equivalence ratio ϕ and reduced mass flow $\dot{m}_{red}$. The transitions of the flame shape are more evident here than in *Fig. 9.15* and variable geometry enables to sustain a lifted flame up to the half of the air mass flow met at the fixed geometry transition boundary.

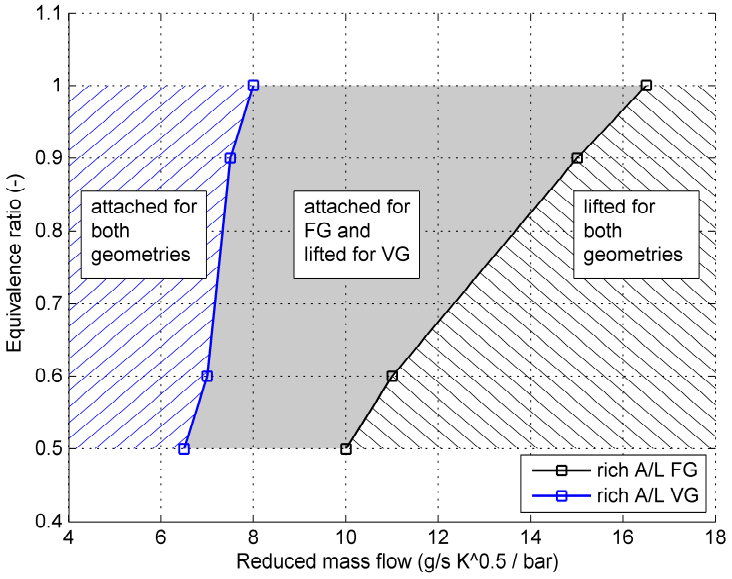

Fig. 9.16: Flame shapes as function of reduced mass flow and equivalence ratio

In *Fig. 9.17* the flame regimes are shown as a function of thermal power P and equivalence ratio ϕ. It seems that the actuation system is more efficient at richer and higher loaded operating points as the margins between the fixed and the variable geometry transition boundaries increase (grayed area).

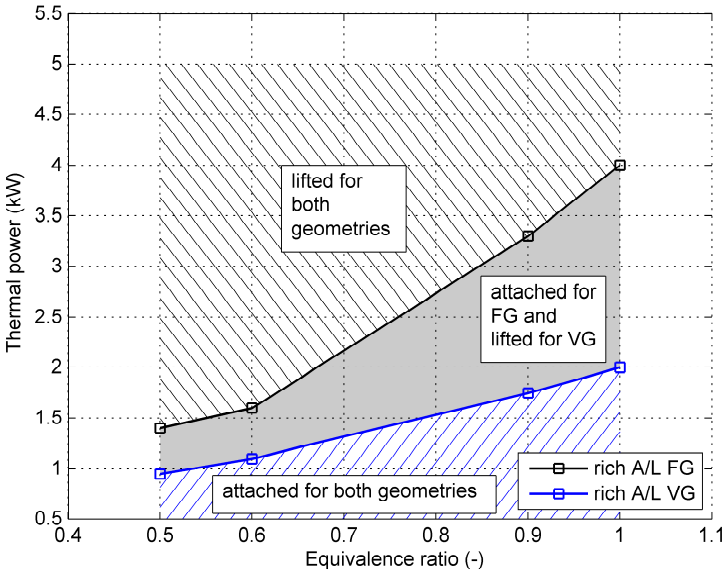

Fig. 9.17: Flame shapes as function of equivalence ratio and thermal power

9.11 Flame influence zone

The schlieren visualization technique was used to identify the flame influence zone at different operating points. *Figure 9.18* is an overlay of the light emission of CH^*-radicals and the density gradients. The head-plate of the burner, which was operated vertically, is also shown at the bottom of the figures. Exposure time of the camera was set to 1/50 sec, aperture and gain have been set automatically. The light emission shows the main reaction zone (the position) of the flame at the different operating points. The density gradients depict the influence zone of the flame which is significantly greater than the core of the flame. These zones are indicated in *Fig. 9.18a* by dotted lines. At the default operating point OP1a the burner produces a stable lifted flame which settles approximately 22 mm above the burner head-plate (*Fig. 9.18a*). By increasing the swirl and keeping the overall mass flow rate constant (operating point OP1b) the flame broadens slightly and simultaneously moves upstream in order to settle around 11 mm above the head-plate (*Fig. 9.18b*). Reducing the mass flow rate compared to OP1a results in an attached flame (*Fig. 9.18c*). The flame settles at the outer ring of the burner exit nozzle and has an elongated tubular shape. By reducing the nozzle exit area, the axial velocity at the exit plane of the burner nozzle is increased. As a result, the flame detaches and settles at approximately 29 mm above the burner head-plate (*Fig. 9.18d*). The flame has gained its compact shape again. These images additionally illustrate, that the influence zone of the flame is significantly larger than the main reaction zone.

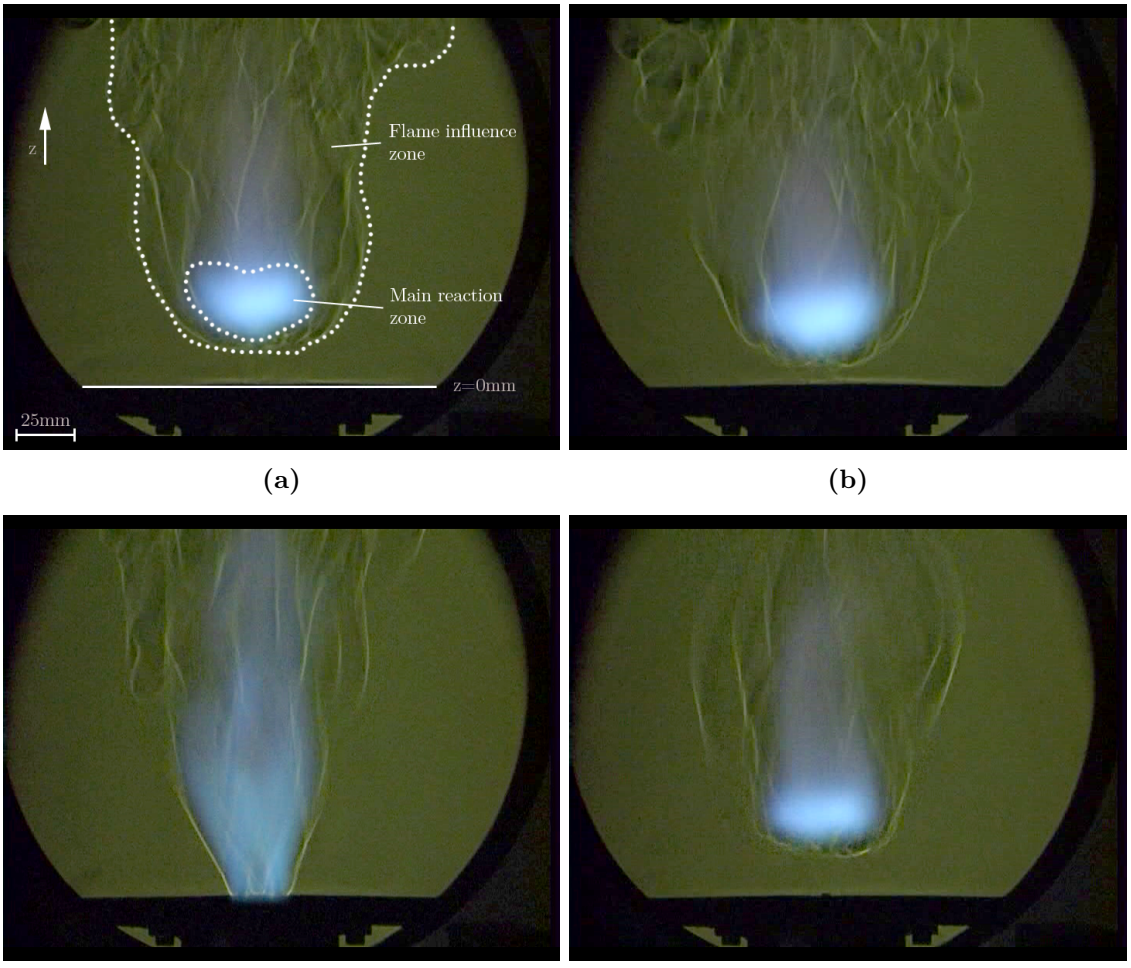

Fig. 9.18: Overlay of schlieren visualization and light emission of CH*-radicals. The light emission shows the position of the flame. The influence zone is depicted by the density gradients. OP1a (a), OP1b (b), OP2a (c), OP2b (d)

Figure 9.19 depicts the density gradients at the operating points OP1a, OP1b, OP2a, and OP2b. Exposure time, aperture, and gain were set to 1/8000 sec, open, and 0 dB, respectively. With the settings used only the density gradients are visible (compared to *Fig. 9.18*). These images reveal strong degrees of turbulence within the main reaction zone of the flame which are characterized by small structures. At the flame borders large structures are observed which are buoyancy driven.

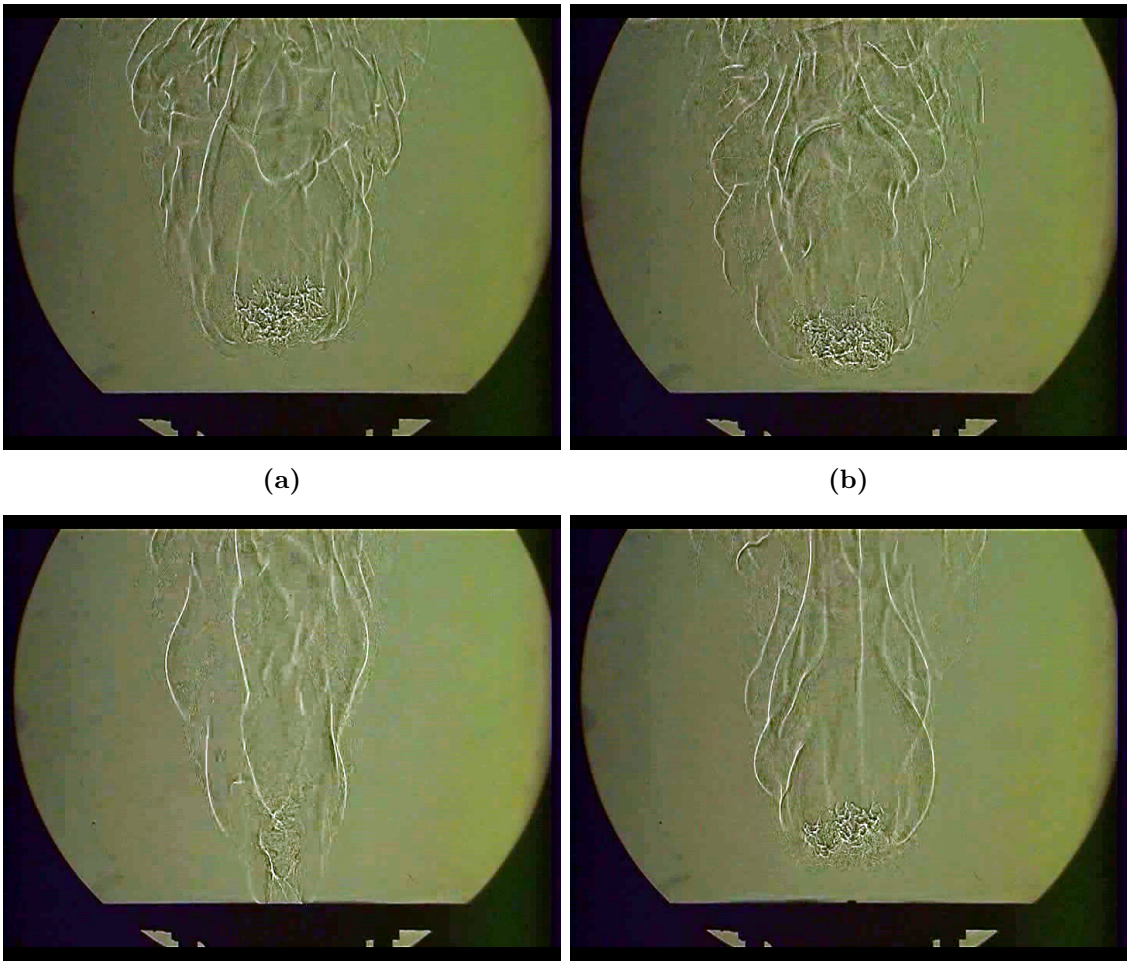

(a) **(b)**

(c) **(d)**

Fig. 9.19: The density gradients reveal strong turbulence (small structures) within the flame and big structures at the flame front, which are buoyancy driven. OP1a (a), OP1b (b), OP2a (c), OP2b (d)

In contrast to *Fig. 9.18* and *Fig. 9.19*, which are snapshots, *Fig. 9.20* was created out of sets of 300 frames. For each subfigure only the brightest pixel value at a specific pixel position has been considered, producing bright traces which again show small structures within the core of the flame and large structures at the border of the influence zone. Additionally, the swirling nature of the flame is indicated by the turning traces of the large structures. Above the zones of high turbulence a unified density distribution is prevalent as there are no (or weak) density gradients visible. The settings of the sole images of exposure time, aperture, and gain were set to 1/8000 sec, open, and 0 dB, respectively. The image stack has been performed in Matlab R2009b.

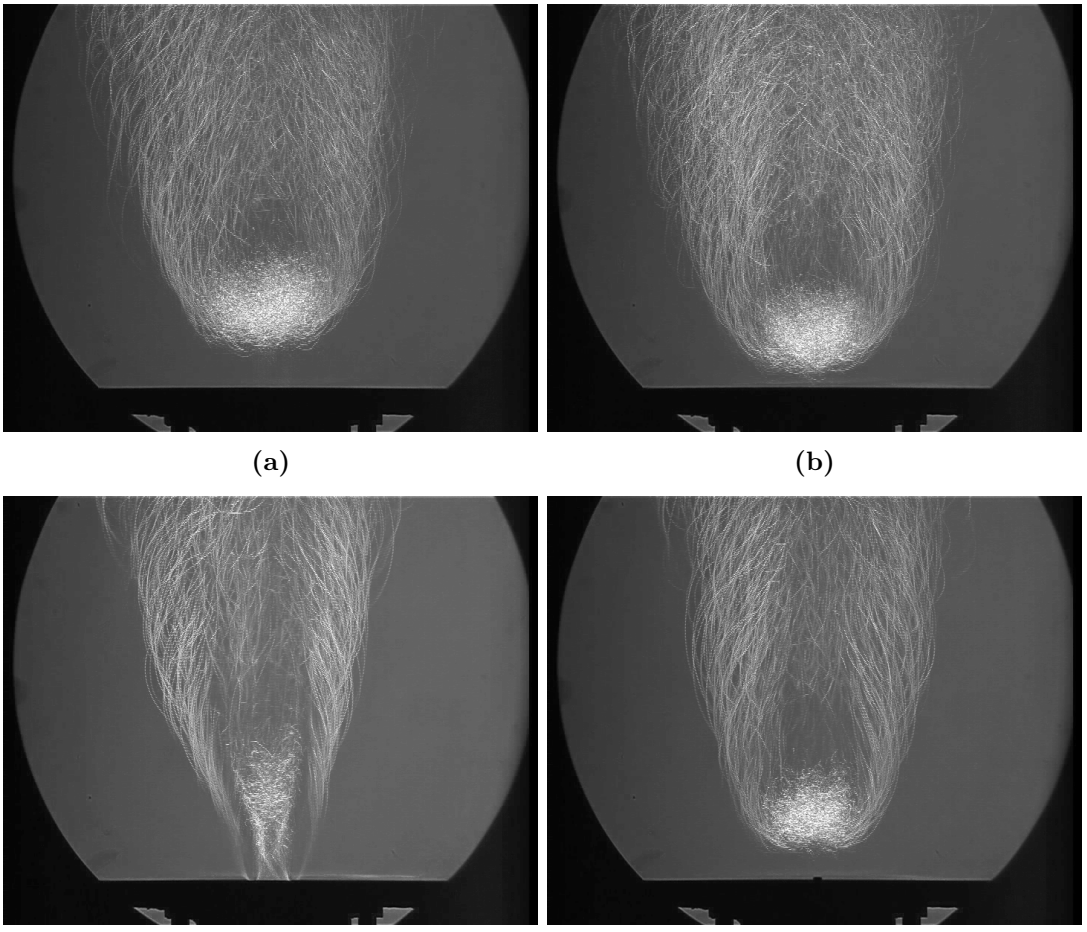

(a) **(b)**

(c) **(d)**

Fig. 9.20: Shown are the brightest pixel values of a set of 300 frames producing streamlines. OP1a (a), OP1b (b), OP2a (c), OP2b (d)

9.12 Flow field

The flow field has been obtained through 3C PIV measurements, as explained in *Sec. 5.2*, under unconfined conditions. The laser light sheet was aligned longitudinally to the burner (within the z-x plane), intersecting the central axis, as shown in *Fig. 9.21*. Field of view is from height $z = 12\,\text{mm}$ to $z = 50\,\text{mm}$ and from radius $r = -25\,\text{mm}$ to $r = 25\,\text{mm}$.

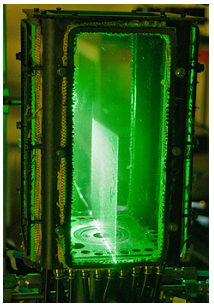

Fig. 9.21: Laser light sheet intersecting the burner axis

Figure 9.22a - *Fig. 9.22d* illustrate the total velocity flow field with arrows indicating the axial-radial velocity vector. The maxima of the total velocity for the operating point OP1a (*Fig. 9.22a*) are in a height of $z = 40\,\text{mm}$. Due to the asymmetry of the flame the right maxima is positioned slightly downstream. Clearly visible are regions of low velocities which are directly downstream of the exit nozzle and sideways at the bottom of the flame. *Figure 9.22b* depicts the flow field at OP1b. Due to the increased swirl strength, the maxima are shifted upstream by approximately 10 mm. Also the inner recirculation zone (IRZ) is widened and slightly shortened. The maximum velocities in the two prongs seem to be lower than in OP1a, which can be due to the increased swirl. As there are four tangential inlet slots within the burner, a stronger swirl intensity may shift the tangential position of the prongs relative to the laser light sheet. This is also observed by the reconstructed flame shapes obtained through light emission measurements (*Fig. 9.7a* and *Fig. 9.7b*). At both operating points, the flow velocity increases further downstream due to the thermal expansion of the gas.

The total velocity field at OP2a (reduced mass flow rate) is shown in *Fig. 9.22c*. Clearly visible is the tubular shape of the flame with a low velocity region inside. Outside the flame the number of sufficient validated vectors is low which is characterized by the noisy signal. This is because of the low concentration of seeding particles in this area. As the flame is attached at this operating point, no sudden thermal expansion occurs. Therefore, the flow velocity decreases further downstream. In order to detach the flame, the nozzle area was decreased. *Figure 9.22d* shows the according total velocity flow field. Compared to *Fig. 9.22c* the exit nozzle velocity increased which anchors the flame at approximately 29 mm downstream of the head-plate. Again, further downstream the flow velocity accelerates, which is due to thermal expansion. The altered nozzle geometry produces a narrower flame shape compared to those obtained at OP1a and OP1b. Outside the flame region, the seeding concentration is higher compared to the one in OP2a. This might be due to the more turbulent behavior of the flame, resulting in an increased signal-to-noise ratio.

Figure 9.22e - *Fig. 9.22h* illustrate the axial velocity flow fields. As already shown in the total velocity flow fields, distinctive velocity maxima are again observed in the axial velocity flow field for the operating points OP1a (*Fig. 9.22e*) and OP1b (*Fig. 9.22f*), which differ in axial and radial position due to the variation in swirl strength. Different magnitudes of velocity are observed in the prongs at the bottom of the flame, which may be related to the four inlet slots and the swirl strength, as already noticed in the total velocity flow field. However, due to the thermal expansion of the gas the axial velocity increases further downstream at both operating points.

The axial velocity flow field at the operating points OP2a and OP2b is depicted in *Fig. 9.22g* and *Fig. 9.22h*, respectively. As in the total velocity flow field, the tubular shape of the attached flame at OP2a is shown very nicely. At this operating point, the velocity decreases gradually when moving further downstream, in contrast to OP2b. As mentioned before, at OP2b the axial gas velocity increases downstream due to the thermal expansion of the detached flame.

The tangential velocity flow fields (*Fig. 9.23a* - *Fig. 9.23d*) look differently compared to the total and axial fields, as shown in *Fig. 9.22*. First of all, the maximum tangential velocities reach only 50 % of the total and axial velocities. Secondly, the flow field turns around the central burner axis. The influence of the increased swirl strength at OP1b compared to OP1a, results in a larger zone of higher tangential velocity, which is slightly more slanted, shown in *Fig. 9.23b*. The tangential flow field of OP2a is depicted in *Fig. 9.23c*. Compared

to the other figures, the velocity decreases monotonically when moving downstream. Due to the poor seeding concentration sideways of the flame and to the fact that the number of validated vectors is low, noise is increased. However, the main information is not affected. When decreasing the exit nozzle area, the zone of high tangential velocities is shortened significantly (*Fig. 9.23d*). As the flame is detached at this operating point and hence turbulence is increased, the seeding concentration outside the flame is higher, resulting in a better signal-to-noise ratio sideways of the flame.

When considering the radial velocity flow fields, as shown in *Fig. 9.23e* - *Fig. 9.23h*, three zones can be detected at all operating points, which are characterized by the sign or magnitude of the velocity. What is common to all zones is that they are widened when moving downstream. The middle zone, entailing the burner central axis, is a region with no or low radial velocity. Due to the introduced swirl, air is forced to flow outwards, which is illustrated by the two outer zones. In hot regions, local maxima are detected, which can be seen at operating points OP1a, OP1b and OP2b. The maxima of the radial velocities at OP1b (*Fig. 9.23f*) are moved upstream by approximately 10 mm compared to OP1a (*Fig. 9.23e*). These maxima are of the order of the tangential velocities mentioned above. At OP2a (attached flame), no distinct maxima are observed, as within the field of view no hot spots are detected.

Figure 9.24, *Fig. 9.25* and *Fig. 9.26* show lineplots of axial, tangential and radial velocities, respectively. These plots are extracted from the velocity flow fields discussed above. Plots are shown at axial distance of 15 mm ($z/D \approx 0.8$), 18 mm ($z/D = 1$), 25 mm ($z/D \approx 1.4$) and 35 mm ($z/D \approx 2$) for the operating points OP1a, OP1b, OP2a and OP2b. Due to the low seeding concentration near the head-plate noised results for the tangential and radial velocities are observed at the operating points OP2a and OP2b, especially at $z = 15$ mm and $z = 18$ mm.

From the PIV measurements, the swirl number S, as defined in *Sec. 3.1.1*, and the turbulence level T_U at $z/D \approx 2$ have been derived. This distance was chosen in order to avoid regions of low seeding concentration. The turbulence level was calculated as the ratio of the total RMS velocity $V_{tot,RMS}$ and the total velocity V_{tot}, as shown in *Eq. (9.2)*.

$$T_U = \frac{V_{tot,RMS}}{V_{tot}} \tag{9.2}$$

The swirl number increases by 30 % from OP1a to OP1b which is due to the increased tangential velocity component. The same elevated swirl number is detected at OP2a; by increasing the axial velocity component at OP2b, it decreases to nearly the value of OP1a again. Furthermore, it seems that the turbulence level is a function of the exit nozzle area as turbulence increases drastically, by 100 %, with a reduced exit area. It also corresponds to the light emission fluctuations calculated for the whole flame regime shown in *Fig. 9.12c*. Values for swirl number S and turbulence level T_U for the specific operating points are listed in *Tab. 9.3*.

Tab. 9.3: Swirl number S and turbulence level T_U at different operating points

	OP1a	OP1b	OP2a	OP2b
Swirl number S	0.36	0.47	0.47	0.33
Turbulence level T_U (%)	30	26	25	51

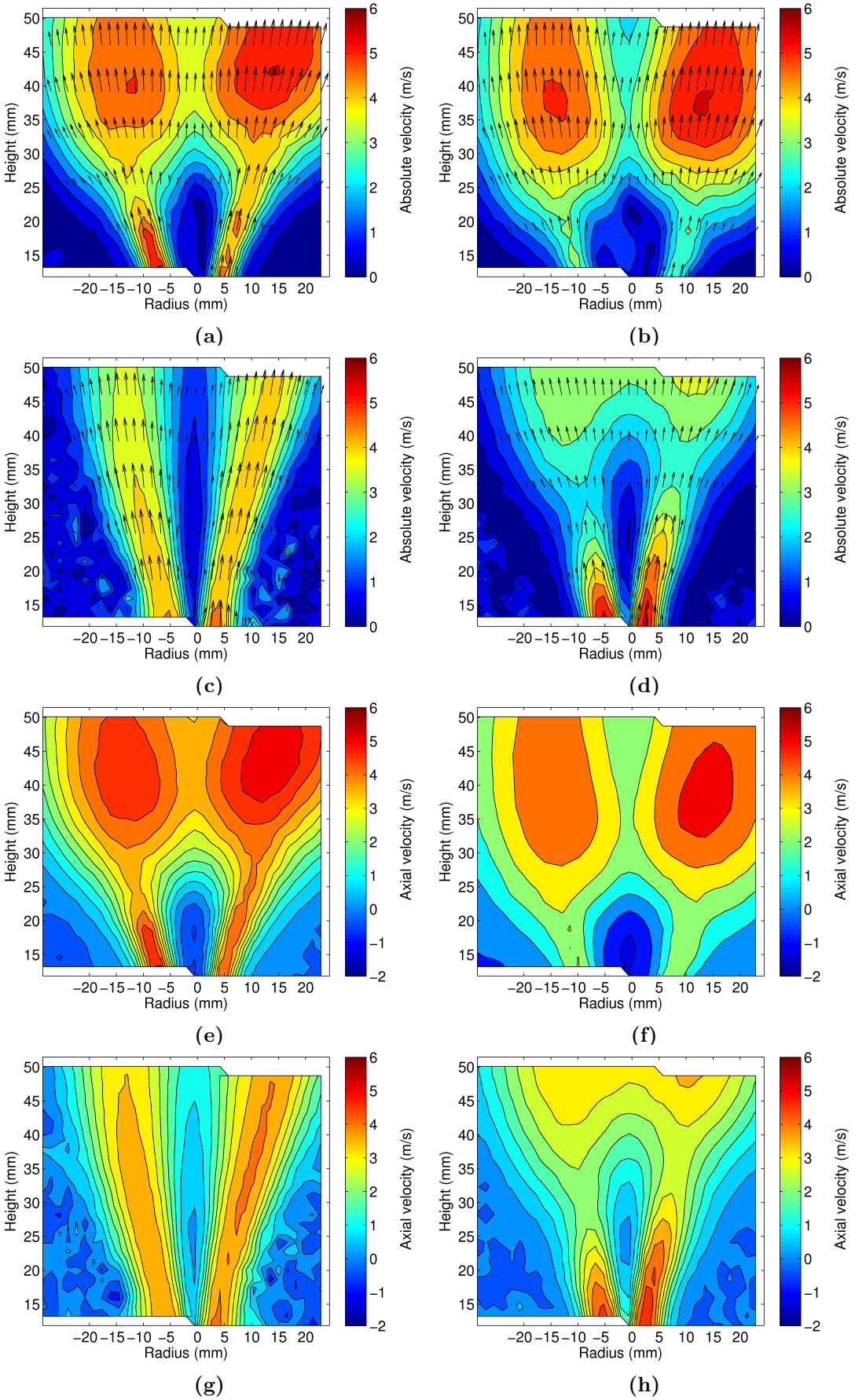

Fig. 9.22: Averaged total and axial velocity fields. Total: OP1a (a), OP1b (b), OP2a (c), OP2b (d). Axial: OP1a (e), OP1b (f), OP2a (g), OP2b (h)

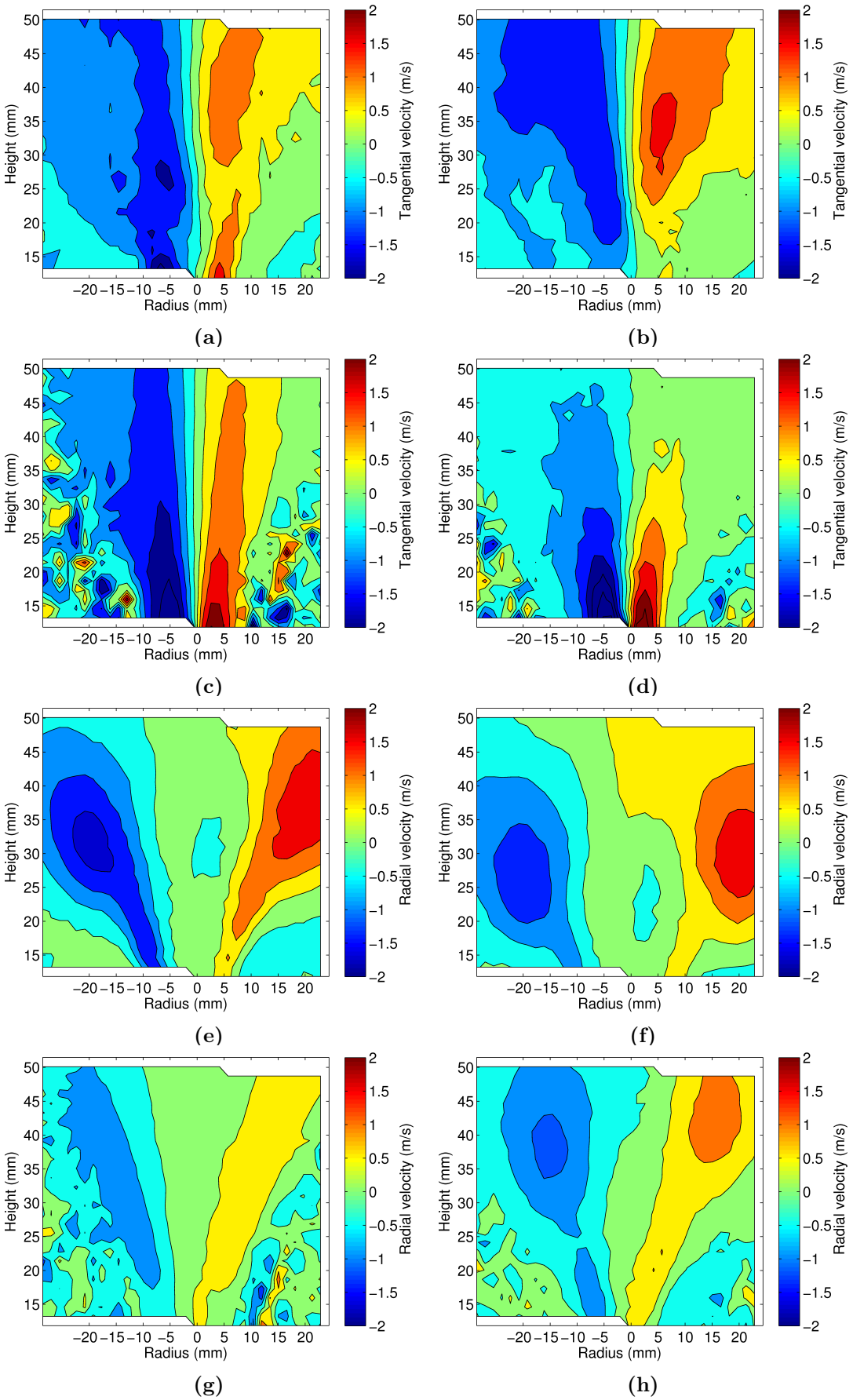

Fig. 9.23: Averaged tangential and radial velocity fields. Tangential: OP1a (a), OP1b (b), OP2a (c), OP2b (d). Radial: OP1a (e), OP1b (f), OP2a (g), OP2b (h)

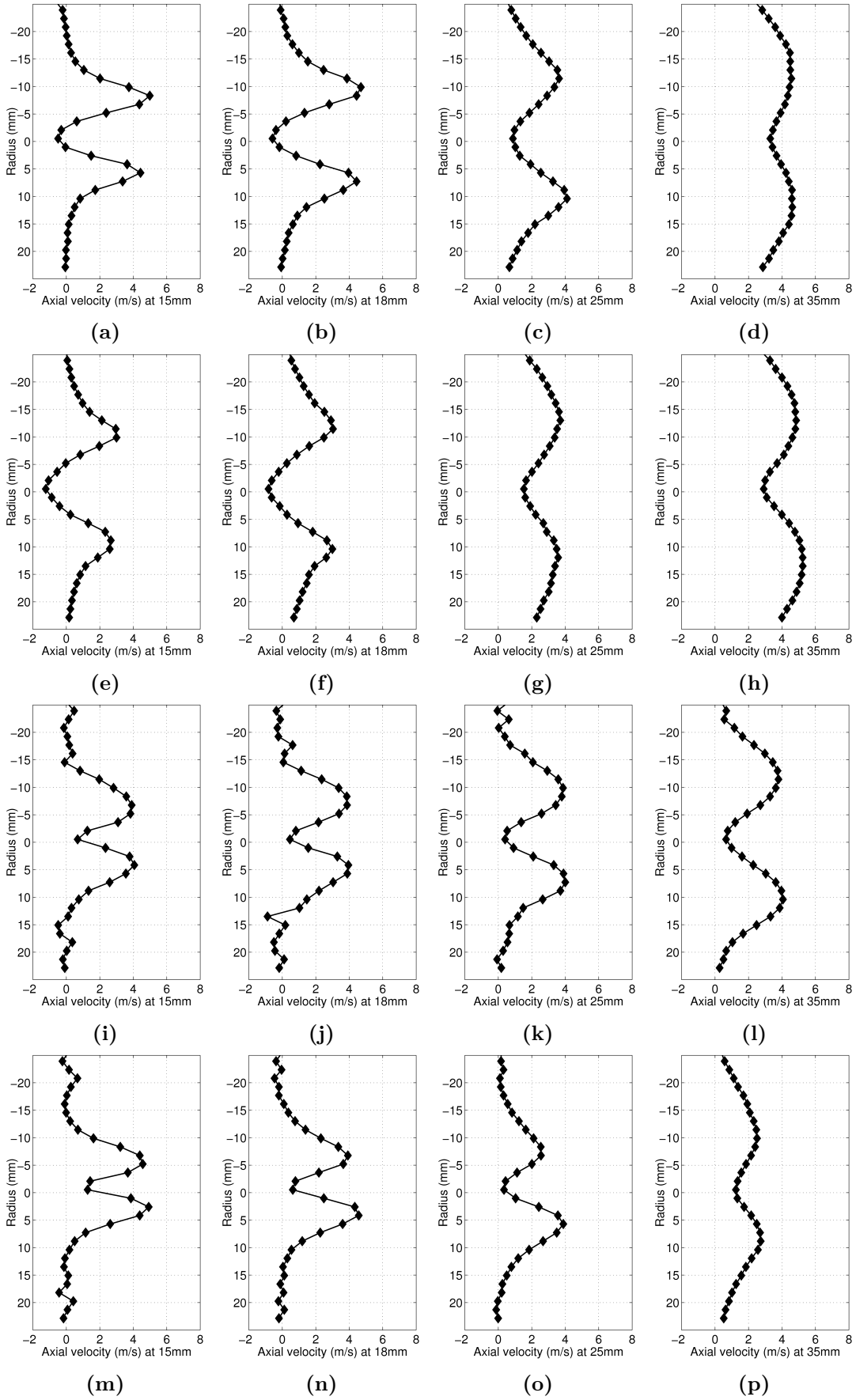

Fig. 9.24: Profiles of averaged axial velocities at different operating points. OP1a (a)-(d), OP1b (e)-(h), OP2a (i)-(l), OP2b (m)-(p)

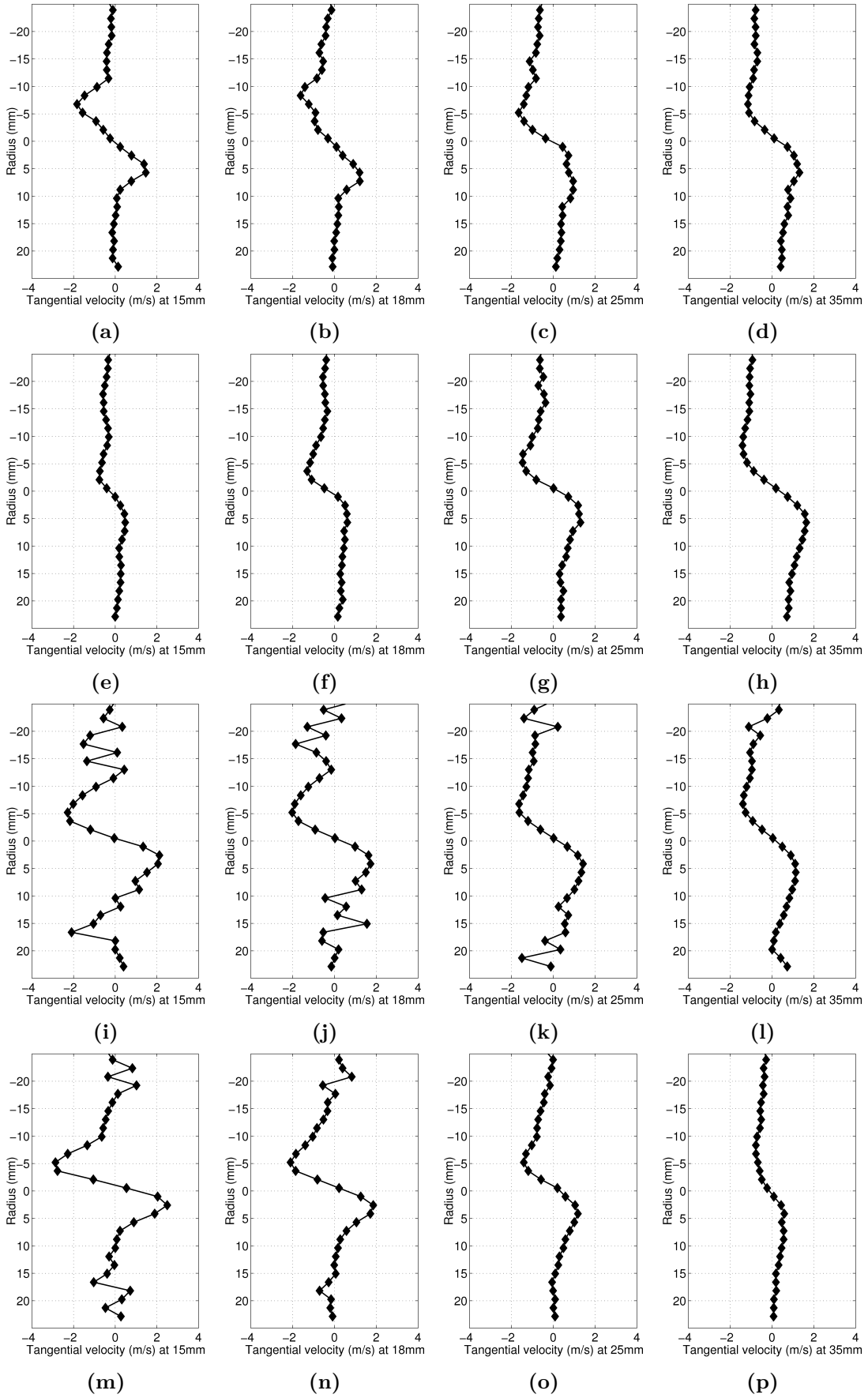

Fig. 9.25: Profiles of averaged tangential velocities at different operating points. OP1a (a)-(d), OP1b (e)-(h), OP2a (i)-(l), OP2b (m)-(p)

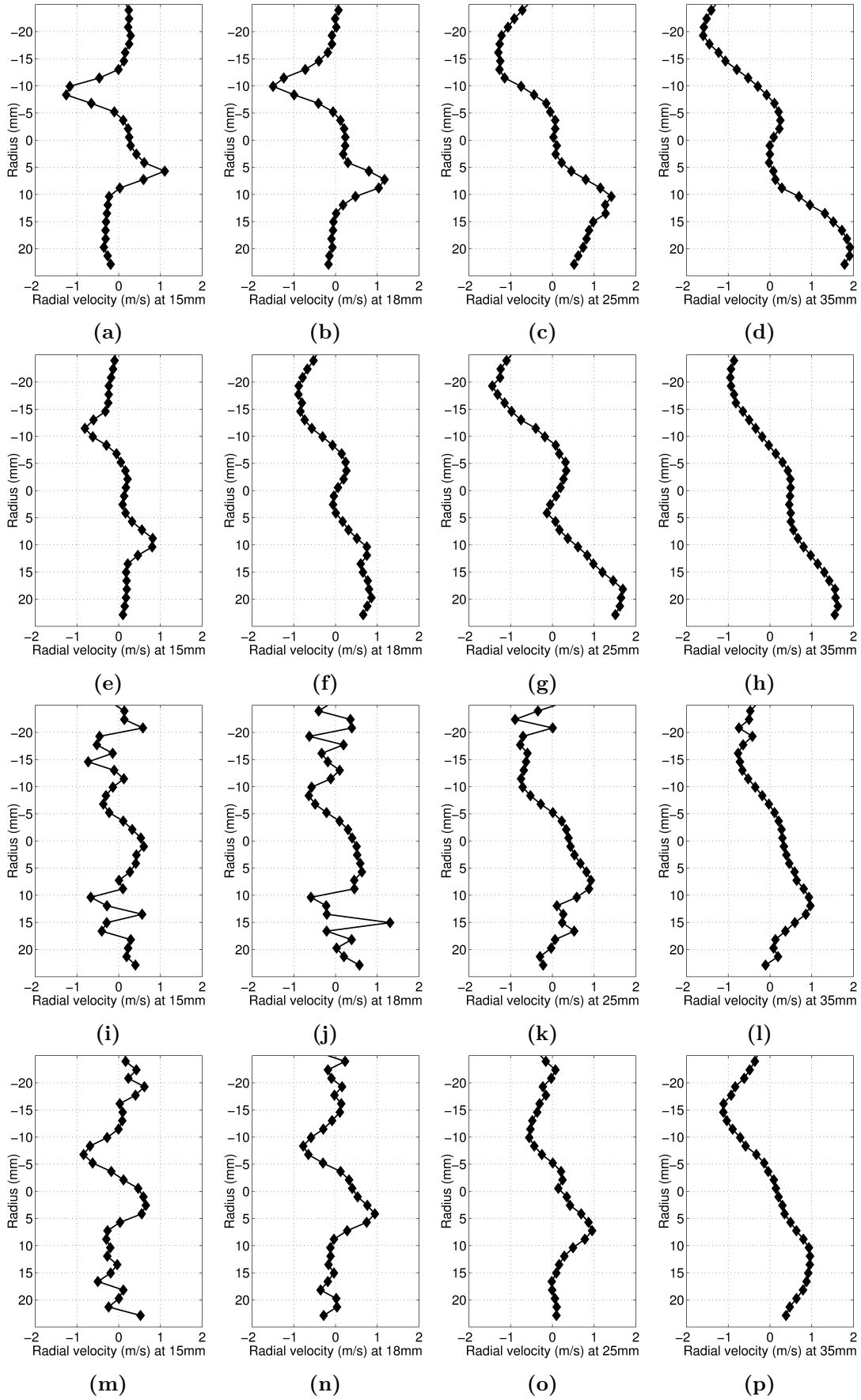

Fig. 9.26: Profiles of averaged radial velocities at different operating points. OP1a (a)-(d), OP1b (e)-(h), OP2a (i)-(l), OP2b (m)-(p)

9.13 Temperature distributions

The temperature distributions shown in *Fig. 9.27* - *Fig. 9.29* have been obtained by Raman measurements explained in *Sec. 5.6*. Illustrated are 2d-plots in radial direction within $x = \pm 17\,\text{mm}$ at three different heights z. Shown are single measurement results (black dots) and moving average curves (red lines) calculated from 15 measurement samples.

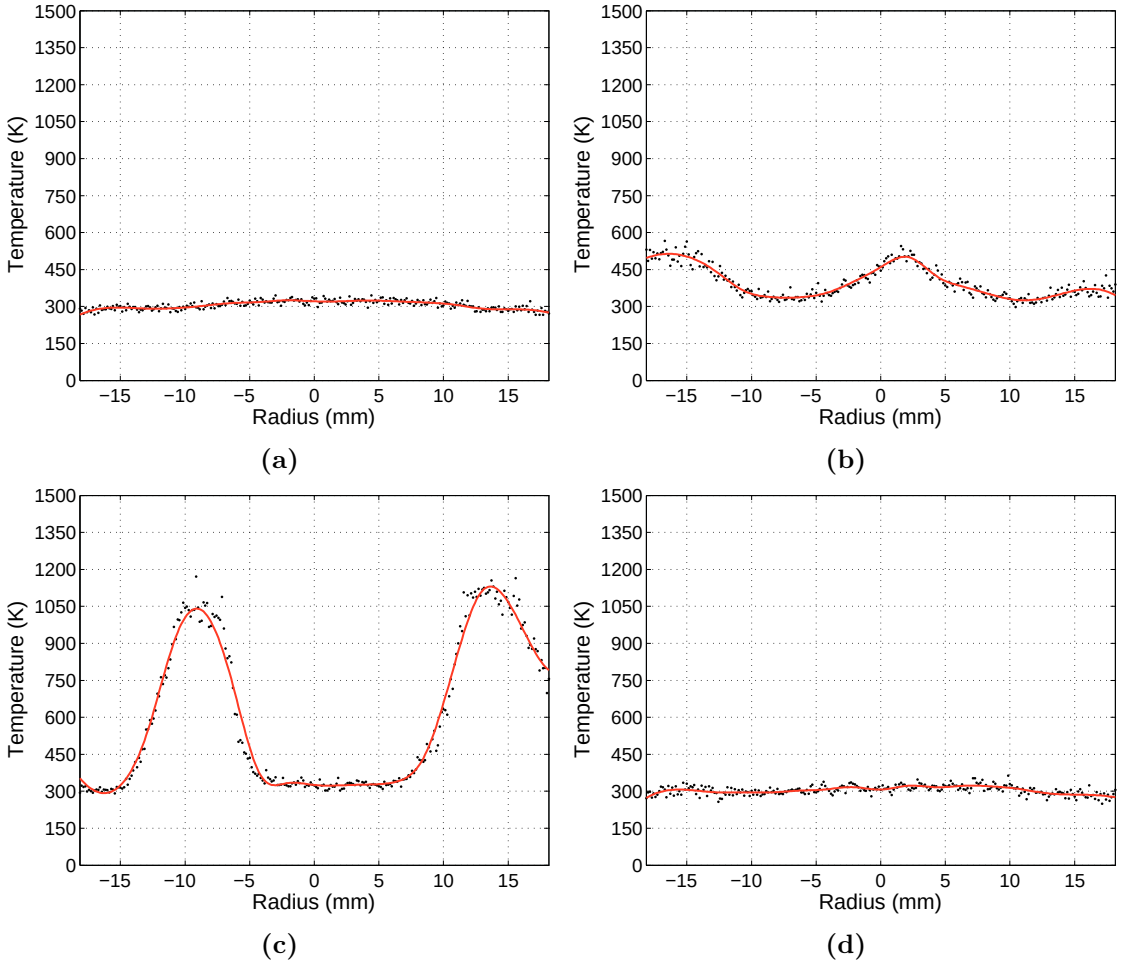

Fig. 9.27: Temperature distribution at $z = 10\,\text{mm}$. OP1a (a), OP1b (b), OP2a (c), OP2b (d)

Figure 9.27 shows the temperature distributions at $z = 10\,\text{mm}$ for the operating points OP1a - OP2b. As expected, for the points OP1a and OP2b temperatures are around ambient as the measurement positions are well below the flame reaction zone (lifted flame). OP1b has already an elevated temperature level due to the upstream shifted flame. Three distinct peaks are observed which correspond to the flame shape. The different outer peak values indicate the swirling character of the flame as four prongs are produced by the finite number of inlet slots as already discussed in *Sec. 9.12*. The maximum temperature of 500 K can be found near the burner central axis. A different temperature distribution is observed at OP2a as the flame is attached on the burner exit nozzle. Two peaks can be found, which mark the reaction zone and illustrate the tubular shape of the flame. The maximum value is around 1100 K. A slight eccentricity of 2 mm is observed which may

be due to a misalignment of the measurement system. Due to the calculated equivalence ratio $\phi = 0.7$ peak temperatures around 1400 K have been expected, however, the actual temperature level corresponds rather to $\phi \approx 0.4$ than to 0.7. Two possible reasons may be responsible for this discrepancy. Either ambient air is diluting the fuel/air mixture more than expected or the differences are due to the missing anti-Stokes bands (observed at temperatures higher than 2000 K) and hence the iterative evaluation algorithm of the Raman technique.

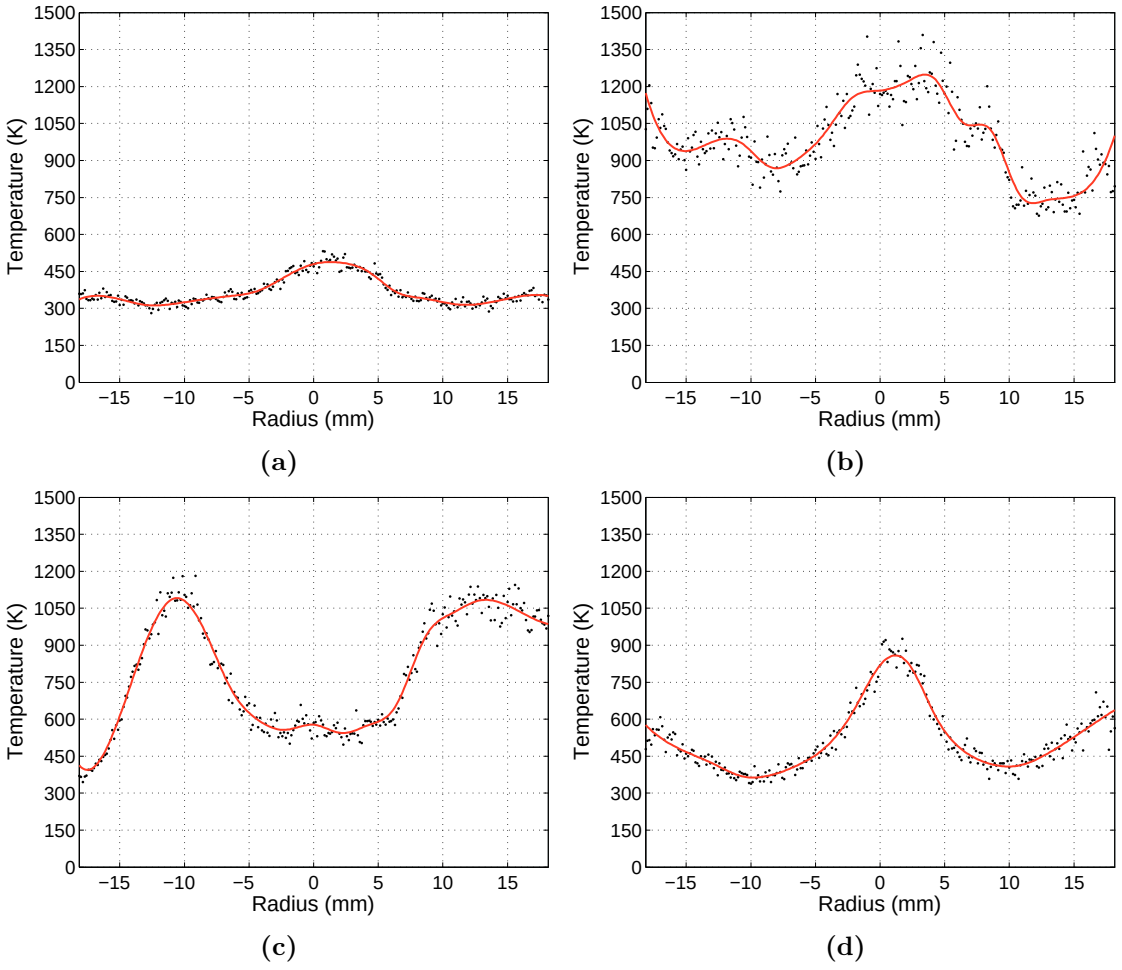

Fig. 9.28: Temperature distribution at $z = 25$ mm. OP1a (a), OP1b (b), OP2a (c), OP2b (d)

As the measurement positions in *Fig. 9.28* ($z = 25$ mm) are closer to the reaction zone, the temperature levels are in general higher than in *Fig. 9.27* ($z = 10$ mm). The spreading of the measured values increases in zones of higher turbulence (main reaction zones) and can reach ±100 K compared to ±20 K at ambient conditions. At OP1a a peak is observed in the center with a maximum value of 500 K, at radii ±12 mm temperature reaches ambient level and slightly increases at ±16 mm. The temperature distribution at OP1b (*Fig. 9.28b*) transforms drastically compared to *Fig. 9.27b*. First of all, the peak temperature reaches nearly 1250 K. Secondly, the central peak broadens and the peaks at the sides shift radially outwards. Due to the turbulent behavior, spreading increases as mentioned above. For the attached flame (OP2a) at $z = 25$ mm, the temperature distribution changes slightly.

The two peaks remain unchanged, except the temperature level inside the tubular flame increases up to approximately 600 K. At OP2b a peak in the center is observed as at OP1a, however, the maximum temperature is as high as 900 K. At larger radii, temperature reaches approximately 600 K.

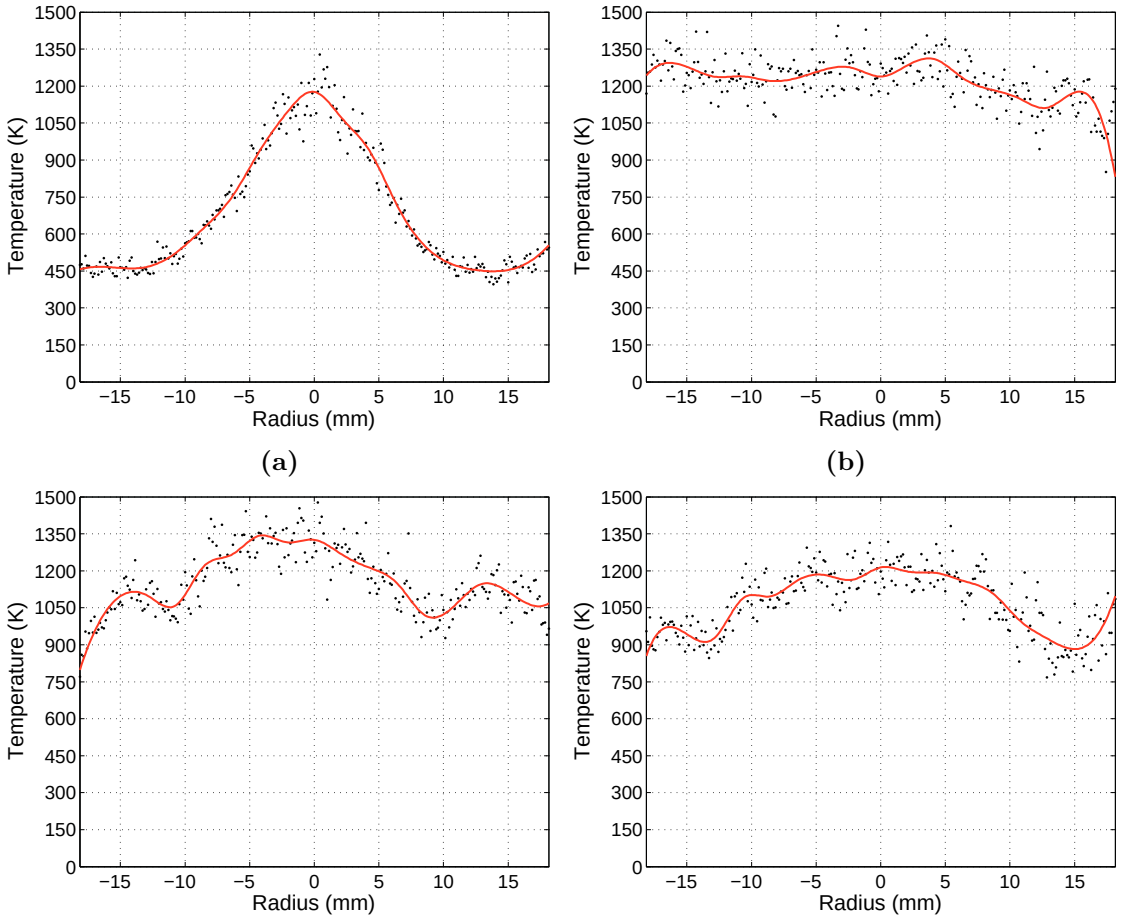

Fig. 9.29: Temperature distribution at $z = 35$ mm. OP1a (a), OP1b (b), OP2a (c), OP2b (d)

Figure 9.29 illustrates the temperature distributions at $z = 35$ mm. At OP1a a distinct peak is formed with a mean maximum temperature of approximately 1200 K. Unlike the other operating points (OP1b to OP2b), temperature decreases with increasing radius to 450 K. The other operating points (OP1b, OP2a and OP2b) produce a broad inner peak, and temperatures are not falling below 900 K. Maximum temperatures are around 1300 K. It is interesting to note, that at OP2a the temperature level at the center increased from 600 K (*Fig. 9.28c*) to 1300 K (*Fig. 9.29c*).

9.14 Density distributions

With shearing interferometry, a measurement technique explained in *Sec. 5.5*, it is possible to obtain absolute numbers of density if the phase difference $\Delta\phi$ (equivalent to density gradient), the Gladstone-Dale constant G, the laser light wavelength λ, and the shear δ, according to *Eq. (5.22)*, are known. However, as only the four specific operating points OP1a, OP1b, OP2a and OP2b will be compared to each other and as G, λ and δ can be assumed constant, $\int \Delta\phi$ will be displayed as it is equivalent to the density ρ.

Shearing interferometry provides integral data at first, however, with the tomographic reconstruction technique explained in *Sec. 5.3.2*, local information has been obtained. Artifacts, which may occur at larger radii due to the reconstruction algorithm, have been tried to suppress by interpolating between adjacent projections.

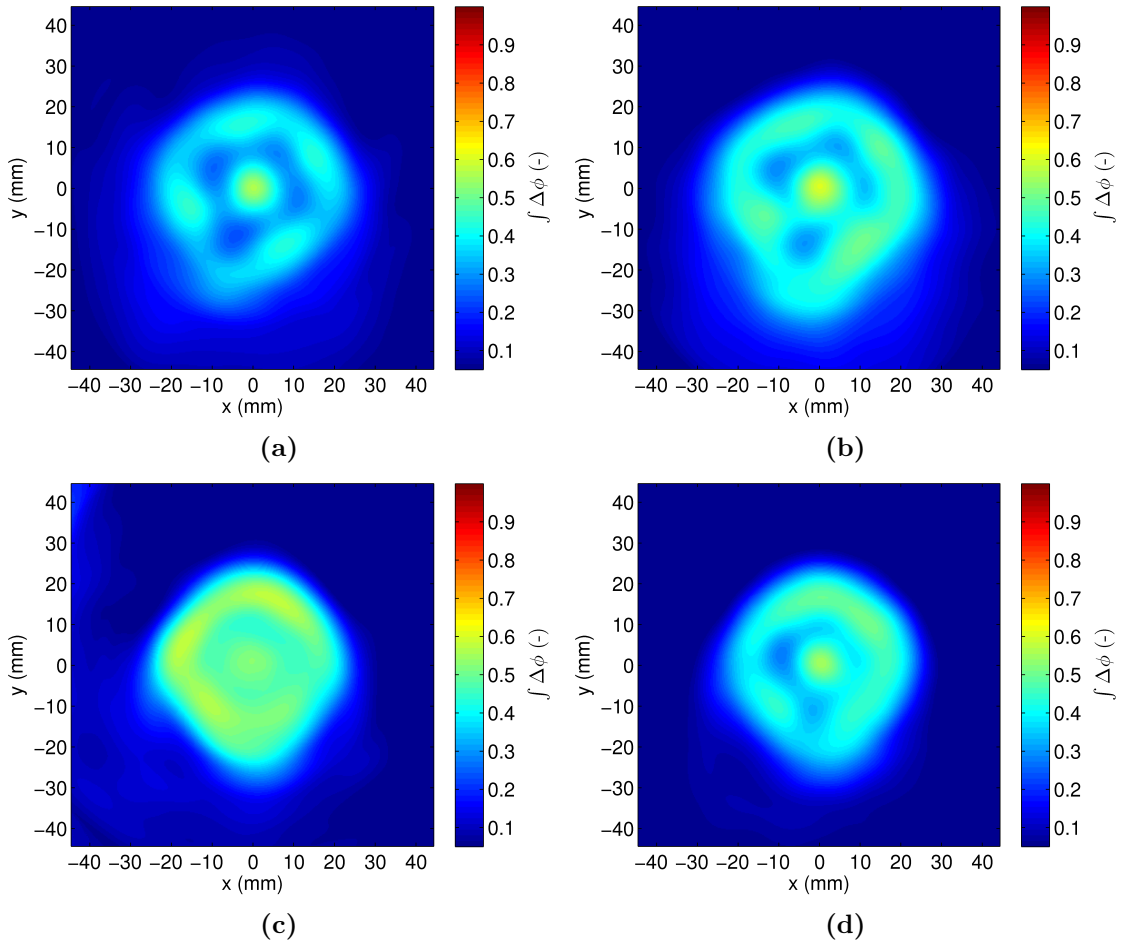

Fig. 9.30: Density distribution within the x-y plane at $z = 25\,\text{mm}$. OP1a (a), OP1b (b), OP2a (c), OP2b (d)

The density distributions in terms of $\int \Delta\phi$ of the operating points OP1a, OP1b, OP2a and OP2b in the x-y plane at height $z = 25\,\text{mm}$ are illustrated in *Fig. 9.30*. Regions of low density are identified by the bright zones. What is common to all operating points, are the four prongs due to the tangential inlet slots. These are more or less developed depending on the axial flame position, and are arranged circumferentially at a radius of approximately 18 mm. For the tubular flame (*Fig. 9.30c*) these prongs are hardly visible.

There are also low-density regions observed in the center of all flames, which are clearly visible at the operating points OP1a, OP1b and OP2b. The burner produces a slightly asymmetric flame, which is nicely illustrated by *Fig. 9.30*.

Figure 9.31 - *Fig. 9.33* show lineplots of $\int \Delta\phi$ (equivalent to density) in the z-x plane ($y = 0$) at three different heights z. At $z = 10\,\text{mm}$ (*Fig. 9.31*) only the attached tubular flame produces a noticeable density change, shown in *Fig. 9.31c*. The minima are positioned at $x = \pm 12\,\text{mm}$ and illustrate the tubular flame shape. Another minima is observed at the burner central axis. The fluid in the wake of the center-body may be heated by the surrounding hot zones. At all other operating points nearly no density change is observed as the measurement positions are below the reaction zones.

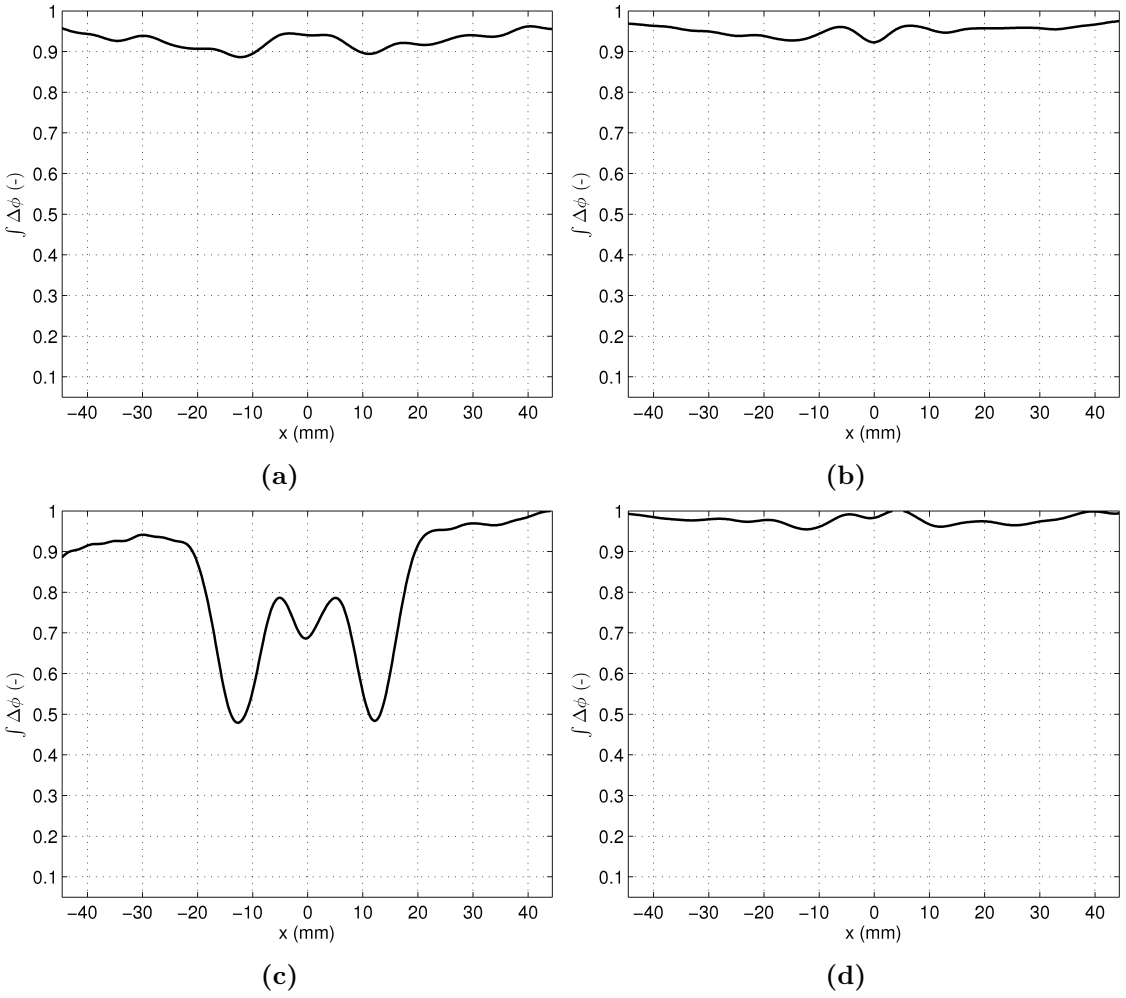

Fig. 9.31: Density distribution at $z = 10\,\text{mm}$. OP1a (a), OP1b (b), OP2a (c), OP2b (d)

A different behavior is observed at $z = 25\,\text{mm}$, shown in *Fig. 9.32*. For all operating points, except OP2a, the graph shows three peaks with the minimum value at the center axis. The distribution may be explained by the formation of the four prongs mentioned before, as seen in *Fig. 9.30*. The minima of $\int \Delta\phi$ are of the same order at all operating points. *Figure 9.32c* shows a nearly unified distribution. However, the two peaks observed in *Fig. 9.31c* are still visible and have been shifted to $x = \pm 19\,\text{mm}$.

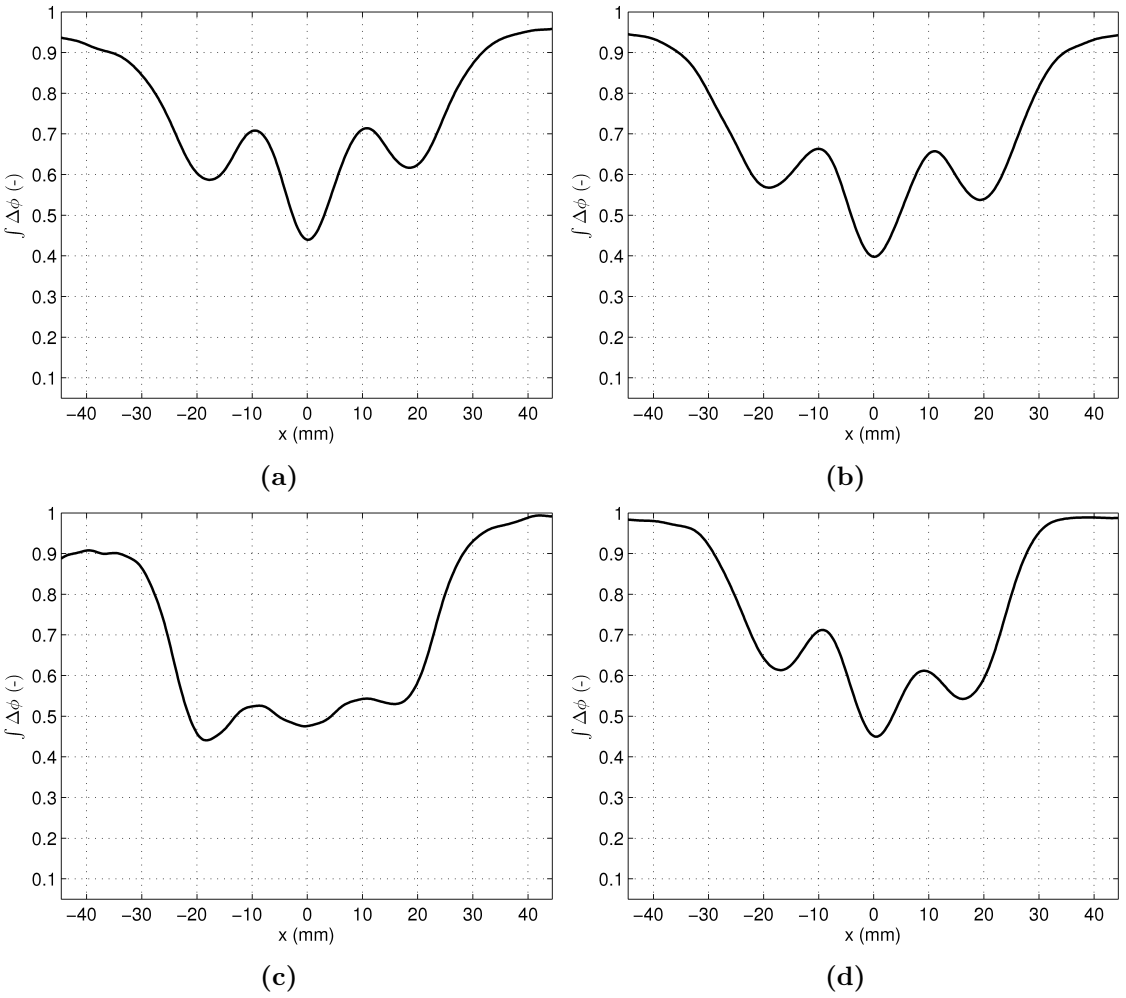

Fig. 9.32: Density distribution at $z = 25\,\text{mm}$. OP1a (a), OP1b (b), OP2a (c), OP2b (d)

When moving further downstream to $z = 35\,\text{mm}$, the distribution of density becomes more uniform, as shown in *Fig. 9.33*. This may be mainly related to the mixing process and the heat transfer. It is also observed that the zones of low density broaden. At this height no big differences between the operating points can be identified, except for the width of the low-density region. The minima for OP1b are around $x = \pm 24\,\text{mm}$ and for OP2b around $x = \pm 17\,\text{mm}$.

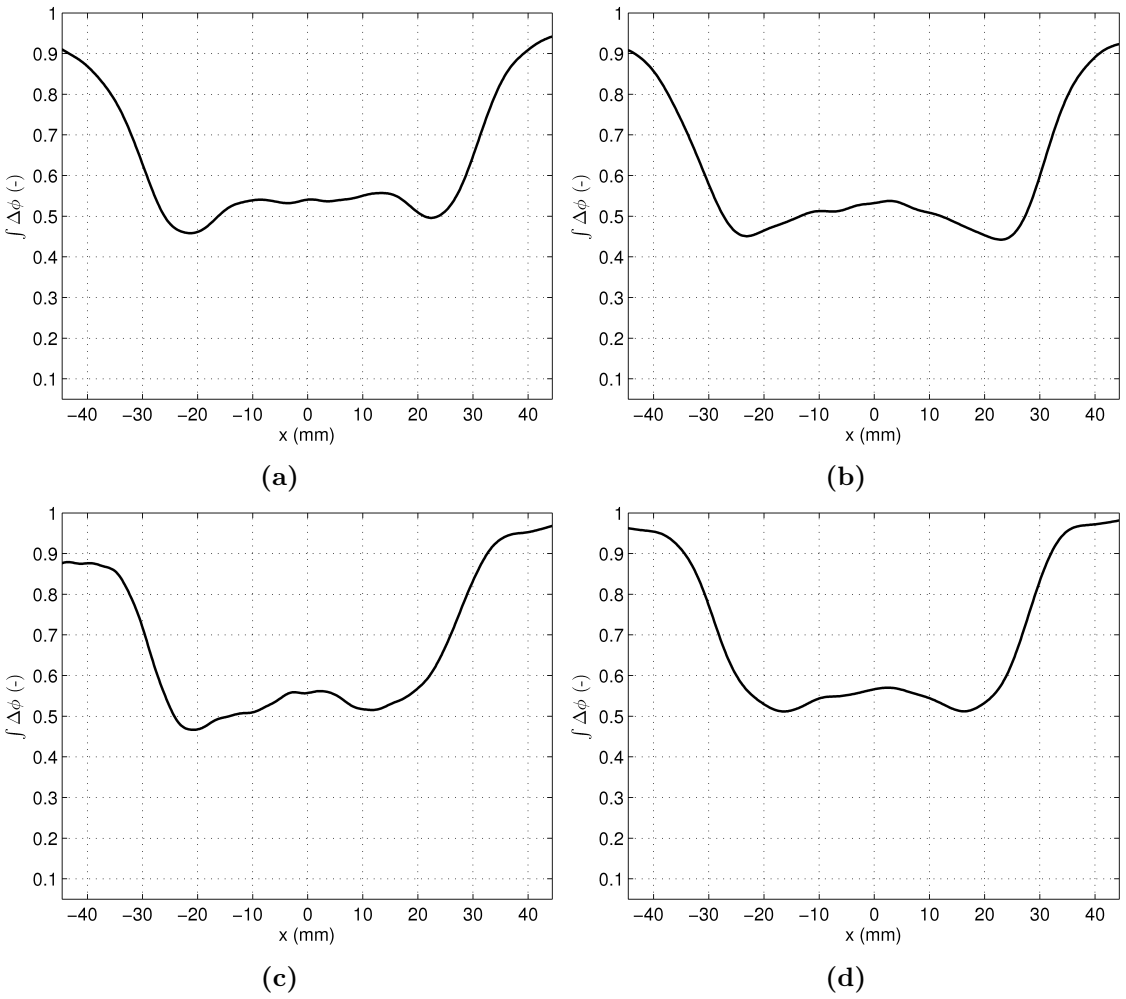

Fig. 9.33: Density distribution at $z = 35\,\text{mm}$. OP1a (a), OP1b (b), OP2a (c), OP2b (d)

9.15 Density fluctuations

Figure 9.34 qualitatively illustrates local density fluctuations at different operating points. The results were obtained by applying the dual laser interferometric vibrometry, as explained in *Sec. 5.4.3*. For that the burner was traversed from $x = -40$ to $x = 40$ in steps of 2.5 mm at $y = 0$ and at three different heights z, namely 10, 25 and 35 mm.

Shown are graphs of σ, which is the square root of the magnitude of the power spectrum $C(f)$ obtained by correlating the two LV signals (*Eq. (9.3)*).

$$\sigma = \sqrt{C(f)} \tag{9.3}$$

Mathematically it is the standard deviation in kg/m^2 as the weighting with the effective measurement area $A_c(f)$ has not been performed. A feasible method for determining $A_c(f)$ is given in *Sec. D*. Sampling rate of the LV has been 16 384 Hz, the velocity range was set to 5 mm/s/V and the Gladstone-Dale constant was assumed to be $2.52 \cdot 10^{-4}\,\text{m}^3/\text{kg}$. The filter width $\Delta\varphi(f)$, used to reduce the influence of sound waves and correlated vortical structures, was set to 1 rad.

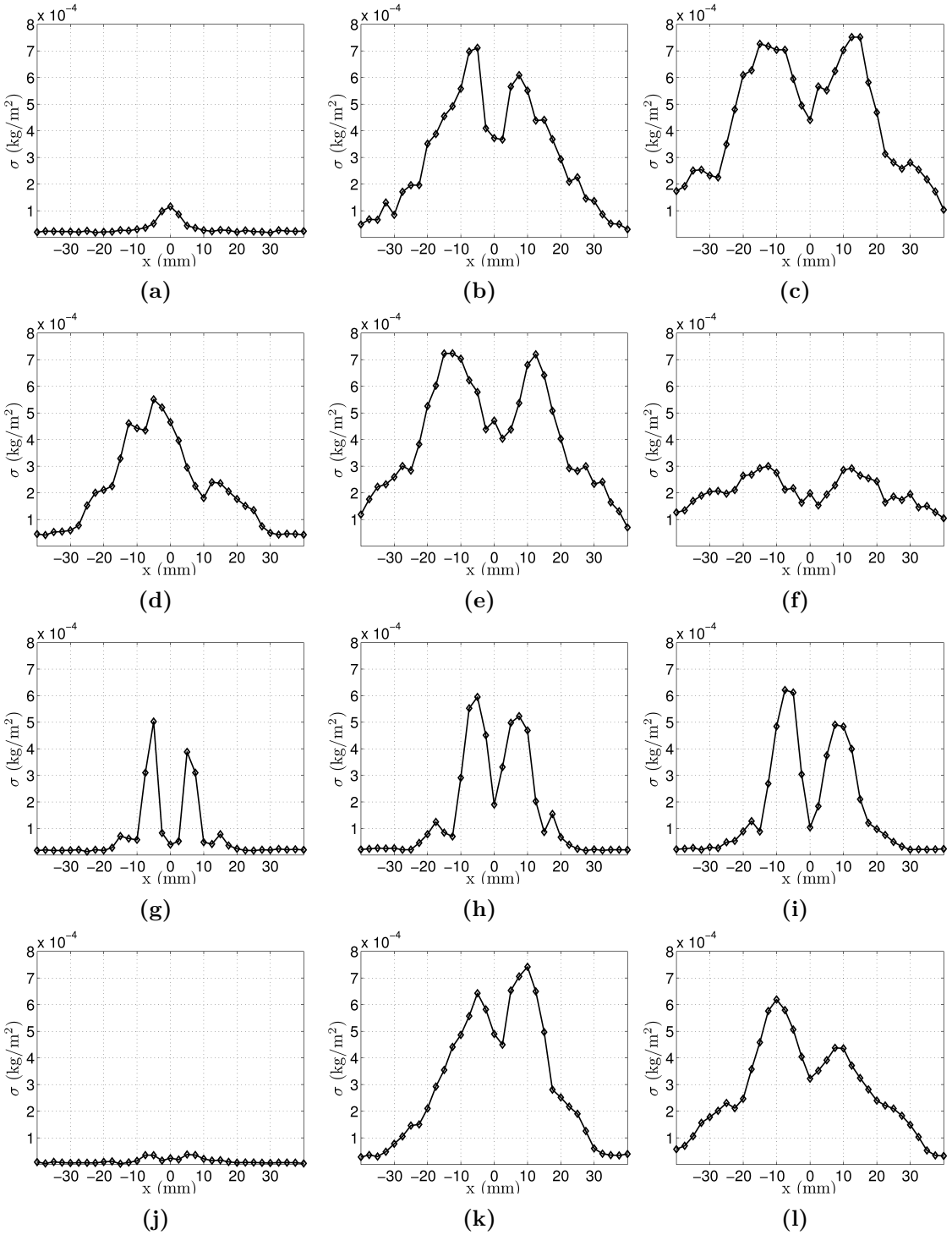

Fig. 9.34: Local density fluctuations along the x-axis. OP1a: $z = 10\,\text{mm}$ (a), $z = 25\,\text{mm}$ (b), $z = 35\,\text{mm}$ (c). OP1b: $z = 10\,\text{mm}$ (d), $z = 25\,\text{mm}$ (e), $z = 35\,\text{mm}$ (f). OP2a: $z = 10\,\text{mm}$ (g), $z = 25\,\text{mm}$ (h), $z = 35\,\text{mm}$ (i). OP2b: $z = 10\,\text{mm}$ (j), $z = 25\,\text{mm}$ (k), $z = 35\,\text{mm}$ (l)

Figure 9.34a - *Fig. 9.34c* show the results for OP1a at three different heights z. At $z = 10\,\text{mm}$ hardly any density fluctuations are observed, except for the area near the central burner axis. At $z = 25\,\text{mm}$ and $z = 35\,\text{mm}$ strong fluctuations are detected with two

distinctive peaks. Due to the wider reaction zone at larger heights z, the peaks shift radially by approximately 4 mm, as can be seen in *Fig. 9.34b* and *Fig. 9.34c*.

As the flame stabilizes approximately 11 mm downstream of the head-plate, strong fluctuations are observed at $z = 10$ mm at OP1b (*Fig. 9.34d*) due to the movements of the flame base. At $z = 25$ mm two peaks are detected which are slightly wider than in the corresponding figure at OP1a (*Fig. 9.34b*). However, at $z = 35$ mm (*Fig. 9.34f*) again two peaks are observed but at a magnitude which is nearly 55 % less than that at $z = 25$ mm.

For the attached flame, the graphs for all heights z show a similar shape, only the magnitude varies by 16 % depending on the axial measurement position (*Fig. 9.34g* to *Fig. 9.34i*). Two peaks are observed which can be related to the tubular shape of the flame. At OP2b (*Fig. 9.34j* to *Fig. 9.34l*) a similar behavior compared to OP1a can be observed. At $z = 10$ mm hardly any fluctuations can be seen, except for the area around the burner central axis. At $z = 25$ mm two peaks are visible of the same magnitude detected at OP1a. At $z = 35$ mm two peaks can be seen as well, however, of lower magnitude compared to $z = 25$ mm.

According to previously published works ([42, 106]), density fluctuations may serve as an marker for the onset of combustion oscillations. These oscillations are located in the low-frequency range with a high sound pressure level and are often recognized as screeching or humming. At all operating points investigated, the flame was burning stable and the fluctuations of density are of the same order of magnitude and can be related to the natural turbulence of the flame.

Chapter 10

Control

In recent times progress has been made not only in controller technology but also actuation and sensing systems have been improved. Adaptive control strategies applying frequency tracking Kalman filters [107], IIR-filters (infinite impulse response) with LMS (Least Mean Squares) algorithms [108] or stable adaptive controllers, denoted self-tuning regulators (STR) [109] have been investigated which adjust the control parameters depending on the operating state. This should ensure robust control throughout the operational envelope while relying as little as possible on a particular control model.

However, the most critical part in control technology is the actuation system as it sets the upper limit of the performance benefit. In addition to well known actuators like acoustic devices, mass- and heat flux modulation devices, and moving surfaces or boundaries, micro-electro-mechanical-system (MEMS) actuators are rapidly emerging. They entail potential for noticeable changes, such as spatially distributed control, less intrusive, more robust, and low costs, although currently the actuation authority and hostile environment operation are limited [110].

Points to consider:

- In order to control the variable geometry burner, the whole operational envelope has to be characterized experimentally. Due to the multiplicity of parameters (tangential air split, exit area, inlet flow rates for air and fuel, flame shape and position) this task is time-consuming.
- Flame behavior and transitions are depending on the direction of a certain parameter variation, hence of the hysteresis behavior, as mentioned in *Sec. 9.9*. Although, the behavior of the flame is reproducible, there are many paths of operation that are to be investigated experimentally before selecting optimum operation curves.
- An important issue of this technology is the need for a failsafe mode. The mechanism of the actuators which drives the air split or varies the exit nozzle area has to be simple and must override all controls in case of an incident, for instance, a repeal spring forcing the actuator back to a default position in case of power loss.
- The parameters of relevance do not necessarily show the same sensitivity. For instance, it was observed, that for a certain operating point variation the change of air split is rather small compared to the change of exit nozzle area change (*Tab. 8.3*).
- In terms of input parameters for control purposes, integral light emission measurements with the help of cameras, might be an eligible technology as the technical effort can be kept low and processing may be possible in real time. For instance, the position of the flame as well as its shape in combination with conventional measurement techniques like pressure and temperature probes can produce instant feedback.

Laser optical measurement techniques like LIV do provide useful data on the state of the burner, however, information is delivered in a time-consuming post-processing step.

Chapter 11

Summary and outlook

The main objective of this work was to investigate a novel variable geometry burner concept in terms of broadening the operating range. At design conditions the burner produces a compact aerodynamically swirl-stabilized flame. Two parameters at the injection can be adjusted steplessly and independently, namely the swirl strength of the fluid and the injector exit nozzle area. This technology was found useful, as new low-emission aircraft engine concepts may vary the air mass flow drastically, in the order of 30 % compared to a default operating point. As a result, conventional combustion may undergo some difficulties like flame transition, flash back or even flame blow-off.

In a first step a literature study was performed to gain knowledge on variable geometry in gas turbine combustion technology. Therefore, technical papers, books, reports and patents have been scanned and summarized. After that it was agreed on the type of burner to be realized and on the variable geometry parameters to control. Most of the applications found, focus on the air flow control within the combustion chamber, for instance, controlling the air distribution between primary and secondary zone. However, here the interest was put on the injection system, namely altering the swirl strength of the fluid and varying the exit nozzle area of the injector. The swirl strength was altered by controlling the ratio of tangential to axial air while keeping the overall mass flow rate constant. The injector exit nozzle area was changed by moving a bluff body axially back and forth.

For the validation process of the burner several experiments had to be carried out. However, measurements in reacting flows, or more specifically in flames, are always critical as mechanical probes are exposed to heat and heat release fluctuations. Due to the intrusive nature of the measurement devices the flame and its dynamics are influenced and the results may not be reliable. As a consequence, non-intrusive optical and laser-based measurement techniques such as the schlieren technique, particle image velocimetry, interferometric measurement techniques, light emission measurements, and Raman spectroscopy, have been used here to investigate the behavior of the variable geometry burner. Of interest have been flame visualizations (shape, position), distributions and visualizations of density gradients, density fluctuations, combustion aerodynamics, and distributions of temperature. The techniques used and the principles that lie behind have been presented.

Prior to realizing the variable geometry burner, a numerical analysis of a well known burner was performed. The question which was assessed, was if it is possible to obtain a similar flow field, compared to a default operating point, with the help of variable geometry, when operating conditions have changed. For the analysis, the investigations focused on the aerodynamics (flow field) of the primary combustion zone, in absence of cooling. Furthermore, the feedback of combustion on the injection was not taken into account. The parameters which were altered in the frame of this analysis were the strength of swirl, the area at the injector exit nozzle, and the mass flow rate. Similarity was supposed to be achieved if the

reference velocity at the injector exit and the swirl number at $z/D = 1$ were within $\pm 5\,\%$ of the reference case values. It has been shown through the simulations, that reductions in mass flow rate alter the combustion aerodynamics, which can be nearly canceled out by changing the burner exit nozzle area and setting a different swirl strength.

After the feasibility study a model burner was realized and instrumented together with a test rig. The main aim of this work, the extension of the stable operating range with the help of variable geometry in case of a drastic variation of air mass flow rate, was demonstrated. Within an interval of approximately $-25\,\%$ of reduced mass flow variation, compared to the default operating point, combustion is sustained applying fixed geometry. Larger variations, of the order of $30\,\%$ when throttling the core mass flow in order to improve efficiency, cause a flame shape transition which can be prevented through altering swirl strength and exit nozzle area. Combustion hence remains stable within variations of reduced mass flow rates of about $-50\,\%$.

Additionally, four specific operating points have been investigated more in detail with the measurement techniques explained in *Sec. 5*. They have been chosen in order to show the effectiveness of the actuation and as they may represent possible operating points through the operational envelope of the burner. Differences between the points have been worked out and were illustrated.

For control purposes, from the results deduced, integral light emission measurements with the help of cameras, might be an eligible technology for providing useful information as the technical effort can be kept low and processing may be possible in real time. For instance, the position of the flame as well as its shape can produce instant feedback on the state of the burner.

However, with the burner investigated, it was possible to maintain a stable lifted flame on a larger operational envelope, as variable geometry offers a great potential of flexibility. This is due to additional parameters like swirl strength and exit nozzle area, which can be altered depending on the operating point. A more complex combustion control will be necessary and hence this technology has a need for a 'straightforward' design, which is robust and failsafe. If implemented in a combustion system, variable geometry may be found first in industrial gas turbines rather than in aero engines, as space and mass considerations play a major role at the latter application. For instance, a variable geometry burner could replace sequential combustion as the parameters can be set for optimal combustion during a night setback. However, at the moment further research work may be done under more realistic operating conditions.

Appendix

Appendix A

Swirl application literature

In the following a list of selected literature concerning swirl applications is given. The items are ordered by the type of swirl generation, as mentioned in *Sec. 3.1.2*.

Tab. A.1: Swirl application literature

Author	System	Scale	Comment
Aoyama and Mandai [13]	axial	full	
Li and Hales [14]		full	
Dodds and Fear [32]		full	
Gupta et al. [33]		laboratory	
Komarek and Polifke [34]		laboratory	
McManus et al. [111]		laboratory	
Russ et al. [25]	tangential	laboratory	variable swirl
Freitag et al. [26]		laboratory	generic swirler
Lucas et al. [38]		laboratory	
Krautkremer [112]		laboratory	
Albrecht et al. [113]		full	Alstom EV-10-burner
Kokanović et al. [114]		full	Alstom GT26
Chigier and Chervinsky [27]	axial/tangential	laboratory	
Vaught [55]		full	patent
Lee et al. [115]		laboratory	
Lohrmann and Büchner [116]		laboratory	generic swirler
Beér and Chigier [21]	movable block	laboratory	
Weber and Dugué [29]		laboratory	
Borman and Ragland [30]		laboratory	
Palm [31]		laboratory	
Vanoverberghe et al. [117]		laboratory	flame state transition

Appendix B

Validation of the numerical model

In order to validate the numerical model for the nozzle simulations a test case, described in [118], has been chosen. The authors performed 3d LES calculations and LDA measurements at reactive and non-reactive conditions. The chosen test case (non-reactive) was then simulated with a simplified 2d model and compared to the results of the LES calculation and the measurements. The 3d model for the LES calculations is shown in *Fig. B.1*, the 2d model for the validation simulation in *Fig. B.2*. It is important to note that the shape of the combustion chamber in the reference case is rectangular, in the validation case, however, cylindrical. In *Tab. B.1* the settings for the numerical simulations for the reference case (3d model) and the validation case (2d model) are shown. All measurements and simulations have been performed at non-reactive conditions. Inlet temperature and pressure were 463 K and 1 bar abs, respectively. The air mass flow rate was set to 15 g/s. The operating conditions are summarized in *Tab. B.2*.

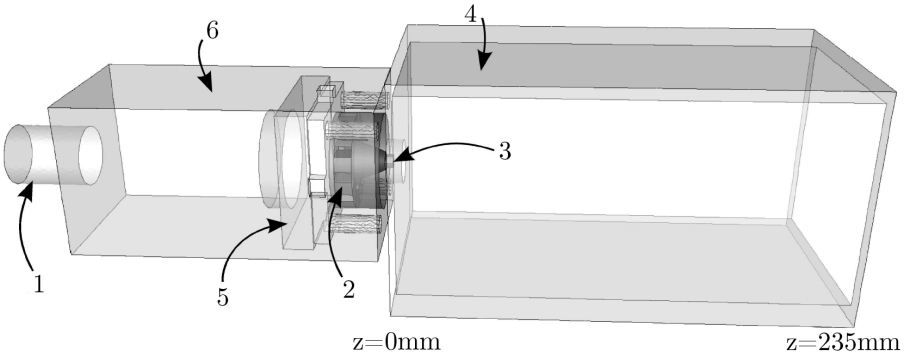

Fig. B.1: 3d model for the LES calculations [118]. Air inlet channel (1), swirler (2), fuel injection (3), combustion chamber (4), swirler holder (5), plenum (6). Flow direction is from left to right.

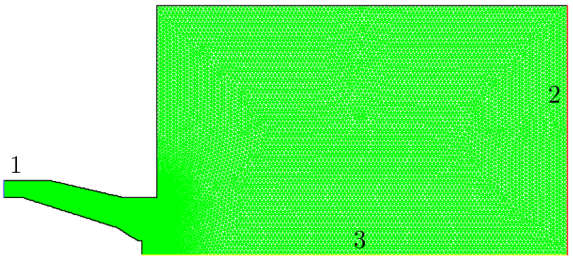

Fig. B.2: 2d model for the validation simulation. Air inlet (1), exit (2), symmetry axis (3). Flow direction is from left to right.

Tab. B.1: Settings for the numerical validation simulations

Description	3d model [118]	2d model
Number of cells	$3.5{\cdot}10^6$	25 000
Type	Tetrahedron	Tetrahedron
Type of solver	CDP, AVBP	2d axisymmetric swirl pressure based
Turbulence model	LES	standard k-ϵ

Tab. B.2: Boundary conditions for the simulations

Description	Value
Condition	non-reactive
Pressure	atmospheric
Air inlet temperature	463 K
Air mass flow rate	15 g/s

Figure B.3a and *Fig. B.3b* show the mean axial and mean tangential velocities for the reference case, respectively. Each figure shows four plots at different axial positions downstream of the headplate, where the squares denote the LDA measurements, the solid lines the CDP simulations, and the dashed lines the AVBP results. *Figure B.3c* and *Fig. B.3d* depict the mean axial and tangential velocities for the validation case, respectively. Again, each figure shows four plots at different axial positions. It has to be noted, that the simulation results for the reference case seem to underestimate the velocity maxima. This can be seen in *Fig. B.3a* at positions 56 mm and 86 mm. However, this issue was extensively discussed in [118].

Comparing the mean axial velocities for the reference and the validation case reveals good agreement of the maxima and their radial positions, especially for axial positions of 6 mm, 26 mm, and 56 mm (*Fig. B.3a* and *Fig. B.3c*). At position 86 mm the position of the calculated maxima for the validation case is shifted further outside by approximately 10 mm compared to the simulation results of the reference case, although the maximum velocity shows good agreement. In general, the velocity profiles of the reference case seem to be smoother than that obtained at the validation case. This may be due to the fact that no fillets have been modeled in the 2d case.

The largest deviations between reference and validation case are observed at the mean tangential velocities (*Fig. B.3b* and *Fig. B.3d*). However, the positions of the maxima show good agreement at axial positions 6 mm, 26 mm, and 56 mm. Again, at position 86 mm the maxima of the validation case are shifted further outside by approximately 10 mm. The velocity maxima at positions 6 mm, 26 mm, and 56 mm between the two cases differ by almost 50 %. At position 86 mm the maxima between the simulation results of the reference case and the validation case show good agreement. The results of the LDA measurements of the reference case are slightly higher. It is interesting to note, that at position 26 mm of the reference case (*Fig. B.3b*) a third positive maximum is observed, which is missing in the according plot of the validation case (*Fig. B.3d*). This difference may be a result of the finite number of inlet slots of the swirler as the additional peak is observed by

the simulations and the measurements. Further downstream, due to mixing effects, the maximum fades away.

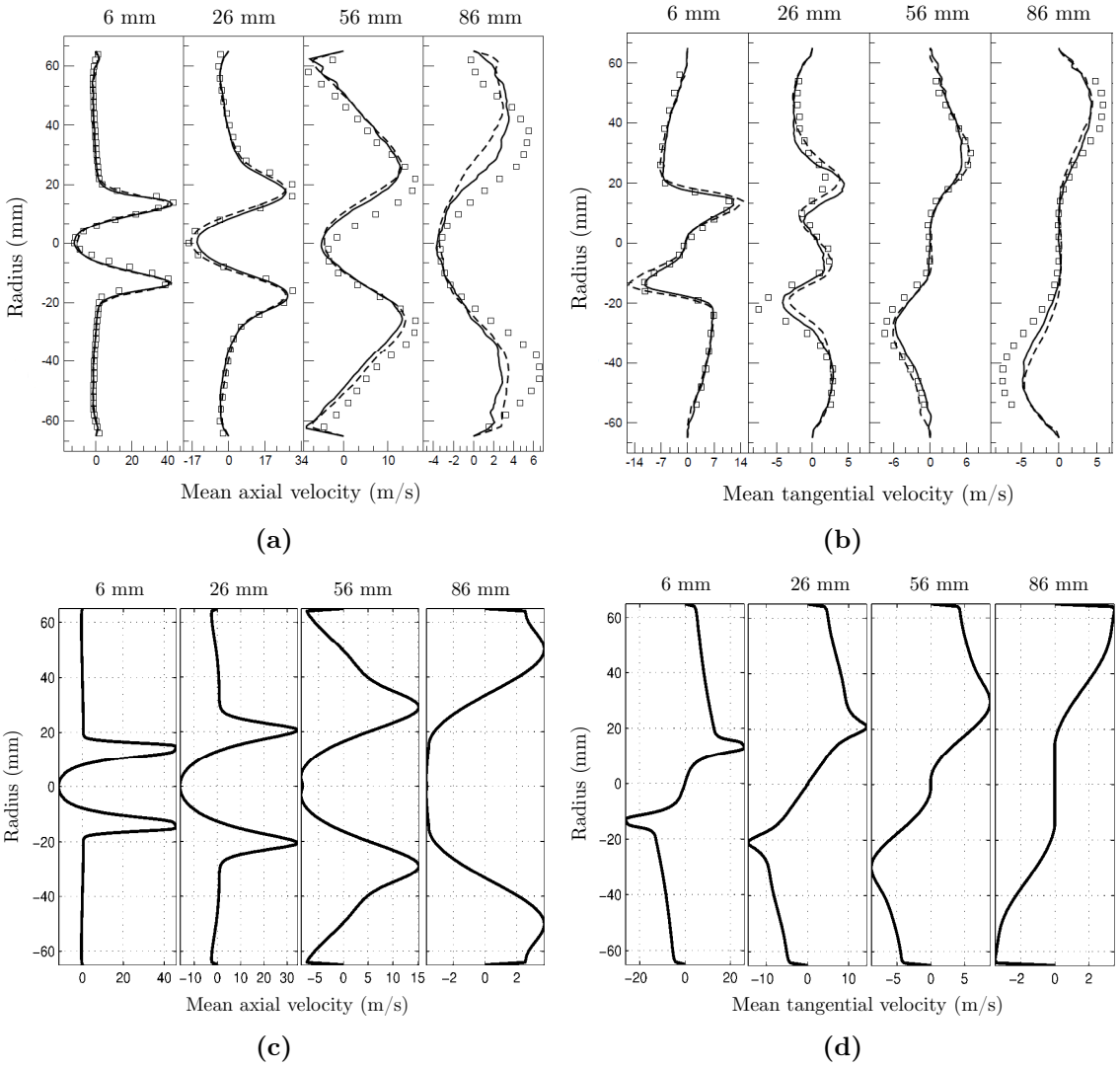

Fig. B.3: Results of the validation simulations. Mean axial velocities of the reference case (a), mean tangential velocities of the reference case (b). Squares: LDA measurements, solid lines: CDP, dashed lines: AVBP [118]. Mean axial velocities of the validation case (c), mean tangential velocities of the validation case (d).

It is assumed that the numerical model for the 2d simulations is sufficient for the needs of this work here as the dimensioning of the injector nozzle was to be done by the help of the numerical calculations and the effectiveness of the actuation was to be shown. The validation process revealed that the axial flow field of the 2d model is similar to that observed in the reference case and that the tangential velocities are overestimated in the 2d model compared to the 3d model.

Appendix C

Density fluctuations as indicator for combustion oscillations

It is assumed that density ρ is a function of pressure p and entropy s [10] but cannot be stated exactly. In order to give a mathematical expression, developments of Taylor series for $p(\rho)$ and $\rho(s)$ are used. This results in

$$p(\rho) = p(\rho_0) + (\rho - \rho_0)\,\frac{\partial p}{\partial \rho}(\rho_0) + \dots \tag{C.1}$$

and

$$\rho(s) = \rho(s_0) + (s - s_0)\,\frac{\partial \rho}{\partial s}(s_0) + \dots \tag{C.2}$$

Rearranging of *Eq. (C.1)* and *Eq. (C.2)* and neglecting terms of higher order lead to

$$p(\rho) - p(\rho_0) = (\rho - \rho_0)\,\frac{\partial p}{\partial \rho}(\rho_0) \tag{C.3}$$

and

$$\rho(s) - \rho(s_0) = (s - s_0)\,\frac{\partial \rho}{\partial s}(s_0) \tag{C.4}$$

Combining *Eq. (C.3)* and *Eq. (C.4)* and substituting $p(\rho) - p(\rho_0)$ by p' and $(\rho - \rho_0)$ by ρ' in *Eq. (C.3)* and $\rho(s) - \rho(s_0)$ by ρ' and $(s - s_0)$ by s' in *Eq. (C.4)*, the density fluctuations can be expressed as

$$\rho' = \left.\frac{\partial \rho}{\partial p}\right|_s p' + \left.\frac{\partial \rho}{\partial s}\right|_p s' \tag{C.5}$$

where ρ', p' and s' denote as the fluctuating parts of density, pressure and entropy, respectively. The partial derivation of density with respect to pressure can be written as $1/c_0^2$ and the derivation of density with respect to entropy equals $-\rho_0/c_p$, where c_0 denotes as the local speed of sound and c_p as the specific heat capacity at constant pressure. Substituting the partial derivatives in *Eq. (C.5)* with the expressions stated before leads to

$$\rho' = \frac{1}{c_0^2}\,p' - \frac{\rho_0}{c_p}\,s' \tag{C.6}$$

Taking the time derivative of *Eq. (C.6)* and replacing s' by q'/T_0 (neglecting viscous effects and assuming that the fluctuations of entropy are caused by perturbations of heat release [119, 120]) results in

$$\frac{\partial \rho'}{\partial t} = \frac{1}{c_0^2}\,\frac{\partial p'}{\partial t} - \frac{\rho_0}{c_p\,T_0}\,\dot{q}' \tag{C.7}$$

where $\dot{q}'$ denotes as the fluctuating part of the specific heat per unit mass and second. Substituting $(\rho_0\,\dot{q}')$ by $\dot{q}'_v$ and knowing that $c_p = R\,\gamma/(\gamma-1)$ and $c_0^2 = \gamma\,R\,T_0$ gives

$$\frac{\partial \rho'}{\partial t} = \frac{1}{c_0^2}\frac{\partial p'}{\partial t} - \frac{\gamma-1}{c_0^2}\,\dot{q}'_v \tag{C.8}$$

where $\dot{q}'_v$ denotes as the heat release rate per unit volume and γ as the ratio of specific heat capacities. *Equation (C.8)* is equivalent to the equations stated in [42] and [119]. The first term on the right hand side of *Eq. (C.8)* accounts for density fluctuations due to acoustic pressure changes and the second term for density fluctuations due to changes of heat release. As will be shown later, the contribution of heat release in flames is much greater than that of acoustic pressure. Thus, *Eq. (C.8)* can be rewritten as

$$\frac{\partial \rho'}{\partial t} = -\frac{\gamma-1}{c_0^2}\,\dot{q}'_v \tag{C.9}$$

Taking the integral over the flame volume V_F gives

$$\int_{V_F} \frac{\partial \rho'}{\partial t}\,dV = -\frac{\gamma-1}{c_0^2}\,\dot{Q}' \tag{C.10}$$

where $\dot{Q}'$ denotes as the heat release rate of the flame. The left hand side of *Eq. (C.10)* can be directly measured by a laser vibrometer in the velocity mode – see *Eq. (5.12)* – and thus, an estimation of the heat release rate can be given. Further information can be found in [121], where this method was applied on a pulsated flame.

Appendix D

Determining the effective measurement area $Ac(f)$

In order to calculate local power spectra of density fluctuations $\overline{|F(x_0, y_0, f)|^2}$ ($\mathrm{kg^2/m^6}$), the cross spectra $\overline{|C(x_0, y_0, f)|}$ ($\mathrm{kg^2/m^4}$) have to be corrected by an effective measurement area $A_c(f)$ ($\mathrm{m^2}$), as shown in *Eq. (D.1)*, where x_0 and y_0 denote the coordinates and f the frequency.

$$\overline{|F(x_0, y_0, f)|^2} = \frac{\overline{|C(x_0, y_0, f)|}}{A_c(f)} \tag{D.1}$$

The evaluation used here requires tomographic reconstruction of integral data obtained through a single LV. The technique was already successfully applied in [106]. A different approach based on local pressure measurements was shown in [122].

D.1 Obtaining local frequency resolved data from one laser vibrometer

In the following the steps necessary to obtain local data are listed:

1. Collect and sort time signals $U(t)$ of one laser vibrometer, which has been traversed in radial direction perpendicular to the line of sight.

2. Multiply the time signals $U(t)$ with k/G to obtain $\int_z \dot{\rho}'\, dz$, where k is the vibrometer calibration factor in $m/s/V$, G the Gladstone-Dale constant in $\mathrm{m^3/kg}$ and z the coordinate in the line of sight.

3. Perform a FFT of $\int_z \dot{\rho}'\, dz$ obtained at the different radial measurement positions. This was done in Matlab R2009b. Note that in Matlab the amplitude is calculated as $2\,|\mathrm{fft}(\int_z \dot{\rho}'\, dz)|/\text{bin-size}$, where bin-size is the number of points in a portion of the time signal (necessary for averaging the spectra).

4. Create a vector with the amplitudes at a specific frequency at all radial positions. Export this data into an ASCII-file, which can be opened by IDEA (software program for digital fringe evaluation [85]). Take care that at the borders the amplitudes are zero, which is important for the next step (if necessary extrapolate). In radial direction approximately 200 points should be available (if necessary interpolate). This step has to be done for each frequency of interest.

5. Perform the tomographic reconstruction in IDEA. Here, the Abel Inversion (Radial Data - ART) applying 200 projections has been used. Save the result as '1D Raw ASCII Data' (*.asc). This step has to be done for each frequency of interest.
6. With Matlab these files can be opened and visualized. For calculating $A_c(f)$ the local data have to be squared to obtain power spectra of density fluctuations $\overline{|F(x_0, y_0, f)|^2}$.

D.2 Calculating the effective measurement area

The effective measurement area $A_c(f)$ is calculated according to *Eq. (D.2)* by rearranging *Eq. (D.1)*. For obtaining *Fig. D.1*, $A_c(f)$ has been calculated at seven different frequencies, namely 80, 110, 250, 500, 1500, 4000 and 8000 Hz.

$$A_c(f) = \frac{\overline{|C(x_0, y_0, f)|}}{\overline{|F(x_0, y_0, f)|^2}} \tag{D.2}$$

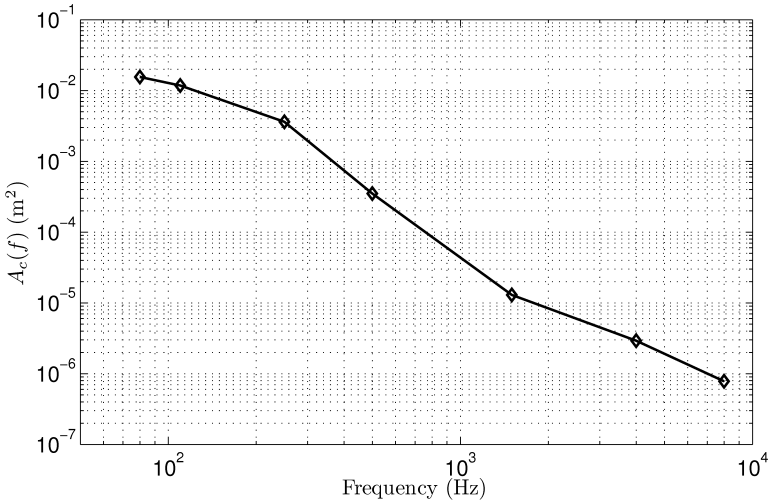

Fig. D.1: Effective measurement area

Appendix E

Emissions

When using hydrocarbons (C_xH_y) as fuel ideally carbon dioxide and water vapor are produced. The combustion mechanism can be stated as follows:

$$C_xH_y + (x + y/2)\, O_2 + z\, N_2 \longleftrightarrow z\, N_2 + x\, CO_2 + y/2\, H_2O + H_u \tag{E.1}$$

Although carbon dioxide is mainly considered as a pollutant it is a product of the complete combustion process when using hydrocarbons. It can only be reduced by improving the efficiency of the combustion process or by using a different fuel, e.g. hydrogen. New power plant cycles focus on CO_2-capture by using just oxygen as fuel. These are so-called oxyfuel cycles, for instance the Graz cycle [123]. Recently, also water is considered as pollutant when emitted in the upper atmosphere as it intensifies the greenhouse effect.

During the combustion process always unwanted products are produced. These are carbon monoxide, nitrogen oxide, nitrogen dioxide, unburned hydrocarbons, sulfur dioxide, and soot. Modern hydrocarbons include less than 0.1% sulfur which means that the amount of sulfur dioxide is negligible. Thus, the mechanism can be qualitatively written as:

$$C_xH_y + O_2 + N_2 \longleftrightarrow CO_2 + H_2O + CO + NO + NO_2 + \text{UHC} + \text{Soot} \tag{E.2}$$

In the following sections the most important pollutants will be described. A summary of the effects of the emissions on the environment are shown in *Tab. E.1* [124].

E.1 Carbon dioxide (CO_2)

Carbon dioxide is a product of the complete combustion using hydrocarbons (*Eq. (E.2)*). It is a colorless and odorless gas which is also produced through biological processes. Its concentration in the atmosphere of around 340 ppm is increased by 1 ppm by combustion processes annually. At concentrations higher than 20 000 ppm it may cause head ache. CO_2 blocks the heat radiation of the Earth and thus has a major impact on the greenhouse effect.

E.2 Nitric oxides (NO_x)

Nitrogen monoxide (NO) and nitrogen dioxide (NO_2) are commonly known as nitric oxides. NO is a colorless and odorless gas whereas NO_2 is a red-brownish to violet gas which smells similar to ozone. Mainly, 95 % of the whole nitric oxides formation is nitrogen monoxide the remaining 5 % is nitrogen dioxide. Starting from 10 ppm nitrogen

Tab. E.1: Effects of the pollutants

Pollutant	Effect
Carbon monoxide CO	toxic
Carbon dioxide CO_2	greenhouse effect
Nitric oxides NO, NO_2	toxic
	reduction of ozone in the stratosphere
	photochemical reaction to ozone in the troposphere
Unburned hydrocarbons UHC	photochemical reaction to ozone in the troposphere
	carcinogen
	smog
Sulfur dioxide SO_2	smog
Water vapor H_2O	greenhouse effect when emitted in upper atmosphere
Soot	carcinogen
	smog
	influence on visibility

dioxide shows toxic behavior. The problem with nitric oxides are their effect on ozone (O_3) depending on the height of emission. Near ground nitric oxides are responsible for ozone production (*Eq. (E.3)* and *Eq. (E.4)*) which in turn is responsible for generating photochemical smog as indicated by *Eq. (E.5)* and *Eq. (E.6)*. In the troposphere (9-13 km) O_3 acts as a greenhouse gas and within the stratosphere (17-23 km) nitric oxides are reducing the ozone layer of the Earth, as can be seen in *Eq. (E.7)*, where NO acts as a catalyst, and *Eq. (E.8)*.

$$NO_2 \xrightarrow{\text{UV, } \lambda < 420\,\text{nm}} NO + O^* \tag{E.3}$$

$$O_2 + O^* \longrightarrow O_3 \tag{E.4}$$

$$O_3 \xrightarrow{\text{UV}} O_2 + O^* \tag{E.5}$$

$$C_xH_y + O^* \longrightarrow \text{Aldehydes, Ketones} \tag{E.6}$$

$$NO + O_3 \longrightarrow NO_2 + O_2 \tag{E.7}$$

$$NO_2 + O^* \longrightarrow NO + O_2 \tag{E.8}$$

In the literature mainly five mechanisms are mentioned which produce nitrates [10]. These are thermal NO, prompt NO, fuel NO, through NNH produced NO, and NO_x generated through dinitrogen monoxide N_2O (laughing gas). *Fig. E.1* shows the regions of NO formation for each mechanism with respect to the equivalence ratio ϕ. The mechanisms will be described more into detail in the following sections.

E.2.1 Thermal NO

Thermal NO is being generated in hot zones with temperatures above 1800 K as *Eq. (E.9)* requires a high activation energy due to the stable nitrogen which is supplied by the

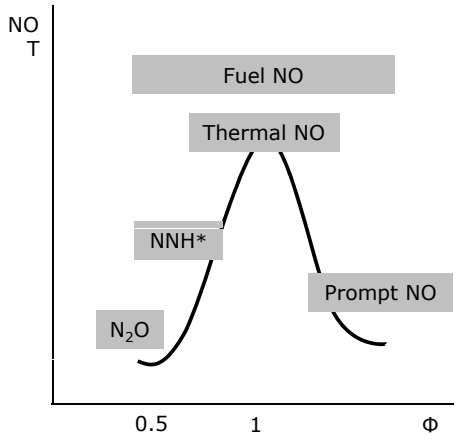

Fig. E.1: *NO* production mechanisms [10]

combustion air. According to Zeldovich the mechanism can be described as follows [125]:

$$O^* + N_2 \overset{k_1}{\longleftrightarrow} NO + N^* \tag{E.9}$$

$$N^* + O_2 \overset{k_2}{\longleftrightarrow} NO + O^* \tag{E.10}$$

$$N^* + OH \overset{k_3}{\longleftrightarrow} NO + H^* \tag{E.11}$$

The velocity-constants k_1–k_3 have to be found experimentally. However, different values are stated in the literature. A comprehensive summary can be found in [126]. What is common is, that k_1 is slower than the other two by several orders of magnitude. Thermal NO formation rises exponentially with temperature and strongly depends on residence time in the reaction zone. Doubling the temperature rises the formation rate by the factor 10^3, a rise from 2000 to 2500 K increases the rate at least by 50 [126]. The so-called Zeldovich mechanism is responsible for the major part of NO production at temperatures above 1900 K. In order to keep the NO formation rate low following aspects have to be considered:

Fuel conditioning A homogeneous mixture of fuel and air has to be provided which means sufficient mixing and evaporation.

Temperatures Avoid stoichiometric conditions in the primary zone, hence lean combustion. Keep combustor entry temperature low.

Oxygen concentration At zones of higher temperatures provide rich conditions.

Residence time At zones of higher temperatures reduce residence time, thus realize shorter flametubes.

E.2.2 Prompt *NO*

The formation of prompt NO is far more complex as the one of thermal NO. It strongly depends on the presence of the CH-radical, which can react in many ways. Prompt NO was firstly described by Fenimore, hence the name Fenimore NO. The formation mechanism can be stated in the following way:

$$CH^* + N_2 \longrightarrow \mathrm{HCN} + N \rightarrow \cdots \rightarrow NO \tag{E.12}$$

In the main step the CH-radical and N_2 react to HCN and through different steps finally to nitrogen monoxide as shown in *Eq. (E.12)*. The source of nitrogen is mainly combustion air. Prompt NO is mainly produced at stoichiometric and rich flames. However, it is also produced at low temperatures and lean conditions although at noticeable lower rates. As the timescale of production is much faster than the timescale for mixing residence time has hardly an effect on formation. At temperatures below 1870 K prompt NO is the prevailing mechanism for generating nitrogen monoxide [127].

E.2.3 Fuel NO

This type of NO is generated from nitrogen contained by the fuel. Fuel NO is generated at temperatures as low as 900 K. Due to the high-quality of fuels for gasturbines the emissions produced are negligible.

E.2.4 NNH^*

The NNH-radical is being generated as a result of the reaction of nitrogen and hydrogen. The radical can then be oxidized through *Eq. (E.13)*. At lean and premixed conditions two NO molecules are build as a last step.

$$NNH^* + O \longrightarrow NO + NH \tag{E.13}$$

E.2.5 Dinitrogen monoxide N_2O

At low temperatures and lean conditions NO can be generated through oxidation of N_2O. To start the reaction an inert diluent M is necessary. The mechanism can be written as follows:

$$N_2 + O + M \longrightarrow N_2O + M \tag{E.14}$$
$$N_2O + O \longrightarrow NO + NO \tag{E.15}$$

Dinitrogen monoxide is the main source for nitrates formation at lean premixed conditions as the mechanism favors higher pressures and low temperatures.

E.3 Carbon monoxide (CO)

Carbon monoxide is an intermediate product of combusting hydrocarbons. It is a colorless, odorless and tasteless gas which provokes rapid suffocation as it fixes on hemoglobin (200 to 300 times more than O_2) preventing it to transport oxygen. The main factors for carbon monoxide production, as mentioned in [128], are firstly inadequate burning rates in the primary zone due to a high AFR and an insufficient residence time. Secondly, inadequate mixing of fuel and air which produces lean regions where CO production is enhanced, and finally quenching the flame too fast and thus freezing the combustion process before CO could be oxidized to CO_2.

CO is produced fast according to *Eq. (E.16)*. The oxidation to CO_2 according to *Eq. (E.17)* is slower and requires temperatures above 1200 K and the presence of oxygen.

$$C_xH_y + O_2 \longleftrightarrow CO + OH \tag{E.16}$$
$$CO + OH \longleftrightarrow CO_2 + H_2O \tag{E.17}$$

E.4 Unburned hydrocarbons (UHC)

Unburned hydrocarbons are fuel vapors and cracked components of fuels. They are produced through incomplete combustion at low temperatures (idle, part load). Local lack of oxygen and too short residence times in the flame front (e.g. at combustion instabilities) also generate high amounts of UHC. At concentrations starting from 0.05 ppm hydrocarbons can be recognized through their smell. Two types exist – aliphatic and aromatic hydrocarbons. Although there are no known lethal effects of aliphatic hydrocarbons aromatic (Aldehydes, Benzol) ones (also known as polycyclic aromatic hydro carbons, PAH) are carcinogen even at concentrations as low as 1 ppm. Those PAH are predecessors of soot [10]. Emitted hydrocarbons are responsible for generating smog.

Reduction of UHC can be achieved firstly, when the hot gases in the reaction zone are not disturbed by cold gas streams or walls, secondly, through a well stabilized flame, thirdly, due to better oxidation at higher temperatures and pressures, and finally by applying sufficient residence time [129].

E.5 Soot

Soot is a visible, black aerosol smelling like hydrocarbons, which consists of fine particles (0.05 μm). It is generated at temperatures between 1200 and 1600 K at rich conditions due to incomplete combustion in the primary zone and shows carcinogen behavior. Soot generation is enhanced by the presence of PAH and by rough sprays. Increasing the operating pressure shifts the rich blow out limit to higher values of the equivalence ratio ϕ which has an amplifying effect on soot production. A high soot concentration increases the heat radiation which puts additional stress on the liner walls. Fuels with a higher condensing point (Kerosene, Diesel) tend to produce more soot than fuels with a lower one (Gasoline).

Soot is reduced by the oxygen of the mixing air in the secondary zone and by simultaneously providing sufficient residence times. Moreover, modern injection systems prefer air-blast atomizers than pressure atomizers as the first provide enhanced mixing which mitigates soot generation [127].

Appendix F

Emission reduction

Considering *Chap. E*, it is obvious that a zero emission technology based on state of the art combustion technology is not yet possible. Due to the different formation mechanisms of the pollutants measures which would reduce for instance carbon monoxide amplify the emission of nitrates. Therefore, a compromise has to be found which keeps the temperatures in a narrow band in order to minimize both carbon monoxide and nitrates as well as UHC and soot formation. *Figure F.1* depicts the emission production situation with respect to temperature and equivalence ratio [10].

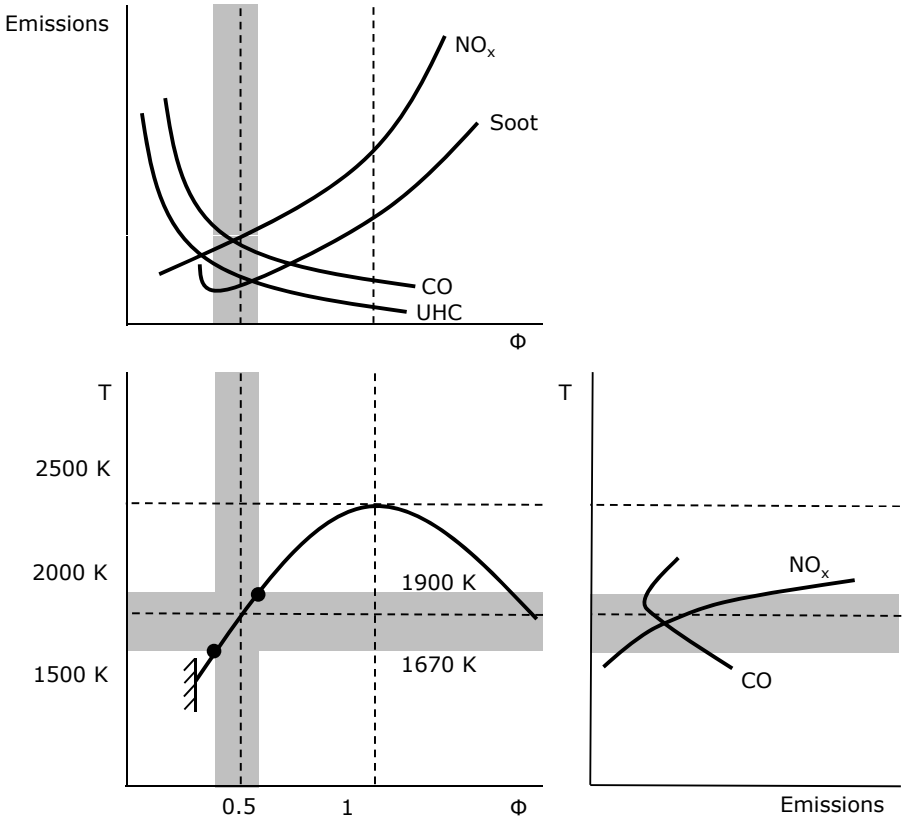

Fig. F.1: The upper left part of the figure depicts the emission formation due to the equivalence ratio ϕ. The lower right due to temperature. The lower left shows the shift in temperature in the reaction zone with respect to the equivalence ratio.

Important parameters effecting the emission formation of gas turbine combustors, as already mentioned above, are the primary zone temperature, the equivalence ratio, the

residence time, the cooling of the flametube, and the mixing zone characteristics. In order to improve the efficiency η combustion chamber inlet temperatures and pressures are continuously rising. Hence, higher flame temperatures are achieved. This inherits higher NO_x levels. What is more, due to the higher temperature of the compressed air cooling is worsened.

Tab. F.1: Measures for emission reduction [128]

Species	Measure
UHC & CO	Improve atomization and enhance mixing (air-blast)
	Air injection in the primary zone ($\phi \simeq 0.7$)
	Increase primary zone volume or residence time (swirl-stabilized)
	Reduce film-cooling air
	Reduce air flow at idle to augment ϕ
	Staged combustion
NO_x	Reduce flame temperature through lean combustion
	Reduce flame temperature through rich combustion
	Homogeneous combustion
	Establish compact flame (short residence time)
	Injection of demineralized water

F.1 Primary measures

F.1.1 Staged combustion

The main problem of lean combustion technology is its susceptibility to flashback, flameout and combustion oscillations. This can be mitigated by stabilizing the lean main zone throughout the operating range of the engine by applying a pilot stage [10]. Due to the additional reaction zone two operating points can be optimized in terms of resident time and stoichiometry. However, the rich operated pilot stage produces higher NO_x emissions but stabilizes the lean main zone via its hot gases. The higher temperatures of the pilot gases are also beneficial in terms of CO and UHC reduction. Emissions are drastically reduced compared to conventional combustion systems through the shortened resident time in the combustion chamber and enhanced mixing technology such as lean premixed prevaporized (LPP) modules or twin annular premixing swirlers (TAPS). In terms of design two concepts are possible – axial and radial staged combustion. Disadvantageous of staged combustion are the tuning between the pilot and main stage and the complexity of the design of the combustion chamber.

F.2 Combustion management

State of the art emission reduction is performed through an enhanced combustion management. These are, for instance lean combustion or reduction of flame temperature. As these technologies require a different geometry existing designs can hardly be modified. Modifications are directly affecting the combustion chamber and are therefore known as

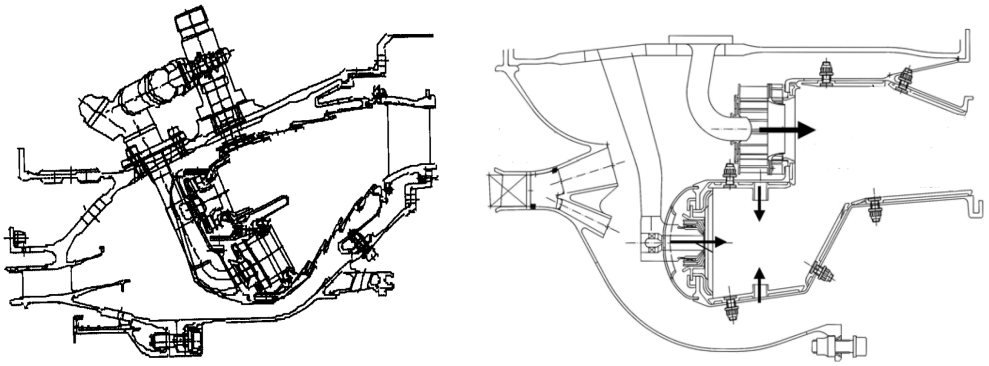

(a) (b)

Fig. F.2: Staged combustion designs. Radial staged combustion chamber of the CFM 56 [130] (a), axial staged combustion chamber with LPP modules [10] (b). Arrows are indicating flow paths.

primary measures. What is common for most of the new technologies is that they require a high quality premixing of fuel and combustion air.

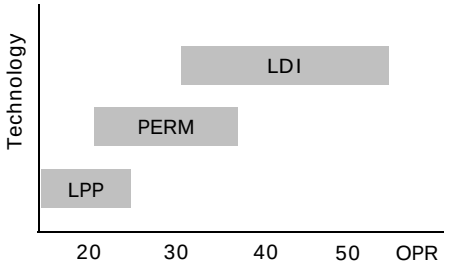

Fig. F.3: Combustion technology

F.2.1 Dry low emission

Dry low emission (DLE) technology is used with gaseous fuels which are premixed with air (without addition of water). Combustion takes place in the lean regime at comparatively low temperatures which mitigates the NO_x emissions (*Fig. F.4*). This technology is mainly applied at stationary gas turbines.

F.2.2 Lean premixed prevaporized

Lean premixed prevaporized (LPP) combustion is applied to liquid fuels and operates in the lean regime. Firstly, the fuel is atomized by an inner air flow, afterwards mixing and evaporation is performed by outer air flows which may be co- or counter rotating. Auto-ignition and flashback constraints apply, as in the premixing tube a combustible mixture is produced, which makes this technology only suitable for low overall pressure ratio (OPR) operating conditions. Furthermore, this technology is susceptible to combustion oscillations as through the lowered flame temperature local flame extinctions cannot be prevented. These cause fluctuations of heat release which may under certain circumstances interact with pressure variations.

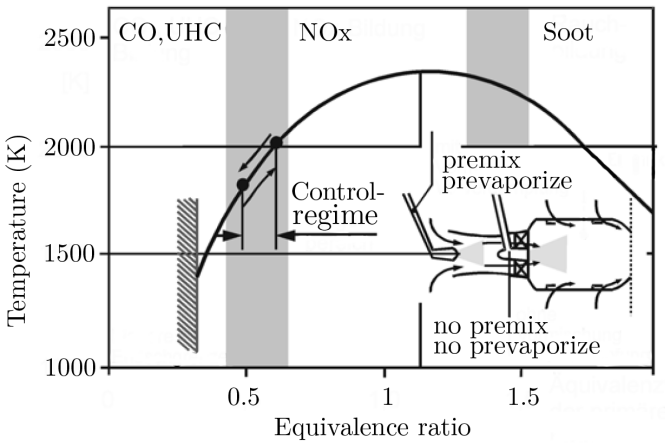

Fig. F.4: Dry low emission [10]

F.2.3 Rich quench lean

Rich quench lean (RQL) combustion takes place in several stages (*Fig. F.5*). The first stage is always in the rich regime and the transition from the rich to the lean stage has to happen fast in order to prevent peaks of high temperature.

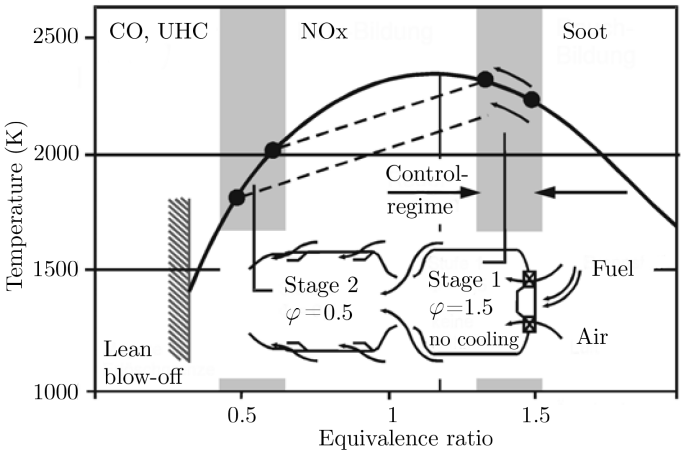

Fig. F.5: Rich quench lean [10]

F.2.4 Partial evaporation and rapid mixing

The partial evaporation and rapid mixing (PERM) concept realizes partial evaporation inside the inner duct of a swirler and fast mixing within the combustion chamber which optimizes the flame location and the combustion stability in terms of preventing flashback. PERM is closely related to the LPP technology except the fact that it can operate at higher overall pressure ratios.

F.2.5 Lean direct injection

In order to overcome the issues related to auto-ignition, flashback and resident time in hot zones (NO_x formation), fuel is injected directly through a pattern of small injectors into the combustion chamber directly. However, due to the number of injectors the control of the lean direct injection (LDI) system is more complex compared to conventional injection systems.

Bibliography

[1] Airbus S.A.S. Global market forecast 2011-2030, 2011. URL http://www.airbus.com. 16 December 2011.

[2] IATA. Climate change. URL, http://www.iata.org/whatwedo/environment/Pages/climate_change.aspx, 2011. 16 December 2011.

[3] H. Graßl. *Klimawandel*. Herder, Freiburg, 2007.

[4] IATA. Aviation and Climate Change - Pathway to carbon-neutral growth in 2020, 2011. URL http://www.iata.org. 17 December 2011.

[5] IATA. Annual report 2011, 2011. URL http://www.iata.org. 16 December 2011.

[6] A. Lundbladh and R. Avellán. Potential of Variable Cycle Engines for Subsonic Air Transport. In *International Symposium on Air Breathing Engines*, September 2007. ISABE-2007-1156.

[7] L. Xu and T. Grönstedt. A contra-rotating variable cycle turbofan engine. In *International Symposium on Air Breathing Engines*, September 2009. ISABE-2009-1161.

[8] Rolls-Royce plc. *The Jet Engine*. Rolls-Royce plc, Derby, 5th edition, 1986.

[9] Rolls-Royce plc. Trent 900, 2009. URL http://www.rolls-royce.com. 20 February 2012.

[10] F. Joos. *Technische Verbrennung, Verbrennungstechnik, Verbrennunsmodellierung, Emissionen*. Springer-Verlag, Berlin, Heidelberg, 1st edition, 2006.

[11] A. H. Lefebvre. *Gas Turbine Combustion*. Taylor & Francis, New York, 2nd edition, 1999.

[12] Rolls-Royce plc. *The Jet Engine*. Rolls-Royce plc, Derby, 6th edition, 2005.

[13] K. Aoyama and S. Mandai. Development of a dry low NOx combustor for a 120 MW gas turbine. *J. Eng. Gas Turb. Power*, 106:795–800, October 1984.

[14] Y. G. Li and R. L. Hales. Steady and dynamic performance and emissions of a variable geometry combustor in a gas turbine engine. *J. Eng. Gas Turb. Power*, 125: 961–971, October 2003.

[15] K. Smith, R. Steele, and J. Rogers. Variable geometry fuel injector for low emissions gas turbines. In *Interantional Gas Turbine and Aeroengine Congress & Exhibition*, June 1999. 99-GT-269.

[16] X. M. H. Bardey, M. A. A. Desaulty, and S. M. Meunier. Variable volume combustion chamber for a gas turbine engine. Patent, May 1993. US 5,211,675.

[17] N. Zarzalis and F. Joos. Burner for gas turbine engines with axially adjustable swirler. Patent, December 1994. US 5,373,693.

[18] W. Lutzhöft, G. Baumgärtel, and F. Fetting. Der Einfluss des Dralles auf die Stabilität von Flammen an Flammhaltern. *Brennstoff-Wärme-Kraft*, 19:402–407, 1967.

[19] N. Fricker and W. Leuckel. The characteristics of swirl-stabilized natural gas flames, Part 3: The effect of swirl and burner mouth geometry on flame stability. *Journal of the Institute of Fuel*, 49:152–158, 1976.

[20] A. K. Gupta, D. G. Lilley, and N. Syred. *Swirl Flows*. Abacus Press, Kent, 1st edition, 1984.

[21] J. M. Beér and N. A. Chigier. *Combustion Aerodynamics*. Applied Science Publishers Ltd., Barking, 1st edition, 1972.

[22] B. Mundus. *Über den Einfluss der Drallerzeugerkonstruktion auf das Strömungs- und Reaktionsfeld turbulenter Diffusionsflammen*. PhD thesis, Ruhr-Universität Bochum, 1990.

[23] R. W. Gore and W. E. Ranz. Backflows in rotating fluids moving axially through expanding cross sections. *A.I.Ch.E. Journal*, 10(1):83–88, 1964.

[24] W. G. Rose. A swirling round turbulent jet: 1–mean-flow measurements. *Journal of Applied Mechanics*, 29(4):615–625, 1962. Transactions of the ASME 841.

[25] M. Russ, A. Meyer, and H. Büchner. Scaling thermo-acoustic characteristics of LP and LPP swirl flames. In *ASME Turbo Expo*, Montreal, Canada, May 2007. GT2007-27775.

[26] E. Freitag, H. Konle, M. Lauer, C. Hirsch, and T. Sattelmayer. Pressure influence on the flame transfer function of a premixed swirling flame. In *ASME Turbo Expo*, Barcelona, Spain, May 2006. GT2006-90540.

[27] N. A. Chigier and A. Chervinsky. Experimental investigation of swirling vortex motion in jets. *Journal of Applied Mechanics*, 34(2):443–451, 1967. doi: 10.1115/1.3607703. URL http://link.aip.org/link/?AMJ/34/443/1.

[28] N. A. Chigier and J. M. Beér. Velocity and Static-Pressure Distributions in Swirling Air Jets Issuing From Annular and Divergent Nozzles. In *Transactions of the ASME*, pages 788–796, December 1964.

[29] R. Weber and J. Dugué. Combustion accelerated swirling flows in high confinements. *Prog. Energy Combust. Sci.*, 18:349–367, 1992.

[30] G. L. Borman and K. W. Ragland. *Combustion Engineering*. McGraw-Hill, New York, 1st edition, 1998.

[31] R. Palm. *Experimentelle Untersuchung der Strömung und Vermischung in einem Drallbrennermodell*. PhD thesis, Technische Universität Darmstadt, 2006.

[32] W. J. Dodds and J. S. Fear. A variable geometry combustor for broadened properties fuels. In *AIAA/SAE/ASME/ASEE 23rd Joint Propulsion Conference*, San Diego, California, 1987. AIAA-87-1832.

[33] A. K. Gupta, M. S. Ramavajjala, J. Chomiak, and N. Marchionna. Burner geometry effects on combustion and NOx emission characteristics using a variable geometry swirl combustor. *J. Propulsion*, 7(4):473–480, 1991.

[34] T. Komarek and W. Polifke. Impact of swirl fluctuations on the flame response of a perfectly premixed swirl burner. In *ASME Turbo Expo*, Orlando, Florida, June 2009. GT2009-60100.

[35] W. Leuckel. Swirl intensities, swirl types and energy losses of different swirl generating devices, 1969. IFRF Doc. No. G 02/a/16.

[36] J. Fritz, M. Kröner, and T. Sattelmayer. Flashback in a swirl burner with cylindrical premixing zone. In *ASME Turbo Expo*, New Orleans, Louisiana, USA, June 2001. 2001-GT-0054.

[37] M. Kröner, J. Fritz, and T. Sattelmayer. Flashback limits for combustion induced vortex breakdown in a swirl burner. *J. Eng. Gas Turb. Power*, 125:693–700, 2003.

[38] M. J. Lucas, R. Noreen, L. C. Sutherland, J. E. Cole, and M. C. Junger. *Handbook of the Acoustic Characteristics of Turbomachinery Cavities*. ASME Press, New York, 1st edition, 1997.

[39] M. P. Escudier. Confined vortices in flow machinery. *Annu. Rev. Fluid Mech.*, 19: 27–52, 1987.

[40] S. Leibovich. Vortex stability and breakdown: Survey and extension. *AIAA Journal*, 25(9):1192–1206, 1984.

[41] M. P. Escudier. Vortex breakdown: Observations and explanations. *Progr. Aerosp. Sciences*, 25:189–229, 1988.

[42] A. P. Dowling and A. S. Morgans. Feedback Control of Combustion Oscillations. *Annual Reviews of Fluid Mechanics*, 37:151–182, 2005.

[43] K. R. McManus, T. Poinsot, and S. M. Candel. A Review of Active Control of Combustion Instabilities. *Prog. Energy Combust. Sci.*, 19:1–29, 1993.

[44] F. Giuliani, A. Schricker, A. Lang, T. Leitgeb, and F. Heitmeir. High-temperature resistant pressure transducer for monitoring ofgas turbine combustion stability. In *International Symposium on Air Breathing Engines*, September 2007. ISABE-2007-1111.

[45] G. Y. G. Barbier, G. J. P. Bayle-Laboure, P. A. P. Bouillot, M. A. A. Desaulty, and R. Martinez. Variable flow air-fuel mixing device for a turbojet engine. Patent, February 1988. US 4,726,182.

[46] P. S. A. Ciccia and E. J. S. Lancelot. Combustion chamber with variable oxidizer intakes. Patent, March 1995. US 5,398,495.

[47] N. A. Sanders. Fuel injector. Patent, September 2007. US 7,263,833 B2.

[48] S. Hayashi, H. Yamada, and K. Shimodaira. Engine testing of a natural gas-fired low-NOx variable geometry gas turbine combustor for a small gas turbine. In *Interantional Gas Turbine and Aeroengine Congress & Exhibition*, June 1996. 96-GT-465.

[49] R. H. Johnson and C. Wilkes. Combustion control system. Patent, March 1981. US 4,255,927.

[50] R. A. Corr, II. Gas turbine combustor having poppet valves for air distribution control. Patent, May 1994. US 5,309,710.

[51] W. J. Egan, jr., R. S. Reilly, and K. N. Hopkins. Optimization of Gas Turbine Combustor Stoichiometry for Expanded Operating Regime. *J. Energy*, 5(5):289–297, September 1981. AIAA 80-1286R.

[52] P. Sampath and N. C. Davenport. Variable premix-lean burn combustor. Patent, July 2001. US 6,253,538.

[53] J. R. Arvin, R. E. Sullivan, and D. L. Troth. Combustion apparatus with combustion and dilution air modulating means. Patent, December 1975. US 3,927,520.

[54] P. W. Pillsbury and J. K. Suter. Combustion air control shutter. Patent, January 1970. US 3,490,230.

[55] J. M. Vaught. Variable geometry swirler. Patent, August 1977. US 4,044,553.

[56] E. Mach and P. Salcher. Photographische Fixierung der durch Projectile in der Luft eingeleiteten Vorgänge. *Sitzungsb. Akad. Wiss. Wien*, 95:764–780, 1887.

[57] M. Born and E. Wolf. *Principles of optics - Electromagnetic theory of propagation, interference and diffraction of light.* Cambridge University Press, Cambridge, 7th edition, 1999.

[58] H. Oertel, sen. and H. Oertel, jun. *Optische Strömungsmesstechnik.* Braun Verlag, Karlsruhe, 1989.

[59] H. Lang. *Einsatz neuer laser-optischer Messmethoden zur Untersuchung instationärer Strömungsvorgänge in transsonischen Turbinenstufen.* PhD thesis, Graz University of Technology, 2003.

[60] M. Raffel, C. Willert, and J. Kompenhans. *Particle Image Velocimetry, a practical guide.* Springer Verlag, New York, 1998.

[61] N. Lawson and J. Wu. Three-dimensional particle image velocimetry: Error analysis of stereoscopic technique. *Meas. Sci. Technol.*, 8:894–900, 1997.

[62] L. Sachs. *Angewandte Statistik.* Springer Verlag, Berlin, 10th edition, 2002.

[63] E. Giacomazzi, G. Troiani, and E. Giulietti. Effect of turbulence on flame radiative emission. *Exp. Fluids*, 44:557–564, 208.

[64] I. R. Hurle, R. B. Price, T. M. Sudgen, and T. M. Thomas. Sound Emission from Open Turbulent Flames. *Proceedings of the Royal Society A*, 303:409–427, 1968.

[65] R. B. Price, I. R. Hurle, and T. M. Sudgen. Optical Studies of the Generation of Noise in Turbulent Flames. *Symposium (International) on Combustion*, 12:1093–1102, 1969.

[66] Y. Hardalupas and M. Orain. Local Measurements of the Time-dependent Heat Release Rate and Equivalence Ratio Using Chemiluminescent Emission from a Flame. *Combust. Flame*, 139:188–207, 2004.

[67] J. G. Lee and D. A. Santavicca. Experimental Diagnostics for the Study of Combustion Instabilities in Lean Premixed Combustors. *Journal of Propulsion and Power*, 19:735–750, 2003.

[68] B. Schuermans, F. Guethe, and W. Mohr. Optical Transfer Function Measurements for Technically Premixed Flames. *J. Eng. Gas Turb. Power*, 132:0815011–0815018, 2010.

[69] M. Lauer and T. Sattelmayer. On the Adequacy of Chemiluminescence as a Measure for Heat Release in Turbulent Flames with Mixture Gradients. *J. Eng. Gas Turb. Power*, 132:061502 (8pp), 2010.

[70] B. O. Ayoola, R. Balachandran, J. H. Frank, E. Mastorakos, and C. F. Kaminski. Spatially resolved heat release rate measurements in turbulent premixed flames. *Combust. Flame*, 144:1–16, 2006.

[71] H. N. Najm, P. H. Paul, C. J. Mueller, and P. S. Wyckoff. On the Adequacy of Certain Experimental Observables as Measurements of Flame Burning Rate. *Combust. Flame*, 113:312–332, 1998.

[72] J. R. Kim, F. Akamatsu, G. M. Choi, and D. J. Kim. Observation of Local Heat Release Rate with Changing Combustor Pressure in the CH4/Air Flame (wrinkled laminar regime). *Thermochimica Acta*, 491:109–115, 2009.

[73] Y. Ikeda, J. Kojima, and H. Hashimoto. Local Chemiluminescence Spectra Measurements in a High-pressure Laminar Methane/Air Premixed Flame. *Proceedings of the Combustion Institute*, 29:1495–1501, 2002.

[74] N. Docquier, S. Belhalfaoui, F. Lacas, N. Darabiha, and C. Rolon. Experimental and Numerical Study of Chemiluminescence in Methane/Air High-pressure Flames for Active Control Applications. *Proceedings of the Combustion Institute*, 28:1765–1774, 2000.

[75] B. Higgins, M. Q. McQuay, F. Lacas, and S. Candel. An Experimental Study on the Effect of Pressure and Strain Rate on CH Chemiluminescence of Premixed Fuel-lean Methane/Air Flames. *Fuel*, 80:1583–1591, 2001.

[76] T. Schuller, D. Durox, and S. Candel. Dynamics of and Noise Radiated by a Perturbed Impinging Premixed Jet Flame. *Combust. Flame*, 128:88–110, 2002.

[77] P. Palies, D. Durox, T. Schuller, and S. Candel. The Combined Dynamics of Swirler and Turbulent Premixed Swirling Flames. *Combust. Flame*, 157:1698–1717, 2010.

[78] T. K. Pham, D. Dunn-Rankin, and W. A. Sirignano. Flame Structure in Small-scale Liquid Film Combustors. *Proceedings of the Combustion Institute*, 31:3269–3275, 2007.

[79] A. J. Marchese, F. L. Dryer, V. Nayagam, and R. O. Colantonio. Hydroxyl Radical Chemiluminescence Imaging and the Structure fo Microgravity Droplet Flames. *Twenty-Sixth Symposium (International) on Combustion, The Combustion Institute*, pages 1219–1226, 1996.

[80] A. Yoshida, M. Narisawa, and H. Tsuji. Structure of Highly Turbulent Premixed Flames. *Symposium (International) on Combustion*, 24:519–525, 1992.

[81] J. Floyd and A. M. Kempf. Computed Tomography of Chemiluminescence (CTC): High resolution and instantaneous 3-D measurements of a Matrix burner. *Proceedings of the Combustion Institute*, 33:751–758, 2011.

[82] N. Anikin, R. Suntz, and H. Bockhorn. Tomographic Reconstruction of the OH-chemiluminescence Distribution in Premixed and Diffusion Flames. *Applied Physics B*, 100:675–694, 2010.

[83] M. Hipp, P. Reiterer, J. Woisetschläger, H. Philipp, G. Pretzler, W. Fliesser, and T. Neger. Application of Interferometric Fringe Evaluation Software at Technical University Graz. *Proceedings of SPIE*, 3745:281–292, 1999. doi: 10.1117/12.357789.

[84] M. Hipp, J. Woisetschläger, P. Reiterer, and T. Neger. Digital evaluation of interferograms. *Measurement*, 36(1):53–66, July 2004. doi: 10.1016/j.measurement.2004.04.003.

[85] M. Hipp and P. Reiterer. *User Manual for IDEA 1.7 - Software for Interferometrical Data Evaluation*. Graz, 2003. Graz University of Technology, Institute for Physics.

[86] G. T. Herman. *Image reconstruction from projections*. Academic Press, 1980.

[87] A. Lewin, F. Mohr, and H. Selbach. Heterodyn-Interferometer zur Vibrationsanalyse. *Technisches Messen*, 57:335–345, 1990.

[88] A. Lewin. New Compact Laser Vibrometer for Industrial and Medical Applications. *Third International Conference on Vibration Mesurements by Laser Techniques*, 3411:61–67, 1999.

[89] N. Mayrhofer and J. Woisetschläger. Frequency analysis of turbulent compressible flows by laser vibrometry. *Exp. Fluids*, 31:153–161, 2001.

[90] F. Giuliani, T. Leitgeb, A. Lang, and J. Woisetschläger. Mapping the Density Fluctuations in a Pulsed Air-Methane Flame Using Laser-Vibrometry. *J. Eng. Gas Turb. Power*, 132:0316031–0316038, 2010.

[91] W. Merzkirch. *Flow Visualization*. Academic Press, Orlando, 2nd edition, 1987.

[92] W. C. Gardiner, jr., Y. Hidaka, and T. Tanzawa. Refractivity of Combustion Gases. *Combust. Flame*, 40:213–219, 1981.

[93] H. Barrell and J. E. Sears. The refraction and dispersion of air for the visible spectrum. *Philosophical Transactions of the Royal Society of London. Series A, Mathematical and Physical Sciences*, 238(786):1–64, February 1939. URL http://www.jstor.org/stable/91351.

[94] J. Woisetschläger, G. Pretzler, H. Jericha, and H.-P. Pirker. Differential interferometry with adjustable spatial carrier fringes for turbine blade cascade flow investigations. *Exp. Fluids*, 24(2):102–109, 1998. doi: 10.1007/s003480050157.

[95] G. Pretzler, H. Jäger, and T. Neger. High-accuracy differential interferometry for the investigation of phase objects. *Meas. Sci. Technol.*, 4:649–658, 1993.

[96] R. Proebster. Implementing of a variable geometry burner testrig. Master's thesis, Graz University of Technology, 2011.

[97] D. A. Long. *Raman Spectroscopy*. McGraw-Hill, New York, 1st edition, 1977.

[98] C. V. Raman and K. S. Krishnan. A new type of secondary radiation. *Nature*, 121: 501, March 1928.

[99] A. Donges and R. Noll. *Lasermesstechnik*. Huethig Buch Verlag, 1st edition, 1993.

[100] R. B. Miles, W. R. Lempert, and J. N. Forkey. Laser rayleigh scattering. *Meas. Sci. Technol.*, 12(5):33–51, 2001.

[101] K. Hayashida, K. Amagai, K. Sato, and M. Arai. Measurement of fuel concentration distribution in sooting flame through Raman scattering. *JSME International Journal Series B*, 49:512–517, 2006.

[102] M. Rachner. Die Stoffeigenschaften von Kerosin Jet-A1. Mitteilung 98-01, März 1998. Deutsches Zentrum für Luft- und Raumfahrt e.V., Köln.

[103] G. Li and E. J. Gutmark. Effects of swirler configurations on flow structures and combustion characteristics. In *ASME Turbo Expo*, Vienna, Austria, June 2004. GT2004-53674.

[104] A. Lang. Konstruktion eines Brennkammer-Prüfstandes und Messungen unter mittlerem Druck. Diplomarbeit, Technische Universität Graz, Institut für Thermische Turbomaschinen und Maschinendynamik, Graz, Österreich, März 2007.

[105] A. Lang, T. Leitgeb, J. Woisetschläger, A. Strzelecki, P. Gajan, and F. Giuliani. Analysis of a Pusled Flame at Intermediate Pressure, July 2008. French Congress on Visualization in Fluid Mechanics.

[106] S. Köberl, F. Fontaneto, F. Giuliani, and J. Woisetschläger. Frequency-resolved interferometric measurement of local density fluctuations for turbulent combustion analysis. *Meas. Sci. Technol.*, 21:035302 (10pp), 2010.

[107] C. A. Jacobson, A. I. Khibnik, A. Banaszuk, J. Cohen, and W. Proscia. Active Control of Combustion Instabilities in Gas Turbine Engines for Low Emissions. Part I: Physics-Based and Experimentally Identified Models of Combustion Instability, May 2000. RTO AVT Symposium on 'Active Control Technology for Enhanced Performance Operational Capabilities of Military Aircraft, Land Vehicles and Sea Vehicles'.

[108] G. Billoud, M. A. Galland, C. Huynh Huu, and S. Candel. Adaptive Active Control of Combustion Instabilities. *Combust. Sci. and Tech.*, 81:257–283, 1992.

[109] S. Evesque. *Adaptive Control of Combustion Oscillations*. PhD thesis, University of Cambridge, 2000.

[110] K. H. Yu. Fundamentals and Fluid Dynamics – Experiments, May 2001. RTO AVT/VKI Lecture Series on 'Active Control of Engine Dynamics'.

[111] K. McManus, F. Han, W. Dunstan, C. Barbu, and M. Shah. Modeling and control of combustion dynamics in industrial gas turbines. In *Proceedings of ASME Turbo Expo 2004*, Vienna, June 2004. GT2004-53872.

[112] B. Krautkremer. *Untersuchung der Sekundärlufteinblasung in eine drallbehaftete Gasturbinen-Brennkammerströmung*. PhD thesis, Technical University of Darmstadt, Darmstadt, January 2003.

[113] P. Albrecht, F. Bauermeister, M. Bothien, A. Lacarelle, J. Moeck, C. O. Paschereit, and E. J. Gutmark. Characterization and control of lean blowout using periodically generated flame balls. In *Proceedings of ASME Turbo Expo 2006*, May 2006. GT2006-90340.

[114] S. Kokanović, G. Guidati, S. Torchalla, and B. Schuermans. Active combustion control system for reduction of nox and pulsation levels in gas turbines. In *Proceedings ASME Turbo Expo 2006*, Barcelona, may 2006. GT2006-90895.

[115] J. Y. Lee, E. Lubarsky, and B. T. Zinn. Suppression of instabilities in liquid fueled combustior by variation of fuel spray properties. In *Proceedings of ASME Turbo Expo 2003*, Atlanta, June 2003. GT2003-38169.

[116] M. Lohrmann and H. Büchner. Scaling of stabiltiy limits in lean-premixed gas turbine combustors. In *Proceedings of ASME Turbo Expo 2004*, June 2004. GT2004-53710.

[117] K. P. Vanoverberghe, E. V. Van den Bulck, M. J. Tummers, and W. A. Hübner. Multiflame Patterns in Swirl-Driven Partially Premixed Natural Gas Combustion. *J. Eng. Gas Turb. Power*, 125:40–45, January 2003.

[118] M. Sanjosé, T. Lederlin, L. Gicquel, B. Cuenot, H. Pitsch, N. García-Rosa, R. Lecourt, and T. Poinsot. LES of two-phase reacting flows. In *Proceedings of the Summer Program 2008*, pages 251–263. Center for Turbulence Research, 2008.

[119] J. E. Ffowcs Williams. Sound Sources in Aerodynamics – Fact and Fiction. *AIAA Journal*, 20:307–315, 1982.

[120] S. Candel, D. Durox, S. Ducruix, A. L. Birbaud, N. Noiray, and T. Schuller. Flame dynamics and combustion noise: progress and challenges. *International Journal of Aeroacoustics*, 8:1–56, 2009.

[121] T. Leitgeb, T. Schuller, D. Durox, F. Giuliani, S. Köberl, and J. Woisetschläger. Interferometric Determination of Heat Release Rate in a Pulsated Flame. *Combust. Flame*, 2012. doi: 10.1016/j.combustflame.2012.11.001.

[122] B. Hampel and J. Woisetschläger. Frequency- and space-resolved measurement of local density fluctuations in air by laser vibrometry. *Meas. Sci. Technol.*, 17:2835–2842, 2006.

[123] H. Jericha, E. Göttlich, W. Sanz, and F. Heitmeir. Design Optimization of the Graz Cycle Prototype Plant. *J. Eng. Gas Turb. Power*, 126:733–740, 2004.

[124] G. Huster. Schadstoffemission - Vorschriften und Schadstoffermittlung, July 1992. MTU.

[125] J. Warnatz, U. Maas, and R. W. Dibble. *Verbrennung.* Springer Verlag, Berlin, 3rd edition, 2001.

[126] G. Merker, C. Schwarz, G. Stiesch, and F. Otto. *Verbrennungsmotoren - Simulation der Verbrennung und Schadstoffbildung.* Teubner Verlag, Wiesbaden, 3rd edition, 2006.

[127] T. Behrendt. *Strömung und Verbrennung in einem neuen Düsenkonzept für magere Vormischverbrennung in Fluggasturbinen.* PhD thesis, Ruhr Universität Bochum, Fakultät für Maschinenbau, Bochum, 2004.

[128] F. Giuliani. Gas Turbine Combustion, October 2007. Skriptum zur Vorlesung aus Verbrennung in Gasturbinen an der Technischen Universität Graz.

[129] S. W. Zettl. Stickoxidreduzierung von Gasturbinenbrennkammern durch gestufte Luftzufuhr (Fett-Mager-Verbrennung). Diplomarbeit, Universität Karlsruhe, Engler-Bunte-Institut, March 1991.

[130] H. C. Mongia. TAPS - A Fourth Generation Propulsion Combustor Technology for Low Emissions. In *AIAA/ICAS International Air and Space Symposium and Exposition: The Next 100 Years*, volume 2, Dayton, Ohio, July 2003. AIAA 2003-2657.